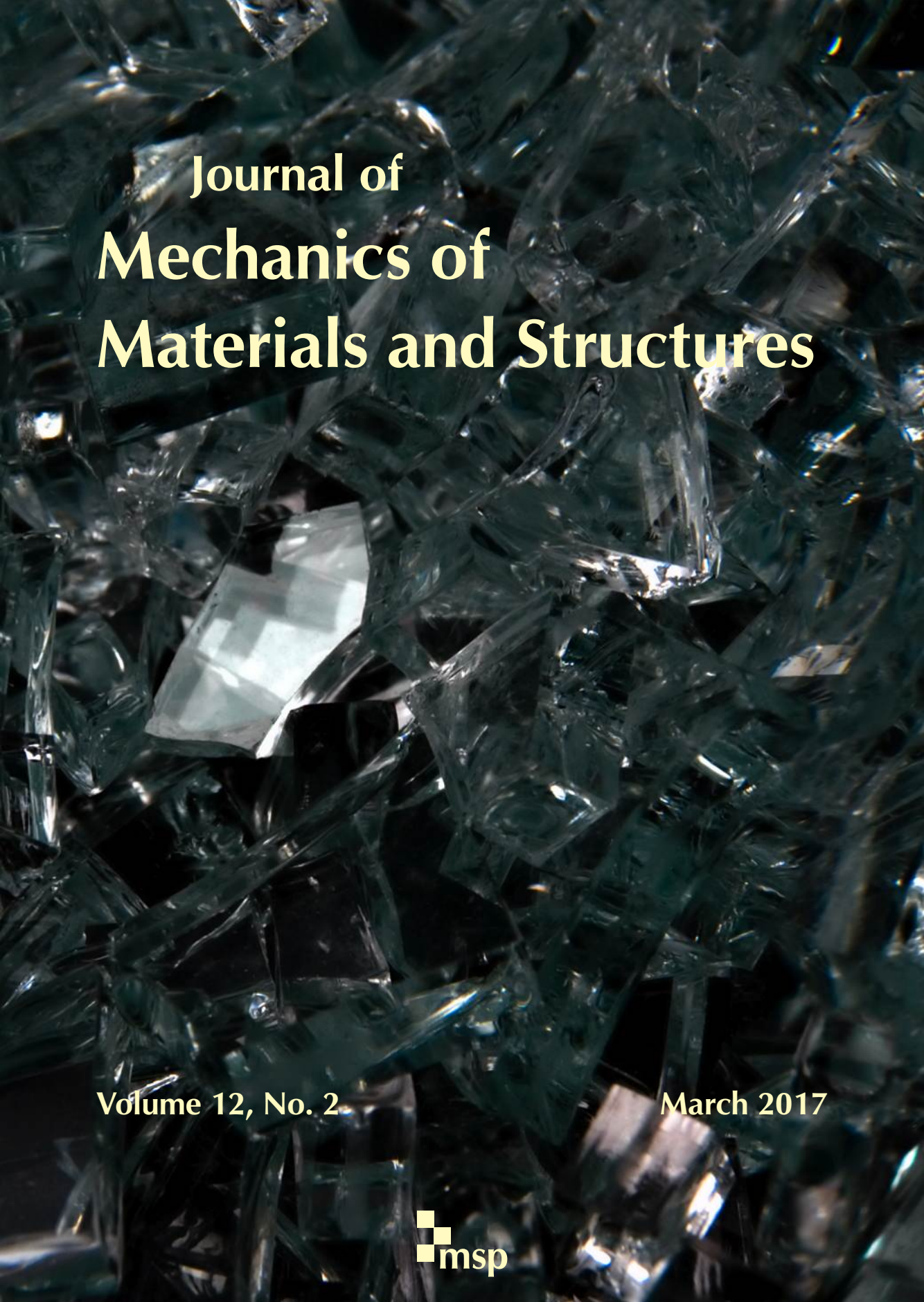

Journal of Mechanics of Materials and Structures

Volume 12, No. 2 March 2017

msp

JOURNAL OF MECHANICS OF MATERIALS AND STRUCTURES

msp.org/jomms

Founded by Charles R. Steele and Marie-Louise Steele

Cover photo: Mando Gomez, www.mandolux.com

See msp.org/jomms for submission guidelines.

JoMMS (ISSN 1559-3959) at Mathematical Sciences Publishers, 798 Evans Hall #6840, c/o University of California, Berkeley, CA 94720-3840, is published in 10 issues a year. The subscription price for 2017 is US $615/year for the electronic version, and $775/year (+$60, if shipping outside the US) for print and electronic. Subscriptions, requests for back issues, and changes of address should be sent to MSP.

JoMMS peer-review and production is managed by EditFLOW® from Mathematical Sciences Publishers.

PUBLISHED BY

mathematical sciences publishers

nonprofit scientific publishing

http://msp.org/

JOURNAL OF MECHANICS OF MATERIALS AND STRUCTURES
Vol. 12, No. 2, 2017
dx.doi.org/10.2140/jomms.2017.12.147

A NOTE ON CROSS PRODUCT BETWEEN TWO SYMMETRIC SECOND-ORDER TENSORS

LÁSZLÓ SZABÓ

The present work is concerned with defining the cross product for symmetric, second-order tensors. The operation presented in this paper generalizes the classical vectorial cross product from three-dimensional Euclidean space to symmetric tensor fields on a seven-dimensional vector space. The result of the cross product operation expresses a nonsymmetric tensor as a sum of a symmetric and a skew-symmetric tensor with one parameter, which satisfies the usual properties of the vector cross product except the triple cross product rule. The cross product formulation can be applied to pairs of symmetric or nonsymmetric tensors where the skew-symmetric parts have the same eigenvectors.

1. Introduction

The vectorial cross product in three-dimensional Euclidean space is broadly used in physics, engineering and other fields. It is a bilinear operation on two vectors $\boldsymbol{a}$, $\boldsymbol{b}$, in three-dimensional vector space, that outputs a vector, $\boldsymbol{a} \times \boldsymbol{b}$, that is perpendicular to both $\boldsymbol{a}$ and $\boldsymbol{b}$. The operation is characterized by three basic properties:

(1) skew-symmetry ($\boldsymbol{a} \times \boldsymbol{b} = -\boldsymbol{a} \times \boldsymbol{b}$),

(2) orthogonality ($\boldsymbol{a} \times \boldsymbol{b} \perp \boldsymbol{a}$ and $\boldsymbol{b}$),

(3) length rule ($|\boldsymbol{a} \times \boldsymbol{b}| = |\boldsymbol{a}||\boldsymbol{b}| \sin\alpha$, where α denotes the angle enclosed by $\boldsymbol{a}$ and $\boldsymbol{b}$).

Applying the geometric formula for the Euclidean inner product, $\boldsymbol{a} \cdot \boldsymbol{b} = |\boldsymbol{a}||\boldsymbol{b}| \cos\alpha$, the third property can be written in the form of Lagrange's identity: $|\boldsymbol{a}|^2|\boldsymbol{b}|^2 = (\boldsymbol{a} \cdot \boldsymbol{b})^2 + |\boldsymbol{a} \times \boldsymbol{b}|^2$.

An operation similar to the dot product can be defined for two second-order tensors $\boldsymbol{A}$, $\boldsymbol{B}$ defined on the same vector space via the double dot product: $\boldsymbol{A} : \boldsymbol{B} = \|\boldsymbol{A}\|\|\boldsymbol{B}\| \cos\beta$. The analogue of the cross product between $\boldsymbol{A}$ and $\boldsymbol{B}$, however, has not been proposed in literature. Analogous to the vectorial cross product in $\mathbb{R}^3$, a cross product of second-order tensors would plausibly have to satisfy the three properties listed above: skew-symmetry, orthogonality and Lagrange's identity. Defining such a cross product, however, is hindered by the same challenges as extending the cross product to higher-dimensional vector spaces. As a consequence of those challenges, vectorial cross products can only be defined in the three- and seven-dimensional Euclidean spaces (see, e.g., [Eckmann 1943; Brown and Gray 1967; Massey 1983; Shaw 1987]). An exception, however, is the cross product between two general second-order tensors acting on three-dimensional Euclidean space, given that each tensor can be viewed as elements of a nine-dimensional vector space.

In this paper, we introduce a tensorial cross product for symmetric, second-order tensors. When viewed as a subspace of seven-dimensional linear space, the six-dimensional subspace of symmetric

Keywords: vector cross product, second-order tensors, tensorial cross product, seven-dimensional vector space.

tensors inherits a cross product from the ambient seven-dimensional space. The result of this product operation will be a well-defined but nonsymmetric tensor. This construct is analogous to the three-dimensional vectorial cross product restricted to vectors in a two-dimensional plane of $\mathbb{R}^3$, with the resulting cross product normal to the plane in $\mathbb{R}^3$.

In this paper, we first introduce the notation used. In Section 2, the basic properties of cross product in three- and seven-dimensional vector spaces are briefly summarized before some definitions of cross product of second-order tensors are outlined. Sections 3 and 4 present a definition of the cross product between two symmetric second-order tensors. In Section 5, a simple application of the newly developed cross product operation is presented on the field of elastoplasticity. Finally, a conclusion of the results is given in Section 6.

Regarding notation, vectors and tensors are denoted by bold-face characters, the order of which is indicated in text. The cross product is denoted by $\times$, the superscript T denotes the transpose and the trace is indicated by the prefix tr. The tensor product is denoted by $\otimes$ and the following symbolic operations apply:

$$\boldsymbol{a}\cdot\boldsymbol{b}=a_ib_i \quad \text{and} \quad (\boldsymbol{A}\cdot\boldsymbol{B})_{ij}=\mathrm{A}_{ik}\mathrm{B}_{kj} \quad \text{and} \quad \boldsymbol{A}:\boldsymbol{B}=\mathrm{A}_{ij}\mathrm{B}_{ij},$$

with summation over repeated indices. The symbols

$$|\boldsymbol{a}|=\sqrt{\boldsymbol{a}\cdot\boldsymbol{a}} \quad \text{and} \quad \|\boldsymbol{A}\|=\sqrt{\boldsymbol{A}:\boldsymbol{A}}\equiv\sqrt{\mathrm{tr}(\boldsymbol{A}\cdot\boldsymbol{A}^T)}$$

are used to denote a norm of vector $\boldsymbol{a}$ and second order tensor $\boldsymbol{A}$. The three- and seven-dimensional Euclidean spaces are represented by the symbols $\mathbb{R}^3$ and $\mathbb{R}^7$, and the orthonormal basis vectors for these spaces are denoted by $\boldsymbol{e}_i$ ($i\in[1,3]$) and $\boldsymbol{E}_\alpha$ ($\alpha\in[1,7]$), respectively. The notation $[\boldsymbol{a}]$ and $[\boldsymbol{A}]$ represent the column vector and square matrix, respectively, formed by the coordinates of the vector $\boldsymbol{a}$ and the second-order tensor $\boldsymbol{A}$.

2. Theoretical background

2.1. ***Cross product of two vectors in a 3D vector space.*** In this section, we briefly summarize the basic properties and identities of the cross product defined on the three-dimensional vector space (see, e.g., [Fenn 2001; Itskov 2015; Young 1993]). Let $\boldsymbol{a}=a_i\boldsymbol{e}_i$ and $\boldsymbol{b}=b_i\boldsymbol{e}_i$ be two vectors in $\mathbb{R}^3$. The cross product of vectors $\boldsymbol{a}$ and $\boldsymbol{b}$, or $\boldsymbol{a}\times\boldsymbol{b}$, is defined by

$$\boldsymbol{a}\times\boldsymbol{b}=a_ib_j\epsilon_{ijk}\boldsymbol{e}_k, \tag{1}$$

and its coordinates can be expressed as

$$[\boldsymbol{a}\times\boldsymbol{b}]^T=[a_2b_3-a_3b_2,\ a_3b_1-a_1b_3,\ a_1b_2-a_2b_1], \tag{2}$$

where ϵ_{ijk} represents the Levi–Civita permutation symbol, a_i and b_i are the vector coordinates with $i\in[1,2,3]$.

The resulting vector has the distinct property of orthogonality between two given vectors, which implies that

$$\boldsymbol{a}\cdot(\boldsymbol{a}\times\boldsymbol{b})=0, \quad \boldsymbol{b}\cdot(\boldsymbol{a}\times\boldsymbol{b})=0. \tag{3}$$

From (2), it is readily seen that the cross product is skew-symmetric, that is

$$\boldsymbol{a} \times \boldsymbol{b} = -\boldsymbol{b} \times \boldsymbol{a}. \tag{4}$$

The magnitude of vector $\boldsymbol{a} \times \boldsymbol{b}$ is given by

$$|\boldsymbol{a} \times \boldsymbol{b}| = |\boldsymbol{a}||\boldsymbol{b}| \sin \alpha, \tag{5}$$

where α is the angle between $\boldsymbol{a}$ and $\boldsymbol{b}$. The angle α can also be defined in the inner or dot product of vectors $\boldsymbol{a}$ and $\boldsymbol{b}$:

$$\boldsymbol{a} \cdot \boldsymbol{b} = |\boldsymbol{a}||\boldsymbol{b}| \cos \alpha. \tag{6}$$

A well-known consequence of formulas (5) and (6) is that the cross product is related to the inner product via the formula

$$|\boldsymbol{a} \times \boldsymbol{b}|^2 = |\boldsymbol{a}|^2 |\boldsymbol{b}|^2 - (\boldsymbol{a} \cdot \boldsymbol{b})^2. \tag{7}$$

Finally, we introduce two important identities. Let $\boldsymbol{c}$ be a vector in $\mathbb{R}^3$. The vector triple cross product identity can be written in the form

$$\boldsymbol{a} \times (\boldsymbol{b} \times \boldsymbol{c}) = (\boldsymbol{a} \cdot \boldsymbol{c})\boldsymbol{b} - (\boldsymbol{a} \cdot \boldsymbol{b})\boldsymbol{c}. \tag{8}$$

From (8), it follows that

$$\boldsymbol{a} \times (\boldsymbol{b} \times \boldsymbol{c}) + \boldsymbol{b} \times (\boldsymbol{c} \times \boldsymbol{a}) + \boldsymbol{c} \times (\boldsymbol{a} \times \boldsymbol{b}) = \mathbb{0}, \tag{9}$$

which is known as the Jacobi identity.

2.2. ***Some further definitions of the cross product in 3D vector space.*** A number of ways to extend the definition of the cross product, in three-dimensional Euclidean space, have been proposed in the literature (see, e.g., [Altenbach 2012; Rubin 2000; Schade and Neemann 2009; Steinmann 2015]). Let's take a brief look at some of these.

2.2.1. *Cross product between a vector and a second-order tensor.* The left cross product of vector $\boldsymbol{a}$ and second-order tensor $\boldsymbol{A}$ is defined by

$$\boldsymbol{a} \times \boldsymbol{A} = (a_i \boldsymbol{e}_i) \times (A_{jl} \boldsymbol{e}_j \otimes \boldsymbol{e}_l) = a_i A_{jl}\, \epsilon_{ijk} \boldsymbol{e}_k \otimes \boldsymbol{e}_l, \tag{10}$$

while the right cross product is given by

$$\boldsymbol{A} \times \boldsymbol{a} = (A_{jl} \boldsymbol{e}_j \otimes \boldsymbol{e}_l) \times (a_i \boldsymbol{e}_i) = a_i A_{jl} \epsilon_{kli} \boldsymbol{e}_k \otimes \boldsymbol{e}_l. \tag{11}$$

2.2.2. *Cross product of second-order tensors.* Define $\boldsymbol{A} = A_{ij} \boldsymbol{e}_i \otimes \boldsymbol{e}_j$ and $\boldsymbol{B} = B_{ij} \boldsymbol{e}_i \otimes \boldsymbol{e}_j$ in $\mathbb{R}^3$. Then we have the following three definitions of the cross product between two second-order tensors:

$$\boldsymbol{A} \underline{\times} \boldsymbol{B} = A_{ij} B_{kj} \epsilon_{pik} \boldsymbol{e}_p, \tag{12}$$

$$\boldsymbol{A} \underline{\overline{\times}} \boldsymbol{B} = A_{ij} B_{kl}\, \epsilon_{ikm} \epsilon_{jln} \boldsymbol{e}_m \otimes \boldsymbol{e}_n, \tag{13}$$

$$\boldsymbol{A} \underline{\underline{\times}} \boldsymbol{B} = A_{ij} B_{kl} \epsilon_{kpj} \boldsymbol{e}_i \otimes \boldsymbol{e}_p \otimes \boldsymbol{e}_l. \tag{14}$$

It is important to note that the operations above do not in general satisfy properties (3)–(9) of the vector product. For more details on these cross products, we refer to [Altenbach 2012; Rubin 2000; Schade and Neemann 2009; Steinmann 2015; de Boer 1982].

Note that the formulation (14) is used in the definition of the homography tensor in the field of computer vision, [Shashua and Wolf 2000] and (13) has been used most recently by Bonet et al. [2015].

2.3. ***Cross product of two vectors in a 7D vector space.*** Three- and seven-dimensional Euclidean spaces are the only Euclidean spaces to have a vector product (see, e.g., [Eckmann 1943; Brown and Gray 1967; Massey 1983; Shaw 1987; Chauhan and Negi 2011; Silagadze 2002; Bisht et al. 2008]). Namely, if $\boldsymbol{u} = u_\alpha \boldsymbol{E}_\alpha$ and $\boldsymbol{v} = v_\alpha \boldsymbol{E}_\alpha$ are two vectors in $\mathbb{R}^7$, then a vector $\boldsymbol{u} \times \boldsymbol{v}$ also in $\mathbb{R}^7$ can be written as

$$\boldsymbol{u} \times \boldsymbol{v} = (u_\alpha \boldsymbol{E}_\alpha) \times (v_\beta \boldsymbol{E}_\beta) = w_\gamma \boldsymbol{E}_\gamma = \boldsymbol{w}, \tag{15}$$

where u_α, v_α, and w_α are the vector coordinates, and $\alpha \in [1, 7]$. In what follows, the subscript index with Greek letters takes the values $1, 2, 3, \ldots, 7$.

The coordinates of the resulting vector $\boldsymbol{w}$ can be defined by

$$w_\gamma = u_\alpha v_\beta f_{\alpha\beta\gamma}; \tag{16}$$

here the symbol $f_{\alpha\beta\gamma}$ (see, for example, [Shaw 1987; Chauhan and Negi 2011; Bisht et al. 2008; Baez 2002]) takes the value 1 for the triples

$$f_{\alpha\beta\gamma} = +1 \quad \text{for } (\alpha\beta\gamma) = (123), (471), (257), (165), (624), (543), (736), \tag{17}$$

and is otherwise characterized by being completely antisymmetric in the indices (so for example $f_{123} = +1$ implies $f_{213} = f_{321} = f_{132} = -1$, and $f_{\alpha\beta\gamma} = 0$ unless all three indices are distinct).

For further consideration, the coordinates w_α are listed below:

$$\begin{aligned}
w_1 &= u_2v_3 - u_3v_2 + u_6v_5 - u_5v_6 + u_4v_7 - u_7v_4,\\
w_2 &= u_3v_1 - u_1v_3 + u_4v_6 - u_6v_4 + u_5v_7 - u_7v_5,\\
w_3 &= u_1v_2 - u_2v_1 + u_5v_4 - u_4v_5 + u_6v_7 - u_7v_6,\\
w_4 &= u_3v_5 - u_5v_3 + u_6v_2 - u_2v_6 + u_7v_1 - u_1v_7,\\
w_5 &= u_4v_3 - u_3v_4 + u_1v_6 - u_6v_1 + u_7v_2 - u_2v_7,\\
w_6 &= u_2v_4 - u_4v_2 + u_5v_1 - u_1v_5 + u_7v_3 - u_3v_7,\\
w_7 &= u_1v_4 - u_4v_1 + u_2v_5 - u_5v_2 + u_3v_6 - u_6v_3.
\end{aligned} \tag{18}$$

Note that while the three-dimensional cross product is unique up to a sign, there are many seven-dimensional cross products (see, e.g., [Shaw 1987; Chauhan and Negi 2011; Baez 2002; Dray and Manogue 2015]). These are defined using the symbol $f_{\alpha\beta\gamma}$ and are associated to the octonion multiplication table (see, e.g., [Fenn 2001; Chauhan and Negi 2011; Baez 2002; Dray and Manogue 2015; Ebbinghaus et al. 1991]). In our case, the cross product is consistent with the three-dimensional subspaces, namely if $u_4 = u_5 = u_6 = u_7 = 0$ and $v_4 = v_5 = v_6 = v_7 = 0$, the resulting vector is equivalent

to (2). For further details of octonion algebra, the reader is referred to [Baez 2002; Dray and Manogue 2015; Fenn 2001].

Like the cross product in three-dimensions, the seven-dimensional product is anticommutative and $\boldsymbol{u} \times \boldsymbol{v}$ is orthogonal both to $\boldsymbol{u}$ and to $\boldsymbol{v}$, namely

$$\boldsymbol{u} \times \boldsymbol{v} = -\boldsymbol{v} \times \boldsymbol{u}, \quad \boldsymbol{u} \cdot (\boldsymbol{u} \times \boldsymbol{v}) = 0, \quad \boldsymbol{v} \cdot (\boldsymbol{u} \times \boldsymbol{v}) = 0. \tag{19}$$

Moreover, the Pythagorean formula (6) with (5) and (7) can also be satisfied:

$$|\boldsymbol{u} \times \boldsymbol{v}|^2 = |\boldsymbol{u}|^2 |\boldsymbol{v}|^2 - (\boldsymbol{u} \cdot \boldsymbol{v})^2. \tag{20}$$

Finally, it is important to note that the vector product in $\mathbb{R}^7$ does not satisfy the triple cross product (8), nor the Jacobi identity (9). However, the seven-dimensional cross product satisfies the Malcev identity (see, e.g., [Ebbinghaus et al. 1991]):

$$(\boldsymbol{u} \times \boldsymbol{v}) \times (\boldsymbol{u} \times \boldsymbol{t}) + \boldsymbol{u} \times [(\boldsymbol{u} \times \boldsymbol{v}) \times \boldsymbol{t}] - \boldsymbol{u} \times [\boldsymbol{u} \times (\boldsymbol{v} \times \boldsymbol{t})] + \boldsymbol{v} \times [\boldsymbol{u} \times (\boldsymbol{u} \times \boldsymbol{t})] = 0, \tag{21}$$

as a generalization of Jacobi identity. Here $\boldsymbol{t} = t_\alpha \boldsymbol{E}_\alpha$ is also a vector in $\mathbb{R}^7$.

3. Cross product between two symmetric second-order tensors

3.1. ***The case of two symmetric second-order tensors.*** In this section we introduce a new definition of cross product on two symmetric second-order tensors. This operation is based on the seven-dimensional Euclidean cross product.

Let $\boldsymbol{A} = A_{ij} \boldsymbol{e}_i \otimes \boldsymbol{e}_j$ and $\boldsymbol{B} = B_{ij} \boldsymbol{e}_i \otimes \boldsymbol{e}_j$ be two symmetric second-order tensors in $\mathbb{R}^3$ ($\boldsymbol{A}^T = \boldsymbol{A}$ and $\boldsymbol{B}^T = \boldsymbol{B}$), with the matrices of these tensors defined by

$$[\boldsymbol{A}] = \begin{bmatrix} A_{11} & A_{12} & A_{13} \\ A_{21} & A_{22} & A_{23} \\ A_{31} & A_{32} & A_{33} \end{bmatrix}, \quad [\boldsymbol{B}] = \begin{bmatrix} B_{11} & B_{12} & B_{13} \\ B_{21} & B_{22} & B_{23} \\ B_{31} & B_{32} & B_{33} \end{bmatrix}.$$

Moreover, consider two vectors, $\boldsymbol{u} = u_\alpha \boldsymbol{E}_\alpha$ and $\boldsymbol{v} = v_\alpha \boldsymbol{E}_\alpha$ in $\mathbb{R}^7$, with coordinates defined using Mandel's matrix notation:

$$[\boldsymbol{u}]^T = \begin{bmatrix} A_{11} & A_{22} & A_{33} & \sqrt{2}A_{23} & \sqrt{2}A_{13} & \sqrt{2}A_{12} & 0 \end{bmatrix}, \tag{22}$$

$$[\boldsymbol{v}]^T = \begin{bmatrix} B_{11} & B_{22} & B_{33} & \sqrt{2}B_{23} & \sqrt{2}B_{13} & \sqrt{2}B_{12} & 0 \end{bmatrix}. \tag{23}$$

In this case, the dot products are identical, so that

$$\boldsymbol{A} : \boldsymbol{B} = \boldsymbol{u} \cdot \boldsymbol{v}. \tag{24}$$

Now, the cross product of vectors $\boldsymbol{u}$ and $\boldsymbol{v}$ is defined by an expression similar to (15), but $u_7 = v_7 = 0$:

$$\boldsymbol{u} \times \boldsymbol{v} = (u_\alpha \boldsymbol{E}_\alpha) \times (v_\beta \boldsymbol{E}_\beta) = u_\alpha v_\beta f_{\alpha\beta\gamma} \boldsymbol{E}_\gamma = w_\gamma \boldsymbol{E}_\gamma = \boldsymbol{w}, \tag{25}$$

where the symbol $f_{\alpha\beta\gamma}$ is defined in (17), and the components w_α, where $\alpha \in [1, 7]$, using (18) are expressed as

$$\begin{aligned}
w_1 &= A_{22}B_{33} - A_{33}B_{22} + 2(A_{12}B_{13} - A_{13}B_{12}),\\
w_2 &= A_{33}B_{11} - A_{11}B_{33} + 2(A_{23}B_{12} - A_{12}B_{23}),\\
w_3 &= A_{11}B_{22} - A_{22}B_{11} + 2(A_{13}B_{23} - A_{23}B_{13}),\\
w_4 &= \sqrt{2}(A_{12}B_{22} - A_{22}B_{12} + A_{33}B_{13} - A_{13}B_{33}),\\
w_5 &= \sqrt{2}(A_{11}B_{12} - A_{12}B_{11} + A_{23}B_{33} - A_{33}B_{23}),\\
w_6 &= \sqrt{2}(A_{22}B_{23} - A_{23}B_{22} + A_{13}B_{11} - A_{11}B_{13}),\\
w_7 &= \sqrt{2}(A_{11}B_{23} - A_{23}B_{11} + A_{22}B_{13} - A_{13}B_{22} + A_{33}B_{12} - A_{12}B_{33}).
\end{aligned} \tag{26}$$

Finally, we define the cross product as

$$\boldsymbol{A} \times \boldsymbol{B} = \boldsymbol{C}, \tag{27}$$

where the tensor $\boldsymbol{C}$ can be decomposed into symmetric and a skew-symmetric parts:

$$\boldsymbol{C} = \boldsymbol{C}_S + \boldsymbol{C}_A. \tag{28}$$

The components of these tensors are defined by the components of the resulting vector $\boldsymbol{w}$ (25) as follows:

$$[\boldsymbol{C}_S] = \begin{bmatrix} w_1 & \frac{1}{\sqrt{2}}w_6 & \frac{1}{\sqrt{2}}w_5 \\ \frac{1}{\sqrt{2}}w_6 & w_2 & \frac{1}{\sqrt{2}}w_4 \\ \frac{1}{\sqrt{2}}w_5 & \frac{1}{\sqrt{2}}w_4 & w_3 \end{bmatrix}, \quad [\boldsymbol{C}_A] = \frac{1}{\sqrt{2}}w_7 \begin{bmatrix} 0 & 1 & 0 \\ -1 & 0 & 0 \\ 0 & 0 & 0 \end{bmatrix}. \tag{29}$$

Now, we impose the seven-dimensional vector space structure on 3x3 (real) matrices by looking at symmetric matrices $[\boldsymbol{C}_S]$ with 6 coordinates (w_α, where $\alpha \in [1, 6]$) together with one antisymmetric piece (w_7).

As in the preceding Section 2.3, we have the following properties:

(i) skew-symmetry,

$$\boldsymbol{A} \times \boldsymbol{B} = -(\boldsymbol{B} \times \boldsymbol{A}); \tag{30}$$

(ii) orthogonality

$$(\boldsymbol{A} \times \boldsymbol{B}) : \boldsymbol{A} = 0, \quad (\boldsymbol{A} \times \boldsymbol{B}) : \boldsymbol{B} = 0, \tag{31}$$

so $\boldsymbol{A} \times \boldsymbol{B}$ is orthogonal to both $\boldsymbol{A}$ and $\boldsymbol{B}$; and

(iii) the dot product

$$\boldsymbol{A} : \boldsymbol{B} = \|\boldsymbol{A}\|\|\boldsymbol{B}\| \cos\alpha, \tag{32}$$

where norm of the cross product,

$$\|\boldsymbol{A} \times \boldsymbol{B}\| = \|\boldsymbol{A}\|\|\boldsymbol{B}\| \sin\alpha, \tag{33}$$

is associated with the same angle α, from which the Pythagorean formula holds:

$$\|\boldsymbol{A} \times \boldsymbol{B}\|^2 = \|\boldsymbol{A}\|^2\|\boldsymbol{B}\|^2 - (\boldsymbol{A} : \boldsymbol{B})^2. \tag{34}$$

As a special case, the triple cross product takes the form

$$(\boldsymbol{A}\times\boldsymbol{B})\times\boldsymbol{A}=(\boldsymbol{A}:\boldsymbol{A})\boldsymbol{B}-(\boldsymbol{B}:\boldsymbol{A})\boldsymbol{A}. \tag{35}$$

Note that the triple cross product identity fails for the cross product defined in this section, however, the Malcev identity (21) is satisfied.

3.2. ***The case of a symmetric and a nonsymmetric second-order tensors.*** It is clear that the preceding definition of a cross product generalizes to the case of one symmetric and one nonsymmetric second-order tensor. Namely, let $\boldsymbol{A}^T\neq\boldsymbol{A}$ be a nonsymmetric second-order tensor, and let $\boldsymbol{B}^T=\boldsymbol{B}$ be a symmetric second-order tensor. Then, the tensor $\boldsymbol{A}$ can be decomposed into its symmetric $\boldsymbol{A}_S$ and skew-symmetric $\boldsymbol{A}_A$ parts, i.e.,

$$\boldsymbol{A}=\boldsymbol{A}_S+\boldsymbol{A}_A, \tag{36}$$

such that

$$\boldsymbol{A}_S=\tfrac{1}{2}(\boldsymbol{A}+\boldsymbol{A}^T),\quad \boldsymbol{A}_A=\tfrac{1}{2}(\boldsymbol{A}-\boldsymbol{A}^T).$$

The tensor $\boldsymbol{A}_A$ has zero diagonal elements and only three independent scalar quantities, given as a, b and c. Hence, the matrix of $\boldsymbol{A}_A$ may be defined in the form

$$[\boldsymbol{A}_A]=\begin{bmatrix}0 & -a & b\\ a & 0 & -c\\ -b & c & 0\end{bmatrix}. \tag{37}$$

The eigenvalues and the eigenvectors of $\boldsymbol{A}_A$ are defined as [Itskov 2015]

$$\lambda_1=0,\quad \lambda_2=\omega i,\quad \lambda_3=-\omega i, \tag{38}$$

and

$$\boldsymbol{A}_A\cdot\boldsymbol{v}_2=\lambda_2\boldsymbol{v}_2,\quad \boldsymbol{v}_3\cdot\boldsymbol{A}_A=-\lambda_3\boldsymbol{v}_3,$$

where

$$\omega=\sqrt{a^2+b^2+c^2}.$$

The spectral representation of $\boldsymbol{A}_A$ takes the form

$$\boldsymbol{A}_A=\omega(\boldsymbol{p}\otimes\boldsymbol{q}-\boldsymbol{q}\otimes\boldsymbol{p}), \tag{39}$$

where

$$\boldsymbol{p}=\tfrac{1}{\sqrt{2}}(\boldsymbol{v}_2+\boldsymbol{v}_3),\quad \boldsymbol{q}=\tfrac{1}{\sqrt{2}}i(\boldsymbol{v}_3-\boldsymbol{v}_2).$$

The vectors $\boldsymbol{p}$ and $\boldsymbol{q}$, by a straightforward manipulation, are given by

$$[\boldsymbol{p}]^T=\frac{1}{\omega\sqrt{b^2+c^2}}[-ac,-ab,b^2+c^2],\quad [\boldsymbol{q}]^T=\frac{1}{\sqrt{b^2+c^2}}[-b,c,0].$$

In addition, we define a third vector

$$\boldsymbol{r}=\boldsymbol{p}\times\boldsymbol{q}. \tag{40}$$

Then, in the coordinate system referred relative to the bases $(\boldsymbol{p}, \boldsymbol{q}, \boldsymbol{r})$, the matrix of tensor $\boldsymbol{A}_A$ becomes

$$[\widetilde{\boldsymbol{A}}_A] = \begin{bmatrix} 0 & \omega & 0 \\ -\omega & 0 & 0 \\ 0 & 0 & 0 \end{bmatrix}, \tag{41}$$

which has the same form as $\boldsymbol{C}_A$ in (29).

Finally, transforming the tensors $\boldsymbol{A}_S$ and $\boldsymbol{B}$ to the same system as in $\widetilde{\boldsymbol{A}}_A$,

$$\widetilde{\boldsymbol{A}}_s = \boldsymbol{Q}^T \boldsymbol{A}_S \boldsymbol{Q}, \quad \widetilde{\boldsymbol{B}} = \boldsymbol{Q}^T \boldsymbol{B} \boldsymbol{Q}, \tag{42}$$

where the first, second and third column of matrix of $\boldsymbol{Q}$ contains the vectors $\boldsymbol{p}$, $\boldsymbol{q}$ and $\boldsymbol{r}$, respectively.

Now, the vectors $\boldsymbol{u}$ and $\boldsymbol{v}$ have the forms

$$[\boldsymbol{u}]^T = [(\widetilde{\boldsymbol{A}}_s)_{11}\ (\widetilde{\boldsymbol{A}}_s)_{22}\ (\widetilde{\boldsymbol{A}}_s)_{33}\ \sqrt{2}(\widetilde{\boldsymbol{A}}_s)_{23} \sqrt{2}(\widetilde{\boldsymbol{A}}_s)_{13}\ \sqrt{2}(\widetilde{\boldsymbol{A}}_s)_{12}\ \sqrt{2}\omega],$$
$$[\boldsymbol{v}]^T = [\widetilde{B}_{11}\ \widetilde{B}_{22}\ \widetilde{B}_{33}\ \sqrt{2}\widetilde{B}_{23}\ \sqrt{2}\widetilde{B}_{13}\ \sqrt{2}\widetilde{B}_{12}\ 0],$$

and the cross product defined previously, using (25) and (18) with $v_7 = 0$ can be determined.

However, the resulting tensor is defined in the rotated system, that is

$$\widetilde{\boldsymbol{A}} \times \widetilde{\boldsymbol{B}} = \widetilde{\boldsymbol{C}}, \tag{43}$$

where $\widetilde{\boldsymbol{A}} = \widetilde{\boldsymbol{A}}_s + \widetilde{\boldsymbol{A}}_A$. In order to complete the procedure, we need to transform the tensor $\widetilde{\boldsymbol{C}}$ back to the original coordinate system. This is accomplished by noting that

$$\boldsymbol{A} \times \boldsymbol{B} = \boldsymbol{C} = \boldsymbol{Q} \widetilde{\boldsymbol{C}} \boldsymbol{Q}^T. \tag{44}$$

It should be noted that our cross product is also applicable for nonsymmetric tensors as long as their skew-symmetric parts have the same eigenvectors. In this case the matrices of tensor $\boldsymbol{A}$ and $\boldsymbol{B}$ are

$$[\boldsymbol{A}] = \begin{bmatrix} A_{11} & A_{12} + \omega_A & A_{13} \\ A_{21} - \omega_A & A_{22} & A_{23} \\ A_{31} & A_{32} & A_{33} \end{bmatrix}, \quad [\boldsymbol{B}] = \begin{bmatrix} B_{11} & B_{12} + \omega_B & B_{13} \\ B_{21} - \omega_B & B_{22} & B_{23} \\ B_{31} & B_{32} & B_{33} \end{bmatrix}, \tag{45}$$

with $A_{ij} = A_{ji}$ and $B_{ij} = B_{ji}$ and vectors $\boldsymbol{u}$ and $\boldsymbol{v}$ are given by

$$[\boldsymbol{u}]^T = [A_{11}\ A_{22}\ A_{33}\ \sqrt{2}A_{23}\ \sqrt{2}A_{13}\ \sqrt{2}A_{12}\ \sqrt{2}\omega_A],$$
$$[\boldsymbol{v}]^T = [B_{11}\ B_{22}\ B_{33}\ \sqrt{2}B_{23}\ \sqrt{2}B_{13}\ \sqrt{2}B_{12}\ \sqrt{2}\omega_B].$$

The cross product, $\boldsymbol{A} \times \boldsymbol{B} = \boldsymbol{C}$, can be calculated by the relations (18), (25) and (27)–(29). The matrix of the resulting tensor is defined by

$$[\boldsymbol{C}] = \begin{bmatrix} C_{11} & C_{12} + \omega_C & C_{13} \\ C_{21} - \omega_C & C_{22} & C_{23} \\ C_{31} & C_{32} & C_{33} \end{bmatrix}, \tag{46}$$

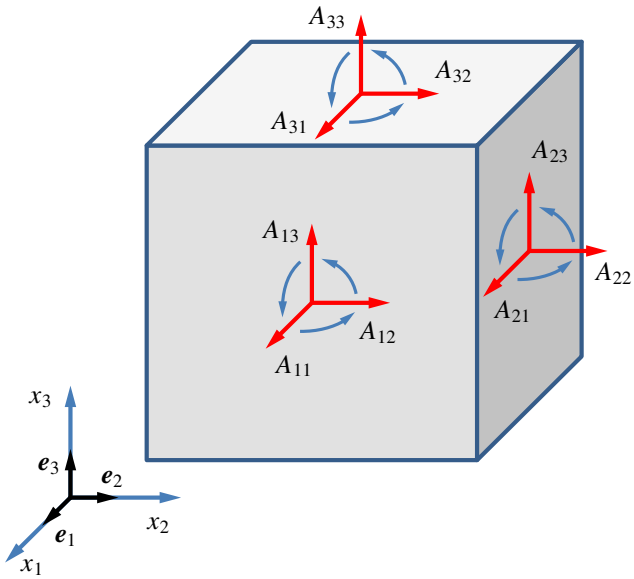

Figure 1. Illustration of the components of a symmetric second-order tensor.

where the components C_{ij}, using (18), are expressed as

$$\begin{aligned}
C_{11} &= A_{22}B_{33} - A_{33}B_{22} + 2(A_{12}B_{13} - A_{13}B_{12} + A_{23}\omega_B - B_{23}\omega_A),\\
C_{22} &= A_{33}B_{11} - A_{11}B_{33} + 2(A_{23}B_{12} - A_{12}B_{23} + A_{13}\omega_B - B_{13}\omega_A),\\
C_{33} &= A_{11}B_{22} - A_{22}B_{11} + 2(A_{13}B_{23} - A_{23}B_{13} + A_{12}\omega_B - B_{12}\omega_A),\\
C_{23} = C_{32} &= A_{12}B_{22} - A_{22}B_{12} + A_{33}B_{13} - A_{13}B_{33} + A_{11}\omega_B - B_{11}\omega_A,\\
C_{13} = C_{31} &= A_{11}B_{12} - A_{12}B_{11} + A_{23}B_{33} - A_{33}B_{23} + A_{22}\omega_B - B_{22}\omega_A,\\
C_{12} = C_{21} &= A_{22}B_{23} - A_{23}B_{22} + A_{13}B_{11} - A_{11}B_{13} + A_{33}\omega_B - B_{33}\omega_A,\\
\omega_C &= A_{11}B_{23} - A_{23}B_{11} + A_{22}B_{13} - A_{13}B_{22} + A_{33}B_{12} - A_{12}B_{33}.
\end{aligned} \tag{47}$$

The cross product formulations (47) can be applied to all the cases introduced in this paper, namely:

(i) when $\boldsymbol{A}$ and $\boldsymbol{B}$ are symmetric ($\omega_A = \omega_B = 0$),

(ii) when $\boldsymbol{A}$ is nonsymmetric but $\boldsymbol{B}$ is symmetric ($\omega_A \neq 0$, $\omega_B = 0$), and

(iii) $\boldsymbol{A}$ and $\boldsymbol{B}$ are nonsymmetric and the skew-symmetric parts of both of them have the same eigenvectors ($\omega_A \neq 0$, $\omega_B \neq 0$).

4. An alternative and equivalent definition

The cross product operation defined in this paper can be introduced in a different way. In many engineering fields, such as solid mechanics, the components of a symmetric second-order tensor (e.g., stress or strain tensors) can be represented on three mutually perpendicular planes, as shown in Figure 1.

Consider the following second-order orthonormal base tensors (see [Itskov 2015; Mehrabadi and Cowin 1990; Moakher and Norris 2006]):

$$\begin{aligned} \boldsymbol{m}_{11} &= \boldsymbol{e}_1 \otimes \boldsymbol{e}_1, \quad \boldsymbol{m}_{22} = \boldsymbol{e}_2 \otimes \boldsymbol{e}_2, \quad \boldsymbol{m}_{33} = \boldsymbol{e}_3 \otimes \boldsymbol{e}_3, \\ \boldsymbol{m}_{23} &\equiv \boldsymbol{m}_{32} = \tfrac{1}{\sqrt{2}}(\boldsymbol{e}_2 \otimes \boldsymbol{e}_3 + \boldsymbol{e}_3 \otimes \boldsymbol{e}_2), \\ \boldsymbol{m}_{13} &\equiv \boldsymbol{m}_{31} = \tfrac{1}{\sqrt{2}}(\boldsymbol{e}_1 \otimes \boldsymbol{e}_3 + \boldsymbol{e}_3 \otimes \boldsymbol{e}_1), \\ \boldsymbol{m}_{12} &\equiv \boldsymbol{m}_{21} = \tfrac{1}{\sqrt{2}}(\boldsymbol{e}_1 \otimes \boldsymbol{e}_2 + \boldsymbol{e}_2 \otimes \boldsymbol{e}_1), \\ \boldsymbol{m}_{\text{skew}} &= \tfrac{1}{\sqrt{2}}(\boldsymbol{e}_1 \otimes \boldsymbol{e}_2 - \boldsymbol{e}_2 \otimes \boldsymbol{e}_1). \end{aligned} \tag{48}$$

These base tensors are associated with the tensor components ($\boldsymbol{m}_{ij} \rightsquigarrow A_{ij}$) and the tensors $\boldsymbol{A}$ and $\boldsymbol{B}$ defined in (45) can be expressed as

$$\boldsymbol{A} = A_{11}\boldsymbol{m}_{11} + A_{22}\boldsymbol{m}_{22} + A_{33}\boldsymbol{m}_{33} + \sqrt{2}(A_{12}\boldsymbol{m}_{12} + A_{13}\boldsymbol{m}_{13} + A_{23}\boldsymbol{m}_{23} + \omega_A \boldsymbol{m}_{\text{skew}}) \tag{49}$$

and

$$\boldsymbol{B} = B_{11}\boldsymbol{m}_{11} + B_{22}\boldsymbol{m}_{22} + B_{33}\boldsymbol{m}_{33} + \sqrt{2}(B_{12}\boldsymbol{m}_{12} + B_{13}\boldsymbol{m}_{13} + B_{23}\boldsymbol{m}_{23} + \omega_B \boldsymbol{m}_{\text{skew}}). \tag{50}$$

The following relationships are crucial for our method. We define the cross product of the base tensors with the right-hand rule as follows.

For $\boldsymbol{m}_{11}$, $\boldsymbol{m}_{22}$ and $\boldsymbol{m}_{33}$:

$$\boldsymbol{m}_{11} \times \boldsymbol{m}_{22} = \boldsymbol{m}_{33}, \quad \boldsymbol{m}_{22} \times \boldsymbol{m}_{33} = \boldsymbol{m}_{11}, \quad \boldsymbol{m}_{33} \times \boldsymbol{m}_{11} = \boldsymbol{m}_{22}. \tag{51}$$

Moreover, for $\boldsymbol{m}_{1i}$, $\boldsymbol{m}_{2i}$ and $\boldsymbol{m}_{3i}$, which are related to three mutually perpendicular planes (Figure 1):

$$\boldsymbol{m}_{1i}\boldsymbol{m}_{1j} = \epsilon_{ijk}\boldsymbol{m}_{1k}, \quad \boldsymbol{m}_{2i}\boldsymbol{m}_{2j} = \epsilon_{ijk}\boldsymbol{m}_{2k}, \quad \boldsymbol{m}_{3i}\boldsymbol{m}_{3j} = \epsilon_{ijk}\boldsymbol{m}_{3k}, \qquad i \in [1, 2, 3], \tag{52}$$

and

$$\boldsymbol{m}_{11} \times \boldsymbol{m}_{23} = \boldsymbol{m}_{\text{skew}}, \quad \boldsymbol{m}_{22} \times \boldsymbol{m}_{31} = \boldsymbol{m}_{\text{skew}}, \quad \boldsymbol{m}_{33} \times \boldsymbol{m}_{12} = \boldsymbol{m}_{\text{skew}}. \tag{53}$$

Then the cross product $\boldsymbol{A} \times \boldsymbol{B} = \boldsymbol{C}$, using (51)–(53), can be defined by

$$\boldsymbol{C} = C_{11}\boldsymbol{m}_{11} + C_{22}\boldsymbol{m}_{22} + C_{33}\boldsymbol{m}_{33} + \sqrt{2}(C_{12}\boldsymbol{m}_{12} + C_{13}\boldsymbol{m}_{13} + C_{23}\boldsymbol{m}_{23} + \omega_C \boldsymbol{m}_{\text{skew}}), \tag{54}$$

and the components C_{ij} and ω_C are listed in (47).

Remark. There are many possible cross products in $\mathbb{R}^7$, namely 480 as shown in [Coxeter 1946; Schray and Manogue 1996], and listed by Barber [2015]. In this analysis, we view the symmetric second-order tensor as a column vector of six components. However, the order of these components is subjective. But, when the cross product of the base tensors with the right-hand rules (51)–(53) is taken into account, the resulting tensor of the cross product is uniquely defined by (47) independently of the order of the elements in vector $\boldsymbol{u}$ and $\boldsymbol{v}$. In other words, a given order of the tensor components $(\cdot)_{ij}$ in seven dimensions is always associated with exactly one multiplication set (triples), $f_{\alpha\beta\gamma}$, which satisfies the right-hand rule for the base tensors.

5. A simple application

As an illustration, the applicability of the newly developed cross product operation is demonstrated by reformulating the constitutive relation of classical elastoplasticity. The deviatoric part of the Prandtl–Reuss equation in elastic-perfectly plastic case is defined by (see, e.g., [Simo and Hughes 1998])

$$\dot{\boldsymbol{s}} = 2G[\dot{\boldsymbol{e}} - \boldsymbol{n}(\dot{\boldsymbol{e}} : \boldsymbol{n})], \tag{55}$$

where $\boldsymbol{s}$ is the deviatoric stress tensor, $\dot{\boldsymbol{e}}$ is the rate of the deviatoric strain and

$$\boldsymbol{n} = \frac{1}{R}\boldsymbol{s}, \quad R = \|\boldsymbol{s}\|, \quad \boldsymbol{n} : \boldsymbol{n} = 1. \tag{56}$$

Equation (55), using the identity (35), can be rewritten as

$$\dot{\boldsymbol{s}} = 2G\boldsymbol{n} \times (\dot{\boldsymbol{e}} \times \boldsymbol{n}). \tag{57}$$

6. Conclusion

We have introduced a cross-product operation between two symmetric second-order tensors. This operation generalizes the classical vectorial cross product from a three-dimensional Euclidean space to symmetric tensor fields. The operation developed here utilizes the vectorial cross product defined on a seven-dimensional vector space. The resulting product tensor is the sum of a symmetric and a skew-symmetric tensor with one parameter, satisfying the usual properties of the vector cross product with the exception of the triple cross product rule. Potential application areas for the tensorial cross product developed here could possibly include computer vision, continuum mechanics and electromagnetism.

Acknowledgement

I would like to thank Professor Tevian Dray (Department of Mathematics, Oregon State University, Corvallis, OR 97331) for several helpful discussions regarding this work.

References

[Altenbach 2012] H. Altenbach, *Kontinuumsmechanik: einfüh-rung in die materialunabhängigen und material-abhängigen Gleichungen*, Springer, Berlin, 2012.

[Baez 2002] J. C. Baez, "The octonions", *Bull. Amer. Math. Soc.* **39**:2 (2002), 145–205.

[Barber 2015] D. Barber, "480 varieties of octonion multiplication", 2015, available at http://tamivox.org/eugene/octonion480/index.html.

[Bisht et al. 2008] P. S. Bisht, S. Dangwal, and O. P. S. Negi, "Unified split octonion formulation of dyons", *Int. J. Theoret. Phys.* **47**:9 (2008), 2297–2313.

[Bonet et al. 2015] J. Bonet, A. J. Gil, and R. Ortigosa, "A computational framework for polyconvex large strain elasticity", *Comput. Methods Appl. Mech. Eng.* **283** (2015), 1061–1094.

[Brown and Gray 1967] R. B. Brown and A. Gray, "Vector cross products", *Comment. Math. Helv.* **42** (1967), 222–236.

[Chauhan and Negi 2011] B. Chauhan and O. Negi, "Octonionic formulation of seven dimensional vector space", *Fund. J. Math. Phys.* **1**:1 (2011), 41–52.

[Coxeter 1946] H. S. M. Coxeter, "Integral Cayley numbers", *Duke Math. J.* **13** (1946), 561–578.

[de Boer 1982] R. de Boer, "Vektor- und Tensorrechnung für Ingenieure", 1982.

[Dray and Manogue 2015] T. Dray and C. A. Manogue, *The geometry of the octonions*, World Scientific, Hackensack, NJ, 2015.

[Ebbinghaus et al. 1991] H.-D. Ebbinghaus, H. Hermes, F. Hirzebruch, M. Koecher, K. Mainzer, J. Neukirch, A. Prestel, and R. Remmert, *Numbers*, Springer, New York, 1991.

[Eckmann 1943] B. Eckmann, "Stetige Lösungen linearer Gleichungssysteme", *Comment. Math. Helv.* **15** (1943), 318–339.

[Fenn 2001] R. Fenn, *Geometry*, Springer, London, 2001.

[Itskov 2015] M. Itskov, *Tensor algebra and tensor analysis for engineers: with applications to continuum mechanics*, 4th ed., Springer, Cham, Switzerland, 2015.

[Massey 1983] W. S. Massey, "Cross products of vectors in higher-dimensional Euclidean spaces", *Amer. Math. Monthly* **90**:10 (1983), 697–701.

[Mehrabadi and Cowin 1990] M. M. Mehrabadi and S. C. Cowin, "Eigentensors of linear anisotropic elastic materials", *Quart. J. Mech. Appl. Math.* **43**:1 (1990), 15–41.

[Moakher and Norris 2006] M. Moakher and A. N. Norris, "The closest elastic tensor of arbitrary symmetry to an elasticity tensor of lower symmetry", *J. Elasticity* **85**:3 (2006), 215–263.

[Rubin 2000] M. Rubin, *Cosserat theories: shells, rods and points*, Kluwer Academic Publishers, Dordrecht, The Netherlands, 2000.

[Schade and Neemann 2009] H. Schade and K. Neemann, *Tensoranalysis*, de Gruyter, Bad Berleburg, Germany, 2009.

[Schray and Manogue 1996] J. Schray and C. A. Manogue, "Octonionic representations of Clifford algebras and triality", *Found. Phys.* **26**:1 (1996), 17–70.

[Shashua and Wolf 2000] A. Shashua and L. Wolf, "Homography tensors: on algebraic entities that represent three views of static or moving planar points", pp. 507–521 in *Computer vision — ECCV 2000: 6th European conference on computer vision proceedings, part I* (Dublin, Ireland), edited by D. Vernon, Springer, Berlin, 2000.

[Shaw 1987] R. Shaw, "Vector cross products in n dimensions", *Int. J. Math. Educ. Sci. Technol.* **18** (1987), 803–816.

[Silagadze 2002] Z. K. Silagadze, "Multi-dimensional vector product", *J. Phys. A* **35**:23 (2002), 4949–4953.

[Simo and Hughes 1998] J. C. Simo and T. J. R. Hughes, *Computational inelasticity*, Interdisciplinary Applied Mathematics **7**, Springer, New York, 1998.

[Steinmann 2015] P. Steinmann, *Geometrical foundations of continuum mechanics: an application to first- and second- order elasticity and elasto-plasticity*, Lecture Notes in Applied Mathematics and Mechanics **2**, Springer, Heidelberg, 2015.

[Young 1993] E. C. Young, *Vector and tensor analysis*, 2nd ed., Monographs and Textbooks in Pure and Applied Mathematics **172**, Marcel Dekker, New York, 1993.

Received 15 Jan 2016. Revised 11 Oct 2016. Accepted 15 Nov 2016.

LÁSZLÓ SZABÓ: szabo@mm.bme.hu
Department of Applied Mechanics, Budapest University of Technology and Economics, Müegyetem rkp. 5, Budapest, 1111, Hungary

JOURNAL OF MECHANICS OF MATERIALS AND STRUCTURES
Vol. 12, No. 2, 2017
dx.doi.org/10.2140/jomms.2017.12.159

FRACTURE IN THREE DIMENSIONS DUE TO DIE MOTION ON CRACK SURFACES: FRAMEWORK FOR STUDY OF CRACK/CONTACT ZONE GEOMETRY

LOUIS M. BROCK

Dynamic steady state growth in 3D of a semi-infinite plane crack in isotropic elastic solids is considered. Growth is driven by the translation of a rigid die between the two crack surfaces. Sliding friction is neglected, but the possibility that crack surfaces resume contact in the wake of the die is considered. Translation and crack growth occur at the same, constant, subcritical speed. An analytical solution is obtained, and a criterion for fracture based on dynamic energy release rate imposed, with kinetic energy included. A nonlinear differential equation for crack edge location and constraint equations result, and together form a framework for study of crack and contact zone geometry.

Introduction

One result of 2D studies of dynamic fracture is an equation of motion for the crack tip [Freund 1990]. In a 3D study, such an equation must describe the contour defined by the crack edge in the crack plane. For the dynamic steady state, this goal is considered in [Brock 2015a] for semi-infinite crack growth in an unbounded solid. [Brock 2015b] extends this effort in two ways:

(a) Per the standard model [Freund 1990], dynamic energy release rate is equated with surface energy.

(b) The standard model is itself modified by the inclusion of kinetic energy [Gdoutos 2005].

As in [Brock 2015a], the crack remains in its original plane, and growth is caused by translation at constant subcritical speed of compression loads on the crack faces. Such growth can be viewed as an example of hydraulic fracture, e.g., [Mastrojannis et al. 1980]. The present article considers fracture driven not by specified crack face loading, but by wedging, i.e., rigid die motion between faces of an initially closed crack.

The 2D, dynamic steady state study of sliding contact, e.g., [Brock and Georgiadis 2000], shows that for subcritical sliding speed the apex of a smooth-contoured, convex rigid die lies within the contact zone. In subsequent 2D studies, e.g., [Brock 2004], semi-infinite crack extension by the wedging action of such a die exhibits the same behavior. Moreover, crack closure (crack surfaces resuming contact in the wake of the die) is possible. This paper considers the same possibility.

The problem statement and governing equations begin the analysis. The unmixed problem for (largely unspecified) discontinuities in displacement and traction over a planar area in the same solid is then addressed. Integral transforms are obtained, and analytical expressions for the inverses applied to the fracture problem. As stated above, sliding contact is frictionless. For purposes of illustration and possible application in future work, however, this part of the analysis incorporates sliding friction. A framework

Keywords: 3D, dynamic, criteria, contact zone, crack edge, kinetic energy.

of equations is developed and its application in the frictionless limit allows study of both crack and contact zone contours.

Problem statement and governing equations

An unbounded isotropic solid is at rest, but contains a closed slit. In Cartesian basis $\boldsymbol{x} = \boldsymbol{x}(x_k),\ k = (1, 2, 3)$ the slit comprises semi-infinite region $(x_3 = 0, x_1 < 0)$ with boundary B_S $(x_1 = 0)$. A rigid die is inserted in the slit, and its shape and placement guarantee symmetry with respect to both the x_1x_2-plane and x_2x_3-plane. The die then translates in the positive x_1-direction at subcritical constant speed V. Translation is opposed by friction, and contact zone A_C with closed boundary B_C forms on each slit face. Fracture occurs so that B_S also moves, and may no longer be rectilinear. Crack closure, i.e., surfaces resume contact [Brock 2004], is allowed in the wake of the die. Thus a crack gap exists in region A_G between B_S and a contour B_C^-, and $A_C \in A_G$. The crack closure region is designated A_C^-, and the nonfractured region ahead of B_S is designated as A_N. Contour B_C^- is also of infinite length, and not necessarily rectilinear. A dynamic steady state ensues, such that (B_S, B_C, B_C^-) no longer change shape but translate in the positive x_1-direction with speed V. Displacement $\boldsymbol{u}(u_k)$ and traction $\boldsymbol{T}(\sigma_{ik})$ do not vary in the moving frame of (B_S, B_C, B_C^-). Basis $\boldsymbol{x}$ is therefore also translated with speed V so that $u_k = u_k(\boldsymbol{x})$, $\sigma_{ik} = \sigma_{ik}(\boldsymbol{x})$ and the (absolute) time derivative $(Df, \dot{f})$ can be written $-V\partial_1 f$. Here $\partial_k f$ signifies x_k-differentiation. For convenience, the origin of $\boldsymbol{x}$ is placed in A_C. Die shape and expectations that (B_S, B_C, B_C^-) do not intersect suggest that contours and contour gradients can be defined by single-valued, continuous functions of (x_1, x_2).

The equations that govern $(\boldsymbol{u}, \boldsymbol{T})$ in the unbounded solid are [Brock 2015a; 2015b]:

$$\nabla \cdot \boldsymbol{T} - \rho V^2 \partial_1^2 \boldsymbol{u} = 0, \tag{1a}$$

$$\frac{1}{\mu}\boldsymbol{T} = \frac{2\nu}{1-2\nu}(\nabla \cdot \boldsymbol{u})\mathbf{1} + \nabla\boldsymbol{u} + \boldsymbol{u}\nabla. \tag{1b}$$

In (1) $(\nabla, \nabla^2, \mathbf{1})$ respectively are gradient, Laplacian, and identity tensor. Constant (μ, ρ, ν) are shear modulus, mass density and Poisson's ratio. Equation (1) embodies the assumption that body forces can be neglected, and uncoupling gives

$$\boldsymbol{u} = \boldsymbol{u}_S + \boldsymbol{u}_D, \tag{2a}$$

$$(\nabla^2 - c^2\partial_1^2)\boldsymbol{u}_S = 0, \qquad (c_D^2\nabla^2 - c^2\partial_1^2)\boldsymbol{u}_D = 0, \tag{2b}$$

$$\nabla \cdot \boldsymbol{u}_S = 0, \qquad \nabla \times \boldsymbol{u}_D = 0. \tag{2c}$$

Dimensionless quantities are also introduced as

$$c = V/V_S, \quad c_D = V_D/V_S = \sqrt{m+1}, \quad m = 1/(1-2\nu). \tag{3a}$$

Here (V_S, V_D) are shear and dilatational wave speeds, and

$$V_S = \sqrt{\mu/\rho}. \tag{3b}$$

Conditions for $x_3 = 0$, $(x_1, x_2) \in (A_N, A_C^-)$ are

$$[u_k] = [\sigma_{3k}] = 0. \tag{4a}$$

Here $[f] = f^{(+)} - f^{(-)}$ and $f^{(\pm)}$ signifies evaluation at $x_3 = 0(\pm)$. Equation (4a) therefore embodies the assumption that slip does not occur in slit closure region A_C^-. Singular behavior of $(\boldsymbol{T}, \nabla \boldsymbol{u})$ is expected near B_S, but not near (B_C, B_C^-). In $A_G - A_C$

$$[\sigma_{3k}] = \sigma_{3k}^{(\pm)} = 0. \tag{4b}$$

Mixed conditions (for infinitesimal deformation) hold in A_C as

$$u_3^{(\pm)} = (\mp)U, \quad [u_1] = [u_2] = 0, \tag{4c}$$

$$\sigma_{31}^{(\pm)} = (\pm)\gamma\sigma_{33}^{(\pm)}, \quad \sigma_{32}^{(\pm)} = 0, \quad [\sigma_{33}] = 0. \tag{4d}$$

Here γ is the (dimensionless) friction coefficient. Function $U(x_1, x_2)$ is defined by shape and orientation of the die, and thus is bounded, continuous and symmetric in x_2. The inhomogeneous Equation (4c) involves bounded terms, and (4c) and (4d) hold in finite region A_C. Solutions $(\boldsymbol{u}, \boldsymbol{T})$ should therefore be finite for $|\boldsymbol{x}| \to \infty$.

Constraints also apply:

(I) Traction in A_C is finite and continuous.

(II) Normal traction is nontensile in (A_C, A_C^-) and tensile near B_C in A_N.

(III) Normal traction in A_C is invariant with respect to resultant compressive force on A_C [Brock 2012].

(IV) The dynamic energy release rate criterion [Freund 1972] governs, with kinetic energy included [Gdoutos 2005; Brock 2015b].

Related problem: translating discontinuities

As in [Brock 2015a; 2015b], an unmixed problem for translation of discontinuities in displacement and traction on the x_1x_2-plane is considered first. Equations (1)–(3) again hold, and the solution is also bounded for $|\boldsymbol{x}| \to \infty$. $([u_k], [\sigma_{3k}])$ vanish for $(x_1, x_2) \notin A_G$, and are piecewise continuous functions of $(x_1, x_2) \in A_G$. Equations (4c) and (4d) are therefore replaced by

$$[u_k] = [\sigma_{3k}] = 0 \quad (x_1, x_2) \notin A_G. \tag{5}$$

For $(x_1, x_2) \in A_G$ components of $[\boldsymbol{u}]$ are bounded, but near B_C components of $[\sigma_{3k}]$ can be singular. The double bilateral transform [Sneddon 1972] is now introduced as

$$\hat{f} = \iint_{12} f(x_1, x_2) \exp(-p_1x_1 - p_2x_2)\, \mathrm{d}x_1\, \mathrm{d}x_2. \tag{6}$$

Symbol 12 signifies integration over the x_1x_2-plane. Application of (6) to (1)–(3) gives

$$\hat{\boldsymbol{u}}_S = \boldsymbol{V}^{(\pm)} \exp(-B|x_3|), \quad \hat{\boldsymbol{u}}_D = \boldsymbol{U}_D^{(\pm)} \exp(-A|x_3|). \tag{7}$$

Superscript $(\pm)$ signifies $x_3 \geq 0$ and $x_3 \leq 0$, respectively, and

$$p_1 V_1^{(\pm)} + p_2 V_2^{(\pm)} (\mp) B V_3^{(\pm)} = 0, \tag{8a}$$

$$(U_D)_1^{(\pm)} = p_1 U_D^{(\pm)}, \quad (U_D)_2^{(\pm)} = p_2 U_D^{(\pm)}, \quad (U_D)_3^{(\pm)} = (\mp) A_{\pm} U_D^{(\pm)}, \tag{8b}$$

$$B = \sqrt{c_1^2 - p_1^2 - p_2^2}, \quad A = \sqrt{c_1^2/c_D^2 - p_1^2 - p_2^2}, \quad c_1 = c p_1. \tag{8c}$$

Here $(V_1^{(\pm)}, V_2^{(\pm)}, U_D^{(\pm)})$ are arbitrary functions of (p_1, p_2), and bounded behavior of (7) as $|x_3| \to \infty$ requires that $\mathrm{Re}(B, A) \geq 0$ in the cut (p_1, p_2)-planes. Use of (5)–(8) gives six equations for finding $(V_1^{(\pm)}, V_2^{(\pm)}, U^{(\pm)})$ in terms of $([\hat{u}_k], [\hat{\sigma}_{3k}])$. Solutions are given in Appendix A by (A.1) and (A.2). Together with the transform of (1b) they generate (A.3).

Transform inversion — general formulas

Equations (4c) and (4d) indicate that application of related problem results to the crack growth problem requires expressions that relate $([u_k], [\sigma_{3k}], \sigma_{3k}^{(+)})$. Therefore (A.3) is subjected to the inversion operation corresponding to (6). This results in three equations of the general form

$$\sum_j \iint_G f_j \, \mathrm{d}\xi_1 \, \mathrm{d}\xi_2 \left(\frac{1}{2\pi i}\right)^2 \iint \mathrm{d}p_1 \, \mathrm{d}p_2 \, C_j \exp[p_1(x_1 - \xi_1) + p_2(x_2 - \xi_2)] = 0. \tag{9}$$

Here $f_j(\xi_1, \xi_2)$ represents $([u_k], [\sigma_{3k}], \sigma_{3k}^{(+)})$ and $C_j(p_1, p_2)$, coefficient of the corresponding transform in (A.3). Subscript G signifies integration over A_G, and the remaining integrals are taken over the entire $\mathrm{Im}(p_1)$- and $\mathrm{Im}(p_2)$-axes. Results in [Brock 2012; 2015a; 2015b] suggest use of transformations

$$p_1 = p \cos\psi, \quad p_2 = p \sin\psi, \tag{10a}$$

$$\begin{bmatrix} x \\ y \end{bmatrix} = \begin{bmatrix} \cos\psi & \sin\psi \\ -\sin\psi & \cos\psi \end{bmatrix} \begin{bmatrix} x_1 \\ x_2 \end{bmatrix}, \quad \begin{bmatrix} \xi \\ \eta \end{bmatrix} = \begin{bmatrix} \cos\psi & \sin\psi \\ -\sin\psi & \cos\psi \end{bmatrix} \begin{bmatrix} \xi_1 \\ \xi_2 \end{bmatrix}. \tag{10b}$$

Here $\mathrm{Re}(p) = 0+$, $|\mathrm{Im}(p), x, y, \xi, \eta| < \infty$ and $|\psi| < \pi/2$. Parameters (p, ψ), $(x, \psi; y = 0)$ and $(\xi, \psi; \eta = 0)$ resemble quasipolar coordinates, i.e.,

$$\mathrm{d}x_1 \, \mathrm{d}x_2 = |x| \, \mathrm{d}x \, \mathrm{d}\psi, \quad \mathrm{d}\xi_1 \, \mathrm{d}\xi_2 = |\xi| \, \mathrm{d}\xi \, \mathrm{d}\psi, \quad \mathrm{d}p_1 \, \mathrm{d}p_2 = |p| \, \mathrm{d}p \, \mathrm{d}\psi. \tag{10c}$$

In (8) and (A.1)–(A.3), quantities (A, B, T, D_R, D_N, D_M) can be written as products of functions of p and, respectively, factors as

$$A = \sqrt{1 - \bar{c}^2/c_D^2}, \quad B = \sqrt{1 - \bar{c}^2}, \quad T = \bar{c}^2 - 2, \tag{11a}$$

$$R = 4AB - T^2, \quad N = 2AB + T, \quad M = 2N + \bar{c}^2 \tag{11b}$$

$$\bar{c} = c \cos\psi. \tag{11c}$$

For $\mathrm{Re}(A, B) \geq 0$ the requirement that $\mathrm{Re}(\sqrt{\pm p}) > 0$ respectively, in the cut p-plane with branches $\mathrm{Im}(p) = 0$, $\mathrm{Re}(p) < 0$ and $\mathrm{Im}(p) = 0$, $\mathrm{Re}(p) > 0$ guarantees that (7) is bounded. However $\mathrm{Re}(A, B) \geq 0$

requires $0 < c < 1$, i.e., translation speed is restricted to range $0 < V < V_S$. Equation (9) assumes the general form

$$\sum_j \frac{1}{i\pi}\int_\Psi C_j\,\mathrm{d}\psi \int_{G\eta}\mathrm{d}\eta\int_{G\xi} f_j\,\mathrm{d}\xi\,\frac{1}{2\pi i}\int\frac{|p|}{p}\,\mathrm{d}p\left(1,\frac{\sqrt{-p}}{\sqrt{p}}\right)\exp p(x-\xi)=0. \tag{12a}$$

Now $f_j = f_j(x,\psi;\eta)$ represents $(\partial[u_k]/\partial\xi, [\sigma_{3k}], \sigma_{3k}^{(+)})$ and $C_j = C_j(\psi)$. Integration is along the positive side $(\mathrm{Re}(p) = 0+)$ of the entire $\mathrm{Im}(p)$-axis, and p-dependence is seen to be of two types. Symbol Ψ signifies integration over range $|\psi| < \pi/2$. Symbols $(G\xi, G\eta)$ signify integration with respect to (ξ,η) over A_G. Performance of the p-integration [Brock 2015a; 2015b] gives

$$\sum_j \int_\Psi C_j\,\mathrm{d}\psi\int_{G\eta}\mathrm{d}\eta\left(f_j,\frac{1}{\pi}\int_{G\xi}\frac{f_j\,\mathrm{d}\xi}{\xi-x}\right)=0. \tag{12b}$$

The first (nonintegral) term in parentheses vanishes for $x \notin G\xi$ and appears for $x \in G\xi$; the integral (second term) is then evaluated in the principal value (vp) sense. It is noted that (A_G, A_C, A_C^-, A_N) and $(\partial[u_k]/\partial\xi, [\sigma_{3k}], \sigma_{3k}^{(+)})$ can be defined completely in terms of (x,ψ), and that

$$f(x,\psi) = -\frac{\partial}{\partial x}\int_{G\eta}\mathrm{d}\eta\int_{G\xi}\mathrm{d}\xi\; f(\xi,\psi)\delta(x-\xi)\delta(\eta). \tag{12c}$$

Here δ is the Dirac function. These results imply that form (12b) is satisfied when

$$\sum C_j(\psi)\left[f_j(x,\psi),\frac{1}{\pi}\int_{G\xi} f_j(\xi,\psi)\frac{\mathrm{d}\xi}{\xi-x}\right]=0.$$

In light of this equality, together with (10)–(12) and (A.3), the three equations in (A.3) give for $x_3 = 0(+)$, $|\psi| < \pi/2$:

$$\frac{\partial}{\partial x}[u_1] = \frac{\cos\psi}{\mu R}[\sigma_{33}] + \frac{2}{\mu R\pi}\int_{GX}\frac{\mathrm{d}\xi}{\xi-x}\big[g_1(\sigma_{31}^{(+)} - [\sigma_{31}]/2) + g_{12}(\sigma_{32}^{(+)} - [\sigma_{32}]/2)\big], \tag{13a}$$

$$\frac{\partial}{\partial x}[u_2] = \frac{\sin\psi}{\mu R}[\sigma_{33}] + \frac{2}{\mu R\pi}\int_{GX}\frac{\mathrm{d}\xi}{\xi-x}\big[g_{12}(\sigma_{31}^{(+)} - [\sigma_{31}]/2) + g_2(\sigma_{32}^{(+)} - [\sigma_{32}]/2)\big], \tag{13b}$$

$$\frac{\partial}{\partial x}[u_3] = \frac{N}{\mu R}\big[[\sigma_{31}]\cos\psi + [\sigma_{32}]\sin\psi\big] - \frac{2\bar{c}^2 A}{\mu R\pi}\int_{GX}\frac{\mathrm{d}\xi}{\xi-x}(\sigma_{33}^{(+)} - [\sigma_{33}]/2), \tag{13c}$$

$$g_1 = M/B\sin^2\psi + \bar{c}^2 B,\quad g_2 = M/B\cos^2\psi + \bar{c}^2 B,\quad g_{12} = -M/B\sin\psi\cos\psi. \tag{13d}$$

Subscript GX signifies integration over those segments of $G\xi$ in which integrand terms do not vanish. In (11) and (13), R is the Rayleigh function, where $R \to 0+$ $(\bar{c} = 0)$, $R = -1$ $(\bar{c} = 1)$ and $R = 0$ $(\bar{c} = c_R,\ 0 < c_R < 1)$. Term $\bar{c} < c$ for $|\psi| < \pi/2$ in (11c), so that restriction $0 < V < V_R$ now applies, where $V_R = c_R V_S$ is the Rayleigh speed.

Basic solution to crack growth problem

In view of (5), (10) and conditions (4) imposed on (A_G, A_C) and (B_S, B_C, B_C^-), the geometry of these regions on $x_3 = 0$ can be defined for $|\psi| < \pi/2$ as

$$A_C : -r_-(\psi) < x < r_+(\psi), \tag{14a}$$

$$A_G : -r_C^-(\psi) < x < r_S(\psi), \tag{14b}$$

$$A_G - A_C : -r_C^-(\psi) < x < -r_-(\psi),\ r_+(\psi) < x < r_S(\psi), \tag{14c}$$

$$A_C^- : x < -r_C^-(\psi), \quad A_N : x > r_C(\psi). \tag{14d}$$

Here $(r_\pm, r_S, r_C^-) > 0$, and a continuous boundary B_C requires that $r_+(\pm\pi/2) = r_-(\mp\pi/2)$. In view of, e.g., [Brock 2004], it is reasonable to expect that $(r_S, r_C^-) \gg r_\pm$, but this expectation plays no role until the basic solution is illustrated for a specific die geometry. Equations (4) and (10) indicate that for $x_3 = 0(+)$, $|\psi| < \pi/2$

$$A_C : [\sigma_{32}] = [\sigma_{33}] = \sigma_{32}^{(+)} = 0, \quad \frac{\partial}{\partial x}[u_1] = \frac{\partial}{\partial x}[u_2] = 0, \tag{15a}$$

$$A_G - A_C : [\sigma_{3k}] = \sigma_{3k}^{(+)} = 0, \qquad k = (1, 2, 3), \tag{15b}$$

$$(A_C^-, A_N) : [\sigma_{3k}] = \frac{\partial}{\partial x}[u_k] = 0, \qquad k = (1, 2, 3). \tag{15c}$$

In addition, properties assumed for the die suggest that

$$A_N : \sigma_{31}^{(+)} = \sigma_{32}^{(+)} = 0, \tag{16a}$$

$$A_C : [u_3] = 2u_3^{(+)}, \quad [\sigma_{31}] = 2\sigma_{31}^{(+)}. \tag{16b}$$

Equations (13a) and (13b) are thus satisfied when $([u_1], [u_2]) \equiv 0$. Notation $(\sigma_{33}^{(\pm)} \to \sigma, \xi \to t)$ is introduced in (13c), which in view of (4c) and (10) gives

$$A_C^- : (vp)\int_{C-} \frac{\sigma\, dt}{t-x} + \int_C \frac{\sigma\, dt}{t-x} + \int_N \frac{\sigma\, dt}{t-x} = 0, \tag{17a}$$

$$A_0 : -\frac{2\bar{c}^2 A}{\mu R\pi}\left[\int_{C-} \frac{\sigma\, dt}{t-x} + (vp)\int_C \frac{\sigma\, dt}{t-x} + \int_N \frac{\sigma\, dt}{t-x}\right] + \frac{2N}{\mu R}\gamma\sigma\cos\psi = -2\frac{\partial U}{\partial x}, \tag{17b}$$

$$A_N : \int_{C-} \frac{\sigma\, dt}{t-x} + \int_C \frac{\sigma\, dt}{t-x} + (vp)\int_N \frac{\sigma\, dt}{t-x} = 0. \tag{17c}$$

Subscripts $(C-, C, N)$ respectively signify integration over range $t < -r_C^-$, $-r_- < t < r_+$ and $t > r_S$. Solution of set (17) for $(x, \psi) \in A_C$ and $(x, \psi) \in (A_C^-, A_N)$ respectively, is

$$\frac{\sigma}{\mu} = \frac{R}{S}\left[\frac{\partial U}{\partial x}\cos\pi\Omega + \sin\pi\Omega\sqrt{\frac{x + r_C^-}{r_S - x}}\,\frac{(r_+ - x)^{1+\Omega}}{(x + r_-)^\Omega}(vp)\,Q_C\left(\frac{\partial U}{\partial x}; x\right)\right], \tag{18a}$$

$$\frac{\sigma}{\mu} = \frac{R}{S}\sqrt{\frac{x+r_C^-}{x-r_S}}\frac{(x-r_+)^{1+\Omega}}{(x+r_-)^{\Omega}}\,Q_C\Big(\frac{\partial U}{\partial x};x\Big), \tag{18b}$$

$$Q_C(f;\xi) = \frac{1}{\pi}\int_C f\sqrt{\frac{r_S-t}{t+r_C^-}}\frac{(t+r_-)^{\Omega}}{(r_+-t)^{1+\Omega}}\frac{\mathrm{d}t}{t-\xi}. \tag{18c}$$

Equation (18a) satisfies constraint I when

$$\int_C \frac{\partial U}{\partial t}\sqrt{\frac{r_S-t}{t+r_C^-}}\Big(\frac{t+r_-}{r_+-t}\Big)^{\Omega}\frac{\mathrm{d}t}{t-r_+} = 0. \tag{18d}$$

In (18a) and (18b) terms (Ω, S) are defined as

$$\Omega = -\tfrac{1}{2}+\Gamma < 0, \quad \Gamma = \frac{1}{\pi}\tan^{-1}\Big(\frac{-\gamma N\cos\psi}{\bar{c}^2 A}\Big) > 0, \tag{19a}$$

$$S = \sqrt{(\gamma N\cos\psi)^2 + (\bar{c}^2 A)^2}. \tag{19b}$$

For $r_+ < x < r_S$ and $-r_C^- < x < -r_-$ respectively in $A_G - A_C$

$$\frac{\partial}{\partial x}[u_3] = \frac{2\bar{c}^2 A}{S}\sqrt{\frac{x+r_C^-}{r_S-x}}\frac{(x-r_+)^{1+\Omega}}{(x+r_-)^{\Omega}}\,Q_C\Big(\frac{\partial U}{\partial x};x\Big), \tag{20a}$$

$$\frac{\partial}{\partial x}[u_3] = -\frac{2\bar{c}^2 A}{S}\sqrt{\frac{x+r_C^-}{r_S-x}}\frac{(r_+-x)^{1+\Omega}}{(-x-r_-)^{\Omega}}\,Q_C\Big(\frac{\partial U}{\partial x};x\Big). \tag{20b}$$

Knowledge of $([u_3], \partial_1[u_3])$ for $r_+ < x < r_S$ will be required. Equations (10) and (20a) provide ingredients for this with

$$[u_3] = -\frac{2\bar{c}^2 A}{S\pi}\int_C \frac{\partial U}{\partial t}\,\mathrm{d}t\sqrt{\frac{r_S-t}{t+r_C^-}}\frac{(t+r_-)^{\Omega}}{(r_+-t)^{1+\Omega}}\int_+\sqrt{\frac{\tau+r_C^-}{r_S-\tau}}\frac{(\tau-r_+)^{1+\Omega}}{(\tau+r_-)^{\Omega}}\frac{\mathrm{d}\tau}{\tau-t}, \tag{21a}$$

$$\partial_1 f = \cos\psi\frac{\partial f}{\partial x} - \frac{\sin\psi}{|x|}\frac{\partial f}{\partial \psi}, \quad \partial_2 f = \sin\psi\frac{\partial f}{\partial x} + \frac{\cos\psi}{|x|}\frac{\partial f}{\partial \psi}. \tag{21b}$$

Symbol + signifies integration over range $x < \tau < r_S$. As is appropriate, (21a) vanishes for $x \to r_S-$.

Constraint (I, II, III): preliminary observations

Contour parameters $r_\pm(\psi)$, $r_S(\psi)$ and $r_C^-(\psi)$ remain to be determined. Equation (18d) provides one equation, and (18a) must satisfy (unilateral) constraint II. If such is indeed the case, the resultant force on each contact zone A_C is

$$-\int_\Psi \mathrm{d}\psi\int_C |x|\sigma(x,\psi)\,\mathrm{d}x. \tag{22a}$$

Constraint III requires that σ be invariant with respect to the force, i.e., for arbitrary $(\delta x, \delta\psi)$

$$\delta\sigma = \frac{\partial\sigma}{\partial x}\delta x + \frac{\partial\sigma}{\partial\psi}\delta\psi = 0. \tag{22b}$$

Therefore for $-r_- < x^* < r_+$

$$\frac{\partial \sigma}{\partial x}(x^*, \psi) = 0, \quad \frac{\partial \sigma}{\partial \psi}(x^*, \psi) = 0. \tag{22c}$$

Equation (22) is examined below in terms of specific die geometry (U).

Constraint IV: dynamic energy release rate

In this study kinetic energy is considered [Brock 2015b; Gdoutos 2005]. Nevertheless known procedures, e.g., [Freund 1972], can be used to derive the balance equation required by constraint IV:

$$D \iint_G e_G \, \mathrm{d}x_1 \, \mathrm{d}x_2 = \iint_0 [\sigma_{3k} \dot{u}_k] \, \mathrm{d}x_1 \, \mathrm{d}x_2 + D \iiint_{123} \frac{\rho}{2} \dot{u}_k \dot{u}_k \, \mathrm{d}x_1 \, \mathrm{d}x_2 \, \mathrm{d}x_3. \tag{23}$$

Subscript 123 signifies integration over the unbounded solid. Subscript 0, integration over a thin strip that straddles crack edge B_S and subscript G, integration over gap surface A_G. Term e_G is the surface energy per unit area of A_G, and is treated as constant [deBoer et al. 1988; Skriver and Rosengaard 1992; Freund 1990]. The presence of operators $(\dot{f}, Df)$ signifies fixed basis $\boldsymbol{x}$. Use of translating basis $\boldsymbol{x}$ and Green's theorem [Malvern 1969], imposition of the dynamic steady state, and use of (10) give for the first term in (23),

$$V e_G \int_\Psi \sqrt{r_S^2 + (r_S')^2} \cos\psi \, \mathrm{d}\psi. \tag{24a}$$

Here f' signifies $\mathrm{d}f/\mathrm{d}\psi$ and it is noted that the radical in (24a) can be written as

$$r_S \sqrt{D_S^2 + D_C^2}, \tag{24b}$$

with

$$D_S = \frac{1}{r_S}(r_S \sin\psi)', \quad D_C = \frac{1}{r_S}(r_S \cos\psi)'. \tag{24c}$$

Because $([u_1], [u_2]) \equiv 0$, use of (10) gives for the second integral in (23),

$$\mu V \int_\Psi \mathrm{d}\psi \int_-^+ |x| \, \mathrm{d}x \, \sigma \partial_1 [u_3]. \tag{25}$$

Here $\pm$ signifies integration limits $r_S \pm$. Term $(\sigma, [u_3]) = 0$ for $r_+ < x < r_S$ and $x > r_S$, respectively. In view of (18b) and (20a), however:

$$\frac{\sigma}{\mu} \approx \frac{R}{S} \frac{G_C}{\pi \sqrt{x - r_S}} \; (x \to r_S+), \tag{26a}$$

$$\frac{\partial}{\partial x}[u_3] \approx -\frac{2\bar{c}^2 A}{S} \frac{G_C}{\pi \sqrt{r_S - x}} \; (x \to r_S-), \tag{26b}$$

$$G_C = \sqrt{l_G} \frac{(r_S - r_+)^{1+\Omega}}{(r_S + r_-)^\Omega} \int_C \frac{\partial U}{\partial t} \frac{(t + r_-)^\Omega}{(r_+ - t)^{1+\Omega}} \frac{\mathrm{d}t}{\sqrt{t + r_C^-} \sqrt{r_S - t}}, \quad l_G = r_S + r_C^-. \tag{26c}$$

Equation (26a) must give positive σ (constraint II), and this requires that $G_C > 0$. Distance between B_S and B_C^-, measured along a line passing through $(x_1, x_2) = 0$, is l_G. In view of (21b), $\partial_1[u_3]$ exhibits (26b), but also the derivative of (21a) with respect to ψ. Chain/product-rule differentiation is required for

this. Quantity U and parameters involving $(\Omega, \bar{c})$ are given functions of ψ, but $(r_\pm, r_S, r_C^-)$ are not. For $x \to r_S-$ however, the dominant contribution involves r_S', and $\partial[u_3]/\partial r_S = -\partial[u_3]/\partial x$. Equation (21b) then gives

$$\partial_1[u_3] \approx -\frac{2\bar{c}^2 A}{S} \frac{G_C D_S}{\pi\sqrt{r_S - x}} \ (x \to r_S-). \tag{27a}$$

In view of (26a) and (27a) the x-integrand exhibits Dirac function $\delta(x - r_S)$ [Freund 1972], so that (25) gives

$$\frac{\mu V}{2\pi} \int_\Psi \mathrm{d}\psi \ \frac{R}{S} G_C^2 r_S D_S. \tag{27b}$$

Singular behavior as $x \to r_S$ and rapid decay as $|x| \to \infty$ seen in (26) are manifest in $\nabla \boldsymbol{u}$ generally. Therefore integration in the third term in (23) can be confined to a tube of radius $r_B \to 0$ that encloses B_S. Term $\dot{u}_k = -V\partial_1 u_k$ in translating basis $\boldsymbol{x}$ for the dynamic steady state, and 3D expressions for $\sqrt{(x - r_S)^2 + x_3^2} < r_B$, $|\psi| < \pi/2$ are required. Equations (A.1) and (7) lead to $\hat{\boldsymbol{u}}(p_1, p_2, x_3)$, and relevant components are given in Appendix B. In light of (B.1) and (10), $(\partial(u_i)_D/\partial x, [u_k], [\sigma_{3k}])$ are related by three equations of general form (compare (12a)):

$$\sum_j C_j \frac{\partial}{\partial x} \int_{GX} \mathrm{d}\xi \ f_j \int \frac{|p|}{p} \mathrm{d}p \left(\frac{x_3}{|x_3|}, \frac{\sqrt{-p}}{\sqrt{p}} \right) \exp[p(x - \xi) - A\sqrt{-p}\sqrt{p}|x_3|] = 0. \tag{28}$$

The integration range for $f_j = \partial(u_i)_D/\partial x$ is $|\xi - r_S| < r_B$, for $f_j = [u_k]$ is $r_+ < \xi < r_S$ and for $f_j = [\sigma_{3k}]$ is $-r_- < \xi < r_+$. Three similar equations in terms of $\partial(u_i)_S$, with A replaced by B, follow from (B.2). Integration with respect to p [Brock 2015a; 2015b] and use of (10) give expressions $\partial u_k/\partial x$ that are valid for $(|x_3| \approx 0, x \to r_S-)$. The results for $x_3 \approx 0(+)$ are given in Appendix C by (C.1)–(C.3). Expressions for $\partial_1[u_3](|x_3| \approx 0, x \to r_S-)$ can then be developed in a manner similar to that involving $\partial_1 u_k$. The last term in (23) entails integration over the tube with radius $r_B \to 0$. A standard polar coordinate system (r, ϕ), centered on B_C, is therefore defined for given ψ in the xx_3-plane by

$$r = \sqrt{(x - r_S)^2 + x_3^2}, \quad \phi = \tan^{-1} \frac{x_3}{x - r_S} (|\phi| < \pi). \tag{29}$$

Combining (24b), (24c), (26) and (29) with the formulas based on (C.1)–(C.3) and corresponding formulas for $x_3 \le 0$ results in (C.4). Use of Green's theorem [Malvern 1969] in the dynamic steady state with translating basis $\boldsymbol{x}$ produce for the last term in (23) an integral over the tube surface. Use of (C.4) and (C.5) then gives for this term

$$-\mu V \int_\Psi \mathrm{d}\psi \ r_S \sqrt{D_S^2 + D_C^2} \left(\frac{\bar{c}^3 A}{\pi S} G_C D_S \right)^2 \int_\Phi E \cos\phi \, \mathrm{d}\phi, \tag{30a}$$

with

$$E = \left(\frac{TA_+}{2AA_\Phi} + \frac{BB_+}{B_\Phi} \right)^2 + \left(\frac{TA_-}{2AA_\Phi} + \frac{B_-}{B_\Phi} \right)^2. \tag{30b}$$

Symbol Φ signifies integration over range $|\phi| < \pi$. Parameter $\bar{c} \le c < c_R < 1$. Therefore, for speeds V which are rapid but well below Rayleigh value $V_R = c_R V_S$, first order expansions for (A, B) in (11c)

and (A_Φ, B_Φ) in (C.5) allow approximations

$$E = 2\bar{c}^4 \sin^2\frac{\phi}{2}\left[\frac{1}{c_D^4} + 4\Big(1-\frac{1}{c_D^2}\Big)^2 \sin^4\frac{\phi}{2}\cos^2\phi\right] + O(\bar{c}^6), \tag{31a}$$

$$\int_\Phi E\cos\phi\,\mathrm{d}\phi = -\pi c_1^4 E_\Phi, \quad E_\Phi = \frac{1}{4}\left[\frac{1}{c_D^4} + \frac{23}{8}\Big(1-\frac{1}{c_D^2}\Big)^2\right]. \tag{31b}$$

Equations (24), (27) and (30a) all involve integration with respect to ψ and exhibit speed V as factor, so that (23), (24a), (27b), (30a) and (31) give

$$\cos\psi\sqrt{D_S^2 + D_C^2} - P_C G_C^2 M D_S = 0, \tag{32a}$$

$$P_C = \frac{\mu}{\pi e_G}\frac{R}{2S}, \quad M = 1 + 2\frac{(\bar{c}^2 A)^2}{SR}\bar{c}^2 E_\Phi D_S\sqrt{D_S^2 + D_C^2}. \tag{32b}$$

For $|\psi| < \pi/2$, (32a) and (24c) define a nonlinear differential equation for $r_S(\psi)$, but parameters $r_C^-(\psi)$ and $r_\pm(\psi)$ are also involved. Equation (18c) and continuity requirements $r_+(\pm\pi/2) = r_-(\mp\pi/2)$ also serve as constraints upon (32a).

Comment on effects of kinetic energy

In the limit as $\bar{c} \to 0$

$$\frac{\bar{c}^2 A}{S} \to 1, \quad 2\frac{\bar{c}^2 A}{R} \to \frac{c_D^2}{c_D^2 - 1}. \tag{33}$$

Thus the effect of kinetic energy (E_Φ) in (32a) is proportional to $\bar{c}^2$, i.e., V^2. The term M is a magnification factor for this effect. Setting $M = 1$ in (32a) leads for $|\psi| < \pi/2$ to

$$D_S - \frac{D_C\cos\psi}{\sqrt{P_G^2 - \cos^2\psi}} = 0 \quad (P_G = P_C G_C^2 > \cos\psi). \tag{34}$$

Particular case: disk-shaped die

Consider the die to be a disk in the shape of ellipsoid of revolution

$$x_1^2 + x_2^2 + C_3 x_3^2 = r_0^2,$$

where $(C_3 \gg 1)$. Length r_0 is the disk radius, and there should be clearance between disk edge and (B_S, B_C^-). Moreover span l_C of A_C is assumed to be small. Thus for $|\psi| < \pi/2$

$$l_C = r_+ + r_- \ll 2r_0, \quad (r_S, r_C^-) > r_0. \tag{35a}$$

In view of (4c) and (10)

$$\frac{\partial U}{\partial x} = -\frac{x}{\sqrt{C_3} r_0}. \tag{35b}$$

If the expectation that $(r_S, r_C^-) \gg r_\pm$ is now also imposed, series expansions for functions of $(r_S, r_C^-, r_\pm)$ can be introduced. In particular integration in (18d) and (26c) can be performed analytically, and constraint I and key parameter G_C have asymptotic forms

$$r_+ + \Omega l_C - 1/2 r_S(1 + r_S/r_C^-)\big[(r_+ + \Omega l_C/2)(r_+ + \Omega l_C) + \tfrac{3}{2}\Omega l_C r_-\big] = 0, \tag{36a}$$

$$G_C = \sqrt{r_S/C_3}\sqrt{1 + r_S/r_C^-}\,\frac{\pi S}{\bar{c}^2 A r_0}(D_0 I_0 + D_1 I_1 + D_2 I_2). \tag{36b}$$

The (D, I)-terms in (36b) are given in Appendix D. Letting $(r_S, r_C^-) \to \infty$ for $|\psi| < \pi/2$ in (36a) gives the result found for sliding on a half-space by an axially symmetric die [Brock 2012]:

$$r_+ = -\Omega l_C, \quad r_- = (1 + \Omega) l_C. \tag{37}$$

Use of (35b) and (36b) in (22) yield asymptotic results $x^* + r_- + \Omega l_C = 0$ and

$$\sigma(x^*) = \sigma^* = -\frac{\mu R}{S\sqrt{C_3}}\frac{l_C(1+\Omega)^{1+\Omega}}{r_0(-\Omega)^\Omega}\left[1 + \frac{1}{2r_S}(1 + r_S/r_C^-)(r_+ + \Omega l_C)\right]. \tag{38}$$

The right hand side of (38) is negative, in accordance with constraint II. Constraint III requires that (38) be invariant for $|\psi| < \pi/2$.

For the disk, the framework developed for study is now seen to consist of:

(a) Properties of the disk (r_0, C_3, c), disk-solid (γ) and solid, e.g., (μ, c_D, c_R, e_G).

(b) Values of c such that V is well below V_R, but not negligible.

(c) For these inputs, formulas for parameters $(r_\pm, r_S, r_C^-)$ are to be determined from (32)–(38), Appendix D and invariance of (38). As is noted at the outset, this paper considers frictionless sliding contact. This does not mean that friction is a negligible effect: parameter Ω in (19a) plays a key role in solution formulas derived above, and calculations in Table 1 for various c and (γ, ψ) suggest that friction effects, while small, become noticeable as sliding/crack growth speed V increases. For purposes of illustrating the use of the framework, and to take advantage of the low-speed kinetic

$(\psi, \gamma)\downarrow$ $c\rightarrow$	0.05	0.1	0.2	0.3
$(\psi, 0)$	−0.5	−0.5	−0.5	−0.5
$(0°, 0.2)$	−0.48424	−0.48399	−0.48367	−0.48306
$(0°, 0.4)$	−0.46855	−0.46807	−0.46742	−0.46621
$(30°, 0.2)$	−0.48634	−0.48608	−0.48594	−0.48556
$(30°, 0.4)$	−0.47274	−0.47221	−0.47194	−0.47118
$(45°, 0.2)$	−0.48813	−0.48868	−0.48861	−0.4884
$(45°, 0.4)$	−0.47629	−0.47739	−0.47725	−0.47682
$(60°, 0.2)$	−0.49211	−0.49212	−0.49201	−0.49192
$(60°, 0.4)$	−0.48422	−0.48424	−0.48403	−0.48385
$(90°, \gamma)$	−0.5	−0.5	−0.5	−0.5

Table 1. Parameter Ω for various c and (ψ, γ).

energy parameter result (31b) however, calculations for the disk are now presented for the case $\Omega = -0.5$ ($\gamma = 0$).

Crack/contact zone contours: key equations

The algebraic manipulations involved in studying the geometry of crack and contact zone contours with the formulas derived thus far are simpler if performed, in part, in terms of parameters

$$l_C = r_+ + r_-, \quad d_C = r_+ - r_-, \quad \beta = r_S/r_C^-. \tag{39}$$

Equations (36a) and (38) now give for $|\psi| < \pi/2$,

$$\frac{l_C}{r_0} = \chi/3[1 + 2\beta - (1+\beta/2)\sqrt{1+\beta}\sqrt{(\chi r_0)/(6r_S)}\,], \tag{40a}$$

$$\frac{d_C}{r_0} = -\tfrac{3}{16}(\chi/3)^2(1+\beta)(1+2\beta)^2 r_0/r_S, \tag{40b}$$

$$\chi = \frac{2\bar{c}^2 A}{\mu R}\sqrt{C_3}|\sigma^*|(\chi, r_0/r_S) < 1. \tag{40c}$$

In appropriate fashion $(l_C, d_C, r_\pm) = 0$ when $|\sigma^*| = 0$ ($\chi = 0$). The quantity $d_C = 0$ when $r_S \to \infty$, a result consistent with (37) when $\gamma = 0$. Use of (36a), (39) and (40) in (32) when $\gamma = 0$ gives for $|\psi| < \pi/2$:

$$\cos\psi\sqrt{D_S^2 + D_C^2} - PMr_0/r_S D_S = 0. \tag{41}$$

In (41) we have

$$M = 1 + \frac{2\bar{c}^4 A}{R} E_\Phi D_S \sqrt{D_S^2 + D_C^2}, \tag{42a}$$

$$P = \frac{\pi}{C_3}\frac{\mu r_0}{e_G}\frac{R}{2\bar{c}^2 A}(\chi/4)^4 F(\beta)\left(P\frac{r_0}{r_S} > \cos\psi\right), \tag{42b}$$

$$F(\beta) = (\tfrac{2}{3}\beta)^2(1+\beta)(1+2\beta)^4. \tag{42c}$$

For $\psi = 0$ (41) and (42) give

$$\frac{r_S}{r_0} = P_1 M_1, \quad \frac{r_C^-}{r_0} = \frac{r_S}{\beta_1 r_0}\left(\frac{r_S}{r_0}, \frac{r_C^-}{r_0}\right) > 1, \tag{43a}$$

$$M_1 = 1 + \frac{2c^4 A_1}{E_\Phi}, \tag{43b}$$

$$P_1 = \frac{\pi}{C_3}\frac{\mu r_0}{e_G}\frac{R_1}{2c^2 A_1}(\chi_1/4)^4 F(\beta_1), \quad \chi_1 = \frac{2c^2 A_1}{\mu R_1}\sqrt{C_3}|\sigma^*| < 1. \tag{43c}$$

Subscript 1 signifies that $\bar{c} \to c$ in (11a) and (11b).

For $|\psi| \to \pi/2$,

$$r_S \approx \frac{h_S}{\cos\psi}, \quad r_C^- \approx \frac{h_C^-}{\cos\psi}, \tag{44a}$$

$$\frac{h_S}{r_0} = P_2 M_2, \quad \frac{h_C^-}{r_0} = \frac{h_S}{\beta_2 r_0}, \tag{44b}$$

$$M_2 = 1 + \frac{c_D^2 c^2}{c_D^2 - 1} E_\Phi, \tag{44c}$$

$$P_2 = \frac{\pi}{C_3}\frac{\mu r_0}{e_G}(1 - 1/c_D^2)^3 \left(\frac{\sqrt{C_3}}{4\mu}|\sigma^*|\right)^4 F(\beta_2). \tag{44d}$$

Subscript 2 signifies that $\bar{c} \to 0$ in (11).

Equations (10) and (44) show that points on (B_S, B_C^-) approach rectilinear asymptotes that parallel the x_2-axis at great distances from the path of the die. That is,

$$B_S : x_1 \to h_C, \qquad |x_2| \to \infty, \tag{45a}$$

$$B_C^- : x_1 \to -h_C^-, \quad |x_2| \to \infty. \tag{45b}$$

Term M in (32) and (42a) is the magnification factor for the effect of kinetic energy, and (M_1, M_2) are limit cases. To illustrate their behavior, consider a generic solid with properties [Brock and Georgiadis 2000; deBoer et al. 1988; Skriver and Rosengaard 1992]:

$$\mu = 79\,\text{GPa}, \qquad |\sigma_Y| = 250\,\text{MPa}, \qquad e_G = 2.2\,\text{J/m}^2$$
$$V_S = 3094\,\text{m/s}, \qquad c_D = 2.0, \qquad c_R = 0.933.$$

Here $|\sigma_Y|$ is the magnitude of the yield stress in compression. Calculations of (43b) and (44c), based on these properties, are given in Table 2 for various values of c. Entries show that the kinetic energy effect in M_1 and M_2 reaches 17% and 14%, respectively, when $V = 0.536 V_R$. In view of (31) therefore, subsequent calculations are restricted to range $0 < c < 0.5$.

Crack/contact zone contours: calculations

Table 2 indicates that kinetic energy is a perturbation in the study of crack and contact zone contours for $\psi = 0$ and $|\psi| \to \pi/2$. Equation (34) and rearrangement of (32a) however show that kinetic energy serves as a singular perturbation in the governing differential equation for $0 < |\psi| < \pi/2$,

$$D_C^2 + \left[\left(\frac{r_S}{r_0 P}\cos\psi - \frac{2\bar{c}^4 A}{R} E_\Phi D_S^2\right)^2 - 1\right] D_S^2 = 0. \tag{46a}$$

c	0.05	0.1	0.2	0.5
M_1	1.00139	1.00563	1.02304	1.1734
M_2	1.0014	1.0056	1.0224	1.1394

Table 2. Parameters (M_1, M_2) for various c.

c	0.05	0.1	0.2	0.4	0.5
C_3^*	$5.67(10^4)$	$5.56(10^4)$	$5.34(10^4)$	$4.36(10^4)$	$3.65(10^4)$

Table 3. C_3^* ($\chi_1 = 1$, $|\sigma^*| = |\sigma_Y|$).

Study of (46a) near $\psi \approx 0$ for a given ratio $\beta = r_S/r_C^-$ suggests asymptotic solution

$$\frac{r_S}{r_0} \approx \frac{\mu r_0}{C_3 e_G} \frac{\pi F(\beta_1)}{\cos\psi} \left(\frac{\chi_1}{4}\right)^4 \left(\frac{R_1}{2c^2 A_1} + c^2 E_\Phi\right). \tag{46b}$$

This result agrees with (43) at $\psi = 0$ and approximates the asymptotic behavior of (43a) for $|\psi| \to \pi/2$. In view of (10) therefore asymptotic formulas for contours (B_S, B_C^-) are, respectively

$$\sqrt{x_1^2 + x_2^2} \approx r_S \ (x_1 > 0), \quad \sqrt{x_1^2 + x_2^2} \approx r_C^- \ (x_1 < 0). \tag{46c}$$

Equations (44a) and (46c) suggest a results similar to that described in [Brock 2015b]. The crack gap lies in a band which bulges outward from the die along its path, but forms a strip of finite width far away from the path.

Results (43)–(45) and related calculations for $\psi = 0$ and $|\psi| \to \pi/2$ by themselves allow insight into contour geometry. Parameter σ^* is the maximum compressive stress in contact zone A_C formed by the disk, and for the ellipsoidal disk, $1/\sqrt{C_3}$ is the disk thickness-diameter ratio. These are coupled in (χ, χ_1), where $\chi_1 > \chi$ $(0 < |\psi| < \pi/2)$. Analysis is elastic, so $|\sigma^*| < |\sigma_Y|$, and approximation (40) requires that $\chi < 1$. Limit case ($\chi_1 = 1$, $|\sigma^*| = |\sigma_Y|$) examination shows that constraint $C_3 < C_3^*$ applies. Calculations of C_3^* for the generic solid in Table 3 imply that the disk can be essentially flat. These observations suggest examining parameters (l_C, d_C) for contact zone A_C, and (β_1, β_2) for crack gap A_G.

For the same generic solid we choose subcritical values $|\sigma^*| = 150$ MPa and $C_3 = 10000$, with disk radius $r_0 = 0.05$ m and clearance ratios

$$\frac{r_S}{r_0} = 4 \ (\psi = 0), \quad \frac{h_S}{r_0} = 1 \ (|\psi| \to \pi/2).$$

In Tables 4 and 5 values of, respectively, l_C/r_0 and d_C/r_0, for $\psi = 0$ are given for various (c, β_1). Corresponding values β_2 follow from (43a) and (44b) as roots of

$$F(\beta_2) - \frac{M_1}{M_2}\left[\frac{2c^2 A_1}{R_1}\left(1 - \frac{1}{c_D^2}\right)\right]^3 F(\beta_1) = 0. \tag{47}$$

$c\downarrow$ $\beta_1\rightarrow$	0.01	0.1	0.2	0.5	0.8
0.05	0.075	0.091	0.107	0.154	0.201
0.1	0.077	0.092	0.108	0.155	0.203
0.2	0.82	0.096	0.114	0.165	0.215
0.5	0.094	0.112	0.115	0.19	0.248

Table 4. l_C/r_0 ($r_S/r_0 = 4$, $\psi = 0$).

$c\downarrow$ $\beta_1\rightarrow$	0.01	0.1	0.2	0.5	0.8
0.05	−0.0034	−0.00052	−0.00077	−0.00194	−0.004
0.1	−0.00035	−0.00053	−0.00077	−0.002	−0.004
0.2	−0.0004	−0.0006	−0.00088	−0.0022	−0.0046
0.5	−0.00053	−0.00081	−0.0012	−0.003	−0.0062

Table 5. d_C/r_0 ($r_S/r_0 = 4$, $\psi = 0$).

β_1	0.01	0.1	0.2	0.5	0.8	1.0
β_2	0.00271	0.0564	0.117	0.275	0.55	0.825
l_C/r_0	0.0756	0.084	0.093	0.118	0.16	0.205

Table 6. Values of $(\beta_1, \beta_2, l_C/r_0)$ for $r_S/r_0 = 4$, $h_S/r_0 = 2$ and $c = 0.2$.

Study of (42c) for $\beta > 0$ shows that $F > 0$, with rapid monotonic growth. Thus numerical determination of roots is not difficult. Based on (47) therefore, a snapshot of how gap-die clearance ratios (β_1, β_2) compare is given in Table 6. Corresponding values of l_C/r_0 ($|\psi| \rightarrow \pi/2$) are also given ($d_C = 0$).

Some observations

This paper considered crack growth in the dynamic steady state caused by the translation of a rigid, smooth die between the surfaces of an initially closed slit. Analysis produced a nonlinear differential equation for the radial distance $r_S(\psi)$ from the die center to the crack edge, where ψ is the angle with respect to the path of die translation. Equation coefficients, however, depend on radial distances $r_\pm(\psi)$ and $r_C^-(\psi)$ to the contours of respectively the crack/die contact zone and the closure zone, i.e., the region in the wake of the die where crack surfaces resume contact. Moreover, the sliding contact aspects of the process lead to algebraic constraints. A framework of equations for the process is thus generated, and was studied to gain insight into the geometry of crack and contact zone behavior. In addition to various formulas:

(a) Calculations in Table 1 show that neglect of sliding friction could affect solution behavior as die/crack growth speed increases.

(b) Calculations in Table 2 show that inclusion of kinetic energy is a perturbation for significant, but clearly subcritical, die/crack growth speeds.

(c) Calculations in Table 3 illustrate the relationship between thickness of a disk-shaped die and maximum allowable die/crack contact zone compression.

(d) Calculations in Tables 4 and 5 show that contact zone width and location of its center with respect to die center are sensitive to die/crack growth speed. They are also sensitive to the relative distances, measured along the die path, from die center to crack edge and crack closure contour. For example, consider in Table 4 the die speed that is 20% of the shear speed in the solid: if the closure contour is 100 times further away from the die center than is the crack edge, contact zone width is 8.2% of the die radius. If it is only 1.25 times further away, the ratio is 24.9%.

(e) Calculations in Tables 4–6 show that the relative distances measured along the die path are greater than relative distances far away from the die path. This observation, together with formulas, show that the gap opened up by die-induced fracture is an infinitely long slit of finite width; its contours bulge out from the die near its path, but are rectilinear and parallel far away.

Die sliding was frictionless, but friction was considered in derivation of the framework. A complete solution for the nonlinear differential equation was not attempted. Thus, The framework was not fully utilized here. However, general conclusions concerning the geometry of crack and contact zones did emerge. These conclusions and the equations themselves could provide the basis for a more general investigation.

Appendix A

$$U_D^{(\pm)} = \frac{-1}{2c_1^2 A}\left[T[\hat{u}_3] + \frac{1}{\mu}(p_1[\hat{\sigma}_{31}] + p_2[\hat{\sigma}_{32}])\right](\pm)\frac{1}{c_1^2}\left(p_1[\hat{u}_1] + p_2[\hat{u}_2] + \frac{[\hat{\sigma}_{33}]}{2\mu}\right), \tag{A.1a}$$

$$V_1^{(\pm)} = \frac{p_1 B}{c_1^2}[\hat{u}_3] + \frac{1}{2\mu B c_1^2}\left[p_1 p_2[\hat{\sigma}_{32}] - (p_2^2 + B^2)[\hat{\sigma}_{31}]\right](\pm)\tfrac{1}{2}\left([\hat{u}_1] - \frac{p_1[\hat{\sigma}_{33}]}{\mu c_1^2}\right) \mp \frac{p_1}{c_1^2}(p_1[\hat{u}_1] + p_2[\hat{u}_2]), \tag{A.1b}$$

$$V_2^{(\pm)} = \frac{p_2 B}{c_1^2}[\hat{u}_3] + \frac{1}{2\mu B c_1^2}\left[p_1 p_2[\hat{\sigma}_{31}] - (p_1^2 + B^2)[\hat{\sigma}_{32}]\right](\pm)\tfrac{1}{2}\left([\hat{u}_2] - \frac{p_2[\hat{\sigma}_{33}]}{\mu c_1^2}\right) \mp \frac{p_2}{c_1^2}(p_1[\hat{u}_1] + p_2[\hat{u}_2]). \tag{A.1c}$$

Equation (8c) holds for (A.1), and it is noted that $p_1\hat{V}_1^{(\pm)} + p_2\hat{V}_2^{(\pm)}$ gives

$$\frac{B}{c_1^2}\left[(p_1^2 + p_2^2)[\hat{u}_3] - \frac{1}{2\mu}(p_1[\hat{\sigma}_{31}] + p_2[\hat{\sigma}_{32}])\right](\pm)\frac{1}{2c_1^2}\left[T(p_1[\hat{u}_1] + p_2[\hat{u}_2]) - B(p_1^2 + p_2^2)\frac{[\hat{\sigma}_{33}]}{\mu}\right]. \tag{A.2}$$

For $x_3 = 0(+)$ use of (A.1) and (A.2) lead to

$$[\hat{u}_1] - \frac{1}{\mu D_R B}(p_2^2 D_M - c_1^2 B^2)\left(2\hat{\sigma}_{31}^{(+)} - [\hat{\sigma}_{31}] - \frac{D_N}{c_1^2 B}p_1[\hat{\sigma}_{33}]\right) + p_1 p_2 \frac{D_M}{\mu D_R B}\left(2\hat{\sigma}_{32}^{(+)} - [\hat{\sigma}_{32}] - \frac{D_N}{c_1^2 B}p_2[\hat{\sigma}_{33}]\right) = 0, \tag{A.3a}$$

$$[\hat{u}_2] - \frac{1}{\mu D_R B}(p_1^2 D_M - c_1^2 B^2)\left(2\hat{\sigma}_{32}^{(+)} - [\hat{\sigma}_{32}] - \frac{D_N}{c_1^2 B}p_2[\hat{\sigma}_{33}]\right) + p_1 p_2 \frac{D_M}{\mu D_R B}\left(2\hat{\sigma}_{31}^{(+)} - [\hat{\sigma}_{31}] - \frac{D_N}{c_1^2 B}p_1[\hat{\sigma}_{33}]\right) = 0, \tag{A.3b}$$

$$[\hat{u}_3] - \frac{c_1^2 A}{\mu D_R}\left[2\hat{\sigma}_{33}^{(+)} - [\hat{\sigma}_{33}] - \frac{D_N}{c_1^2 B}(p_1[\hat{\sigma}_{32}] + p_2[\hat{\sigma}_{32}])\right] = 0. \tag{A.3c}$$

Terms (D_R, D_N, D_M) in (A.3) are given by

$$D_R = T^2 + 4(p_1^2 + p_2^2)AB, \quad D_N = T - 2AB, \quad D_M = 2D_N + c_1^2, \tag{A.4a}$$

$$T = (c^2 - 2)p_1^2 - 2p_2^2. \tag{A.4b}$$

Appendix B

In view of (15)–(17), Equations (A.1) and (7) give for $x_3 > 0(-)$ and $x_3 < 0(+)$,

$$(\hat{u}_1)_D + \frac{p_1}{2c_1^2 A}(T[\hat{u}_3] + p_1[\hat{\sigma}_{31}]/\mu)\exp(-A|x_3|) = 0, \tag{B.1a}$$

$$(\hat{u}_2)_D + \frac{p_2}{2c_1^2 A}(T[\hat{u}_3] + p_1[\hat{\sigma}_{31}]/\mu)\exp(-A|x_3|) = 0, \tag{B.1b}$$

$$(\hat{u}_3)_D(\mp)\frac{1}{2c_1^2}(T[\hat{u}_3] + p_1[\hat{\sigma}_{31}]/\mu)\exp(-A|x_3|) = 0. \tag{B.1c}$$

$$(\hat{u}_1)_S - \frac{1}{c_1^2}\left[p_1 B[\hat{u}_3] - \frac{1}{2B}(p_2^2 + B^2)[\hat{\sigma}_{31}]/\mu\right]\exp(-B|x_3|) = 0, \tag{B.2a}$$

$$(\hat{u}_2)_S - \frac{1}{c_1^2}\left(p_2 B[\hat{u}_3] - \frac{p_1 p_2}{2B}[\hat{\sigma}_{31}]/\mu\right)\exp(-B|x_3|) = 0, \tag{B.2b}$$

$$(\hat{u}_3)_S(\mp)\frac{1}{c_1^2}\left[(p_1^2 + p_2^2)[\hat{u}_3] - \frac{p_1}{2}[\hat{\sigma}_{31}]\right]\exp(-B|x_3|) = 0. \tag{B.2c}$$

Appendix C

$$\frac{\partial u_1^{(+)}}{\partial x} \approx -\frac{A\cos\psi}{\pi^2 S}\int_C \frac{\partial U}{\partial t}\sqrt{\frac{r_S - t}{t + r_C^-}}\frac{(t + r_-)^\Omega\,\mathrm{d}t}{(r_+ - t)^{1+\Omega}}\mathrm{Re}\,Q_+(i2P_{12}, t), \tag{C.1a}$$

$$\frac{\partial u_2^{(+)}}{\partial x} \approx -\frac{A\sin\psi}{\pi^2 S}\int_C \frac{\partial U}{\partial t}\sqrt{\frac{r_S - t}{t + r_C^-}}\frac{(t + r_-)^\Omega\,\mathrm{d}t}{(r_+ - t)^{1+\Omega}}\mathrm{Re}\,Q_+(i2P_{12}, t), \tag{C.1b}$$

$$\frac{\partial u_3^{(+)}}{\partial x} \approx \frac{A}{\pi^2 S}\int_C \frac{\partial U}{\partial t}\sqrt{\frac{r_S - t}{t + r_C^-}}\frac{(t + r_-)^\Omega\,\mathrm{d}t}{(r_+ - t)^{1+\Omega}}\mathrm{Im}\,Q_+(i2P_3, t). \tag{C.1c}$$

$$Q_+(f, t) = \int_+ \sqrt{\frac{\tau + r_C^-}{r_S - \tau}}\frac{f(\tau - r_+)^{1+\Omega}}{(\tau + r_-)^\Omega(t - \tau)}\,\mathrm{d}\tau. \tag{C.2}$$

In (C.2) integration subscript + signifies range $r_+ < \tau < r_S$, and in (C.1)

$$P_{12} = \frac{T}{2A(z_A - \tau)} + \frac{B}{z_B - \tau}, \qquad P_3 = \frac{T}{2(z_A - \tau)} + \frac{1}{z_B - \tau}, \tag{C.3a}$$

$$z_A = x + iA|x_3|, \qquad z_B = x + iB|x_3|. \tag{C.3b}$$

In light of (24a), (24c), (26c) and (29) results for $r \to 0$, $|\phi| < \pi$, $|\psi| < \pi/2$ are

$$\partial_1 u_1 \to -\frac{\cos\psi}{\sqrt{2r}} \frac{2A}{\pi S} G_C D_S \left(\frac{T}{2A} \frac{A_+}{A_\Phi} + B \frac{B_+}{B_\Phi} \right) \operatorname{sgn}(\phi), \tag{C.4a}$$

$$\partial_1 u_2 \to -\frac{\sin\psi}{\sqrt{2r}} \frac{2A}{\pi S} G_C D_S \left(\frac{T}{2A} \frac{A_+}{A_\Phi} + B \frac{B_+}{B_\Phi} \right) \operatorname{sgn}(\phi), \tag{C.4b}$$

$$\partial_1 u_3 \to -\frac{1}{\sqrt{2r}} \frac{2A}{\pi S} G_C D_S \left(\frac{T}{2} \frac{A_-}{A_\Phi} + \frac{B_-}{B_\Phi} \right). \tag{C.4c}$$

$$A_\Phi = \sqrt{1 - \bar{c}^2/c_D^2 \sin^2\phi}, \qquad A_\pm = \sqrt{A_\Phi \pm \cos\phi}, \tag{C.5a}$$

$$B_\Phi = \sqrt{1 - \bar{c}^2 \sin^2\phi}, \qquad B_\pm = \sqrt{B_\Phi \pm \cos\phi}. \tag{C.5b}$$

Appendix D

$$D_0 = 1 - 1/r_S(r_+ + \Omega l_C) + \Omega(1+\Omega)(l_C/(2r_S))^2, \tag{D.1a}$$

$$D_1 = 1/(2r_S)(r_S/r_C^- - 1)[1 - 2/r_S(r_+ + \Omega l_C)], \tag{D.1b}$$

$$D_2 = 1/(2r_S^2)\left[\tfrac{3}{4}(r_S/r_C^- - 1)^2 + r_S/r_C^-\right]. \tag{D.1c}$$

$$I_0 = r_+ + \Omega l_C, \tag{D.2a}$$

$$I_1 = r_+^2 + \Omega r_+ l_C - \Omega/2(1-\Omega) l_C^2, \tag{D.2b}$$

$$I_2 = r_+^3 + 3\Omega r_+^2 l_C - 3\Omega/2(1-\Omega) r_+ l_C^2 + \Omega/6(1-\Omega)(2-\Omega) l_C^3. \tag{D.2c}$$

References

[Brock 2004] L. M. Brock, "Dynamic fracture of transversely isotropic coupled thermoelastic solids: wedging by a cylinder with friction", *J. Therm. Stresses* **27**:11 (2004), 1053–1073.

[Brock 2012] L. M. Brock, "Two cases of rapid contact on an elastic half-space: the sliding ellipsoid die, rolling sphere", *J. Mech. Mater. Struct.* **7**:5 (2012), 469–483.

[Brock 2015a] L. M. Brock, "Contours for planar cracks growing in three dimensions", *J. Mech. Mater. Struct.* **10**:1 (2015), 63–77.

[Brock 2015b] L. M. Brock, "Contours for planar cracks growing in three dimensions: influence of kinetic energy", *J. Appl. Mech.* (*ASME*) **82**:11 (09/28 2015), 111011.

[Brock and Georgiadis 2000] L. M. Brock and H. G. Georgiadis, "Sliding contact with friction of a thermoelastic solid at subsonic, transonic, and supersonic speeds", *J. Therm. Stresses* **23**:7 (2000), 629–656.

[deBoer et al. 1988] F. R. deBoer, R. Boom, W. C. M. Mattens, A. R. Miedema, and A. K. Niessen, *Cohesion in metals*, North-Holland, Amsterdam, 1988.

[Freund 1972] L. B. Freund, "Energy flux into the tip of an extending crack in an elastic solid", *J. Elasticity* **2**:4 (1972), 341–349.

[Freund 1990] L. B. Freund, *Dynamic fracture mechanics*, Cambridge Monographs on Mechanics and Applied Mathematics, Cambridge University Press, Cambridge, England, 1990.

[Gdoutos 2005] E. E. Gdoutos, *Dynamic fracture*, pp. 239–264, Solid mechanics and its applications **123**, Springer, New York, 2005.

[Malvern 1969] L. S. Malvern, *Introduction to the mechanics of continuous media*, Prentice-Hall, Englewood Cliffs, New Jersey, 1969.

[Mastrojannis et al. 1980] E. N. Mastrojannis, L. M. Keer, and T. Mura, "Growth of planar cracks induced by hydraulic fracturing", *Int. J. Numer. Meth. Eng.* **15**:1 (1980), 41–54.

[Skriver and Rosengaard 1992] H. L. Skriver and N. M. Rosengaard, "Surface energy and work function of elemental metals", *Phys. Rev. B* **46** (Sep 1992), 7157–7168.

[Sneddon 1972] I. N. Sneddon, *The use of integral transforms*, McGraw-Hill, New York, 1972.

Received 25 Feb 2016. Revised 4 Apr 2016. Accepted 6 Aug 2016.

LOUIS M. BROCK: louis.brock@uky.edu
Department of Mechanical Engineering, College of Engineering, University of Kentucky, Lexington, KY 40506-0038, United States

JOURNAL OF MECHANICS OF MATERIALS AND STRUCTURES
Vol. 12, No. 2, 2017
dx.doi.org/10.2140/jomms.2017.12.179

MAXWELL'S EQUIVALENT INHOMOGENEITY AND REMARKABLE PROPERTIES OF HARMONIC PROBLEMS INVOLVING SYMMETRIC DOMAINS

SOFIA G. MOGILEVSKAYA AND DMITRY NIKOLSKIY

This paper revisits the Maxwell concept of equivalent inhomogeneity in the context of two-dimensional harmonic problems involving composite or porous materials of periodic structure. As previously done for elasticity problems, here the scheme is modified to accommodate for the shape of the equivalent inhomogeneity and for the interactions between the constituents of the cluster. New numerical results for periodic materials with hexagonal arrangements of fibers (holes) demonstrate that, with these modifications, the scheme allows for accurate estimates of the effective material properties. It is also shown that, as for elasticity problems, some harmonic symmetric inhomogeneities possess remarkable properties. Under the action of uniform far-fields, the averages of the fields within these inhomogeneities preserve the structure of the applied far-fields.

1. Introduction

This paper presents further studies of the Maxwell [1892] homogenization scheme that is based on the concept of an equivalent inhomogeneity. The concept suggests that a cluster that represents the material in question affects the fields at large distances away from it in the same manner as an equivalent inhomogeneity whose properties are equal to the effective ones.

The idea has a long history (see, e.g., [Milton 2002; Torquato 2002], and the references therein) and has been reinvented in a few later publications, e.g., [Kuster and Toksöz 1974; Hasselman and Johnson 1987; Lu and Song 1996; Lu 1998; Shen and Yi 2000; 2001; 2004]. In recent years, the concept has attracted even more attention, (e.g., [McCartney and Kelly 2008; McCartney 2010; Koroteeva et al. 2010; Mogilevskaya et al. 2010; 2012a; 2012b; 2013; Weng 2010; Pyatigorets and Mogilevskaya 2011; Levin et al. 2012; Mogilevskaya and Crouch 2013; Kushch 2013; Kushch et al. 2014; Kushch and Knyazeva 2016; Kushch and Sevostianov 2016]) and, in some of these publications, was generalized to include information on the geometrical arrangement of the constituents of the cluster and their interactions.

The original Maxwell scheme and its later modifications in application to the material with overall isotropy adopted either a spherical (three-dimensions) or a circular (two-dimensions) shape of the equivalent inhomogeneity. However, the papers [Jasiuk et al. 1992; 1994; Sevostianov and Kachanov 2011; Kushch and Sevostianov 2015] (see also the references therein) have demonstrated that the shape has an influence on the far-field asymptotic behavior. Some of these publications, although not directly related to Maxwell's concept, are relevant because the analysis of the far-fields is a cornerstone of the original Maxwell concept.

Keywords: Maxwell equivalent inhomogeneity, harmonic problems, composite and porous materials, effective properties.

In the context of Maxwell's scheme, the issue of shape was investigated in [Sevostianov and Giraud 2013; Sevostianov 2014; Kushch et al. 2014; Kushch and Sevostianov 2016; Kushch and Knyazeva 2016]. These authors studied more general cases that involved materials with overall anisotropic behavior and suggested using a more general shape of the equivalent inhomogeneity (elliptical for two-dimensional and ellipsoidal for three-dimensional problems). Their major arguments were based on the availability of closed form analytical solutions for the fields due to these inhomogeneities, see [Eshelby 1957; 1959; 1961]. In [Mogilevskaya and Nikolskiy 2015], it was demonstrated numerically that, for two-dimensional *elastic* materials with hexagonal symmetry, the estimates for the effective bulk and shear moduli based on a hexagonal shape of the equivalent inhomogeneity are more accurate than those based on circular shape. In addition, while circular-based estimates for some materials diverge with the size of the cluster, their hexagonal counterparts converge. Also in that paper, it was numerically discovered that two-dimensional regular polygonal and other symmetric inhomogeneities possess some remarkable properties. Under the action of uniform far-fields, the averages of the fields within these inhomogeneities have the same structure as that of the applied far-fields. In [Mogilevskaya and Stolarski 2015], these properties have been rigorously proved for a wider class of two- and three-dimensional elastic problems, which included anisotropic and nonuniform materials subjected to either far-field loads or constant transformational strains within the inhomogeneity.

In this paper, we use the approach in [Mogilevskaya and Nikolskiy 2015] to study the issue of the shape of Maxwell's inhomogeneity in the context of problems governed by the Laplace equation (harmonic problems). New developments presented here include new numerical results on the effective properties (e.g., conductivities) of two-dimensional materials with hexagonal symmetry, including the convergence studies. As previously done for elasticity problems in the above cited paper, some remarkable properties of symmetric inhomogeneities are numerically discovered here for harmonic problems.

The paper is structured as follows. In Section 2, the classical concept of Maxwell's equivalent inhomogeneity for harmonic problems is described and the generalized Maxwell approach is briefly reviewed. In Section 3, we consider the problem of finding the property of an arbitrarily shaped inhomogeneity whose asymptotic far-fields' expansions contain the same leading terms as those for the circular inhomogeneity of the same area. In Section 4, we analyze the obtained interrelations between the properties of the arbitrarily shaped and circular inhomogeneities. This analysis leads to the discovery of some remarkable properties of regular polygonal and other symmetric inhomogeneities. In Section 5, using the results on the effective properties obtained with the use of circular equivalent inhomogeneity (see [Mogilevskaya et al. 2012b]), we recalculate the effective properties for the periodic materials using a hexagonal shape for that inhomogeneity. We demonstrate that these new estimates converge faster with the size of the cluster than the corresponding circular inhomogeneity-based estimates. The discussion of the obtained results and the direction for future work are presented in Section 6.

2. Maxwell's scheme and a review of the generalized Maxwell approach that accounts for interaction

The original Maxwell scheme is based on the idea that a cluster that represents the material in question (Figure 1, left, for the two-dimensional case) affects the fields at large distances away from it in the same manner as an equivalent circle (sphere) (Figure 1, right) whose property (e.g., thermal or electric

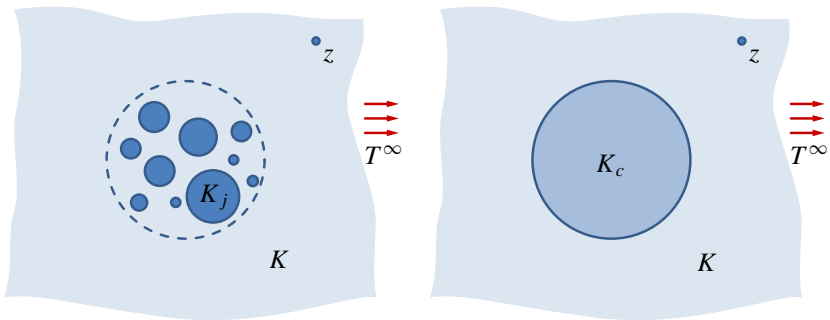

Figure 1. Cluster of circular inhomogeneities (left) and equivalent inhomogeneity (right).

conductivity) is equal to the effective one. The radius R of the equivalent circle/sphere is chosen such that the ratio of the total area (volume) occupied by the constituents of the cluster to that of the equivalent circle (sphere) reflects the volume fraction of the material.

Below we review the basics of the scheme and its generalization in the context of the steady-state heat conduction problem. However, the scheme can be easily reformulated in terms of any harmonic problem (e.g., antiplane elasticity in two dimensions). We assume that the cluster consists of N nonoverlapping fibers/particles that are perfectly bonded to the material matrix. In the original Maxwell's scheme the fibers/particles are of circular/spherical shapes. In that scheme, the geometrical arrangement of the fibers/particles is neglected (from large distances away, they are perceived as to be located at the same point), and the interactions between them are not accounted for (the contribution of every fiber/particle to the far-fields is evaluated under the assumption that this fiber/particle is the only one in the matrix). Maxwell [1892], who considered the three-dimensional case, assumed that all particles had the same conductivities k_p that are different from the conductivity k of the matrix. The latter restriction is easy to lift as it was done in [McCartney and Kelly 2008; Mogilevskaya et al. 2012a] for the three-dimensional case and in [Mogilevskaya et al. 2012b] for the two-dimensional case (the latter paper considered the scheme in the context of antiplane problem).

With the above assumptions, Maxwell's scheme yields the following result for the effective conductivity k_{ef} of the material (both for two- and three-dimensional problems):

$$\frac{k_{\text{ef}}}{k} = \frac{1-(d-1)B^0}{1+B^0}, \qquad B^0 = \sum_{j=1}^{N} c_j \left(1 - \frac{k_j}{k}\right) \frac{1}{(d-1)+k_j/k}, \tag{1}$$

in which k_j is the conductivity of the j-th circular fiber (spherical particle) of radius a_j, the variable d is the dimension of the problem ($d = 2$ in two-dimensions, $d = 3$ in three-dimensions), and c_j is the so-called volume fraction of j-th particle/fiber ($j = 1, \ldots, N$) that is defined as

$$c_j = \left(\frac{a_j}{R}\right)^d. \tag{2}$$

The papers [Mogilevskaya et al. 2012a; 2012b; 2013; Kushch et al. 2013; 2014; Kushch and Knyazeva 2016; Kushch and Sevostianov 2016] generalized the Maxwell scheme by precisely evaluating the far-fields due to the cluster using semianalytical methods. These methods explicitly account for the

geometrical arrangements of the particles/fibers in the cluster and their interactions. The effective constants were obtained by comparing the dipole coefficients in the multipole expansions of far-fields with the dipole coefficients for the equivalent inhomogeneities. The effective conductivity (that was assumed to be the same as that of the equivalent inhomogeneity) was expressed by equations similar to that of (1)–(2) but with different parameters, B^0 (see e.g., [Mogilevskaya et al. 2012a, Equations (16)–(18)] with $B^0 = A^*_{10}$ for spherical particles). In the generalized approach in [Koroteeva et al. 2010; Mogilevskaya et al. 2012a; 2012b], the shape of the equivalent inhomogeneity was assumed to be the same (circular or spherical) as that in the original Maxwell's approach while [Kushch et al. 2014; Kushch and Knyazeva 2016; Kushch and Sevostianov 2016] suggested the use of an elliptical (ellipsoidal) shape when the overall behavior of the materials is anisotropic.

We now consider the two-dimensional case, assuming that shape of the equivalent inhomogeneity may be arbitrary, and formulate the following auxiliary problem: determine the property of a noncircular inhomogeneity such that the asymptotic expansions of the far-fields induced by it have the same leading terms as that induced by the circular inhomogeneity.

3. The expressions for the far-fields induced by the inhomogeneity

We assume that the circular inhomogeneity of radius R and conductivity k_c has its center at the origin of the Cartesian coordinate system $x_1 O x_2$ (Figure 2, left). The counterpart problem of the inhomogeneity D of arbitrary shape and conductivity k_I is shown on Figure 2, right, where L is the boundary of that inhomogeneity. For both problems, it is assumed that the temperature gradient $T^\infty = \alpha x_1$ is applied at infinity. Both problems are governed by the Laplace equation. The solution for the first problem is well-known (see, e.g., [Honein et al. 1992]). The temperature at the point $z = x_1 + i x_2$ located inside the matrix can be written in the form

$$T(z) = T^\infty(z) + \alpha \frac{1 - k_c/k}{1 + k_c/k} \operatorname{Re} \frac{R^2}{\bar{z}}, \tag{3}$$

in which $\bar{z} = x_1 - i x_2$.

The solution for the second problem is also available in [Linkov 2002; Dobroskok and Linkov 2009] and [Dong and Lo 2013]. The temperature at the same point z is

$$T(z) = T^\infty(z) + (1 - k_I/k) \operatorname{Re} \frac{1}{2\pi i} \int_L \frac{T(\tau)\, \mathrm{d}\tau}{\tau - z}. \tag{4}$$

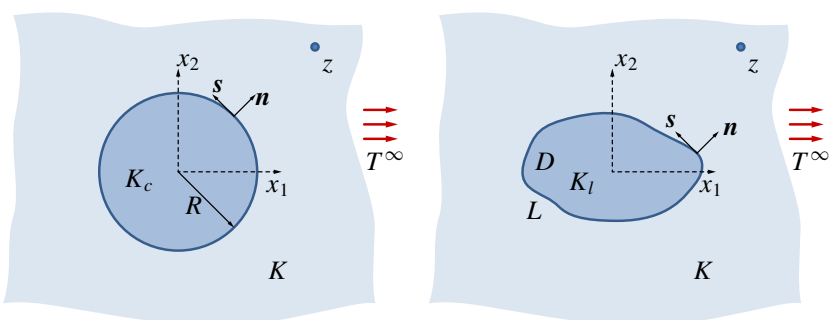

Figure 2. Circular inhomogeneity (left) and arbitrarily shaped inhomogeneity (right)

Assuming that the point z is located far away from the inhomogeneity, one can obtain the following asymptotic expansion for the complementary temperature $T^{\mathrm{com}}(z) = T(z) - T^{\infty}(z)$:

$$T^{\mathrm{com}}(z) = -(1 - k_I/k)\,\mathrm{Im}\,\frac{1}{2\pi}\left\{\frac{1}{z}\int_L T(\tau)\,\mathrm{d}\tau + \frac{1}{z^2}\int_L T(\tau)\tau\,\mathrm{d}\tau + O\left(\frac{1}{z^3}\right)\right\}. \tag{5}$$

The comparison of (3) with the leading terms of (5) yields the following set of equations:

$$\mathrm{Re}\int_L T(\tau)\,\mathrm{d}\tau = 0, \tag{6}$$

$$\mathrm{Im}\int_L T(\tau)\,\mathrm{d}\tau = -2\pi R^2 \frac{\alpha}{1 - k_I/k}\frac{1 - k_c/k}{1 + k_c/k}. \tag{7}$$

It can be shown that

$$\mathrm{Re}\int_L T(\tau)\,\mathrm{d}\tau = -\int_D \frac{\partial T(\tau)}{\partial x_2}\,\mathrm{d}D, \tag{8}$$

$$\mathrm{Im}\int_L T(\tau)\,\mathrm{d}\tau = \int_D \frac{\partial T(\tau)}{\partial x_1}\,\mathrm{d}D, \tag{9}$$

which indicates that these integrals are proportional to the corresponding average temperature gradients within the inhomogeneity.

4. Analysis of the equations of Section 3

It follows from (6) and (8) that

$$\int_D \frac{\partial T(\tau)}{\partial x_2}\,\mathrm{d}D = 0, \tag{10}$$

which indicates that the average temperature gradient within the inhomogeneity has only the x_1 component, as is the case for the applied temperature field. Certainly, it could only be valid for the problems with particular types of symmetry. Using virtually the same arguments as those presented in [Mogilevskaya and Stolarski 2015], it could be proved that (10) is valid for the inhomogeneities whose shapes possess certain types of rotational symmetry. For such problems, the interrelation between the property of the inhomogeneity associated with the problem and that of the circular inhomogeneity can be obtained from (7) and (9) as follows:

$$\frac{k_I}{k} = 1 - 2\frac{1 - k_c/k}{1 + k_c/k}\frac{\alpha}{\Xi}, \tag{11}$$

in which

$$\Xi = \frac{1}{\pi R^2}\int_D \frac{\partial T(z)}{\partial x_1}\,\mathrm{d}D. \tag{12}$$

5. Results

5.1. ***Interpretation of the equations of Section 4.*** We now assume that the area of the inhomogeneity is the same as that of the circle, πR^2. It can be seen that the expression in the right-hand side of (12) is the

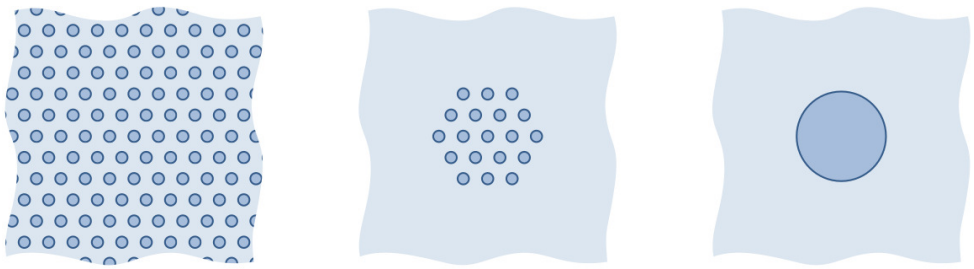

Figure 3. Infinite hexagonal array of inhomogeneities (left), finite cluster of inhomogeneities and equivalent hexagonal inhomogeneity in homogeneous matrix material (middle), finite cluster of inhomogeneities and equivalent circular inhomogeneity (right).

area average of the temperature gradient in the corresponding direction. Therefore, the conductivity of the inhomogeneity D is expressed by (11) via the corresponding property of the circular inhomogeneity of the same area and via the average given by (12). However, this average also depends on the conductivity of the inhomogeneity D, which has yet to be found.

To resolve this issue, we propose the simple iteration procedure in which the boundary value problem of the inhomogeneity of the same geometry as D but with the properties $(k_I)_0$ taken to be the same as for the corresponding circular inhomogeneity, $(k_I)_0 = k_c$, and is solved first by means of a boundary element code. The conductivities k_c were evaluated in [Mogilevskaya et al. 2012b]. The new conductivity $(k_I)_1$ obtained from (12) is then used in the next iteration. The process is terminated when the difference between the values obtained in last two iterations becomes less than the prescribed accuracy level.

Below, the proposed approach is used to evaluate the effective conductivities of a two-phase composite material with a hexagonal arrangement of fibers (Figure 3, left). The unit cell of this material is a hexagon that possesses desirable symmetry with respect to the coordinate axes. The problem of hexagonal inhomogeneity was solved by using an in-house boundary element code that employs quadratic approximations for the unknown temperature on each straight boundary element. Using this code, we demonstrated numerically that the conditions of (10) are satisfied up to 11 significant digits. These conditions, as explained above, imply that the average directional temperature gradients have the same structure as those of the applied far-field temperature field. These "strange" properties of symmetric inhomogeneities can be proved theoretically for more general classes of two- and three-dimensional anisotropic and nonuniform materials using virtually the same arguments as those used in [Mogilevskaya and Stolarski 2015] for elastic problems.

5.2. ***Circular fibers.*** The cluster of $N = N(p) = 1 + 3p(p+1)$, where $p \geq 1$, circular fibers (holes) of radius r_0 that forms a hexagon D is taken from an infinite double-periodic array of fibers (holes) (Figure 3, left) and placed in an infinite matrix material (Figure 3, middle). The area $|D|$ of the hexagon is

$$|D| = \frac{3\sqrt{3}d^2}{2}p^2, \tag{13}$$

in which d is the distance between the centers of the inhomogeneities.

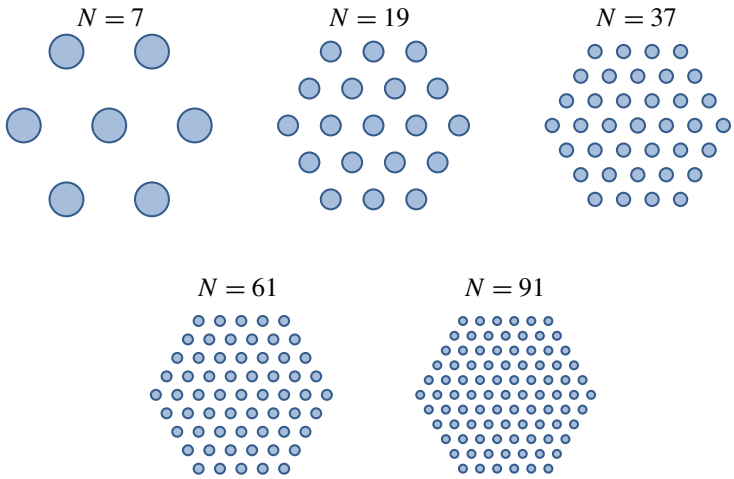

Figure 4. Clusters of N inhomogeneities.

The volume fraction c of the fibers (holes) in the above mentioned double-periodic array is defined as

$$c = \frac{2\pi r_0^2}{\sqrt{3}d^2}. \tag{14}$$

The equivalent circular inhomogeneity (Figure 3, right), considered in [Mogilevskaya et al. 2012b], has the same area as the hexagon. The radius of that inhomogeneity can be found from the equation

$$\pi R^2 = \frac{3\sqrt{3}d^2}{2} p^2. \tag{15}$$

The examples of five clusters of the material with $N = 7$, 19, 37, 61, and 91 fibers are shown in Figure 4. Assume that k_f is the conductivity of the fibers. Consider the cases:

(i) of holes, where $k_f/k = 0$, and

(ii) of high contrast in fibers/matrix conductivities, where $k_f/k = 135$.

The accurate estimates of the normalized effective conductivity (k_{per}/k) were provided to us by Godin [2013] (for both cases) and Kushch [2013](for the second case). These authors solved the double periodic problem using two different methods. For high contrast composites, the results obtained by both methods were identical up to the requested five significant digits. The estimates k_c/k are obtained by the method described in [Mogilevskaya et al. 2012b]. Note, these estimates take the full account for the interactions among all fibers of the cluster and its geometry.

The conductivity of the hexagonal inhomogeneity, k_h/k, is calculated from the iteration procedure described in the beginning of this section. The parameter defining the accuracy level was set up as 10^{-5}. The values of the moduli for each iteration were obtained from (11) in which the conductivity needed to evaluate Ξ was taken from the previous iteration. The number of iterations depended on the volume fraction and varied from 1 (for low volume fractions) to 64 (for high volume fractions). The boundary element solution required to evaluate Ξ employed 32 elements on each side of the hexagon.

c	k_c/k					Periodic (k_{per}/k), [Godin 2013]
	$N=7$	$N=19$	$N=37$	$N=61$	$N=91$	
0.1	0.81814	0.81814	0.81814	0.81814	0.81814	0.81818
0.2	0.66635	0.66635	0.66637	0.66638	0.66639	0.66667
0.3	0.53745	0.53748	0.53754	0.53758	0.53761	0.53844
0.4	0.42621	0.42635	0.42650	0.42660	0.42667	0.42845
0.5	0.32868	0.32901	0.32932	0.32953	0.32967	0.33281
0.6	0.24167	0.24224	0.24277	0.24313	0.24337	0.24834
0.7	0.16227	0.16308	0.16387	0.16441	0.16478	0.17208
0.8	0.08705	0.08791	0.08896	0.08970	0.09021	0.10042
0.85	0.04875	0.04940	0.05051	0.05132	0.05189	0.06383

Table 1. Normalized effective conductivity for hexagonal arrays, $k_f/k = 0$. Circular equivalent inhomogeneity.

c	k_h/k					Periodic (k_{per}/k), [Godin 2013]
	$N=7$	$N=19$	$N=37$	$N=61$	$N=91$	
0.1	0.81818	0.81818	0.81818	0.81818	0.81818	0.81818
0.2	0.66661	0.66661	0.66663	0.66664	0.66665	0.66667
0.3	0.53819	0.53822	0.53828	0.53832	0.53835	0.53844
0.4	0.42773	0.42787	0.42802	0.42812	0.42818	0.42845
0.5	0.33129	0.33162	0.33192	0.33213	0.33227	0.33281
0.6	0.24569	0.24625	0.24677	0.24712	0.24736	0.24834
0.7	0.16806	0.16885	0.16962	0.17014	0.17051	0.17208
0.8	0.09506	0.09588	0.09689	0.09761	0.09812	0.10042
0.85	0.05813	0.05876	0.05983	0.06060	0.06116	0.06383

Table 2. Normalized effective conductivity for hexagonal arrays, $k_f/k = 0$. Hexagonal equivalent inhomogeneity.

The results for k_h/k are tabulated in Tables 2 and 4 (the corresponding results for k_c/k are given in Tables 1 and 3). Graphical representation of the results is presented in Figure 5. It could be seen that, while both circular- and hexagon-based estimates seem to converge with the size of the cluster, the latter estimates are more accurate. This is true for both cases of contrast in fiber and matrix conductivities. To better illustrate this fact, the relative errors $\delta = |k_I - k_{\text{per}}|/k_{\text{per}}$ are plotted in Figure 6 for cases (i) and (ii) with volume fractions $c = 0.6$ and 0.85. The results indicate that both estimates converge linearly, i.e.,

$$\lim_{p\to\infty} \frac{|k_I^{(p+1)} - k_{\text{per}}|}{|k_I^{(p)} - k_{\text{per}}|} = \lambda > 0, \tag{16}$$

c	k_c/k					Periodic (k_{per}/k), [Godin 2013; Kushch 2013]
	$N=7$	$N=19$	$N=37$	$N=61$	$N=91$	
0.1	1.2187	1.2187	1.2187	1.2187	1.2187	1.2186
0.2	1.4915	1.4915	1.4915	1.4915	1.4914	1.4908
0.3	1.8426	1.8424	1.8423	1.8421	1.8420	1.8393
0.4	2.3131	2.3124	2.3116	2.3111	2.3107	2.3016
0.5	2.9814	2.9786	2.9760	2.9742	2.9730	2.9464
0.6	4.0179	4.0090	4.0008	3.9954	3.9917	3.9165
0.7	5.8849	5.8582	5.8321	5.8145	5.8026	5.5744
0.8	10.5035	10.4135	10.3056	10.2313	10.1800	9.2521
0.85	17.4471	17.2641	16.9526	16.9526	16.5806	13.9231

Table 3. Normalized effective conductivity for hexagonal arrays, $k_f/k = 135$. Circular equivalent inhomogeneity.

c	k_h/k					Periodic (k_{per}/k), [Godin 2013; Kushch 2013]
	$N=7$	$N=19$	$N=37$	$N=61$	$N=91$	
0.1	1.2186	1.2186	1.2186	1.2186	1.2186	1.2186
0.2	1.4910	1.4910	1.4910	1.4910	1.4909	1.4908
0.3	1.8402	1.8400	1.8399	1.8397	1.8396	1.8393
0.4	2.3053	2.3046	2.3038	2.3033	2.3029	2.3016
0.5	2.9592	2.9564	2.9539	2.9521	2.9510	2.9464
0.6	3.9561	3.9475	3.9397	3.9346	3.9311	3.9165
0.7	5.6970	5.6724	5.6486	5.6325	5.6216	5.5744
0.8	9.7125	9.6377	9.5483	9.4865	9.4438	9.2521
0.85	15.0606	14.9286	14.7037	14.5444	14.4333	13.9231

Table 4. Normalized effective conductivity for hexagonal arrays, $k_f/k = 135$. Hexagonal equivalent inhomogeneity.

where $k_I^{(p)}$ is the conductivity of the equivalent inhomogeneity representing a cluster containing $N = N(p)$ inhomogeneities. The convergence analysis of the tabulated results suggests that the hexagon-based estimates converge with $\lambda \approx 0.8$, which is faster than the circle-based estimates with $\lambda \approx 0.95$.

6. Conclusions

In this paper, we studied the shape of Maxwell's equivalent inhomogeneity for two-dimensional harmonic problems. For problems with hexagonal symmetry, we report new tabulated and graphically illustrated numerical results that are obtained with the use of the modified Maxwell's scheme that accounts for the interactions within the cluster and employs the hexagonal equivalent inhomogeneity. By performing convergence studies, we demonstrated that this scheme provides more accurate estimates for the effective

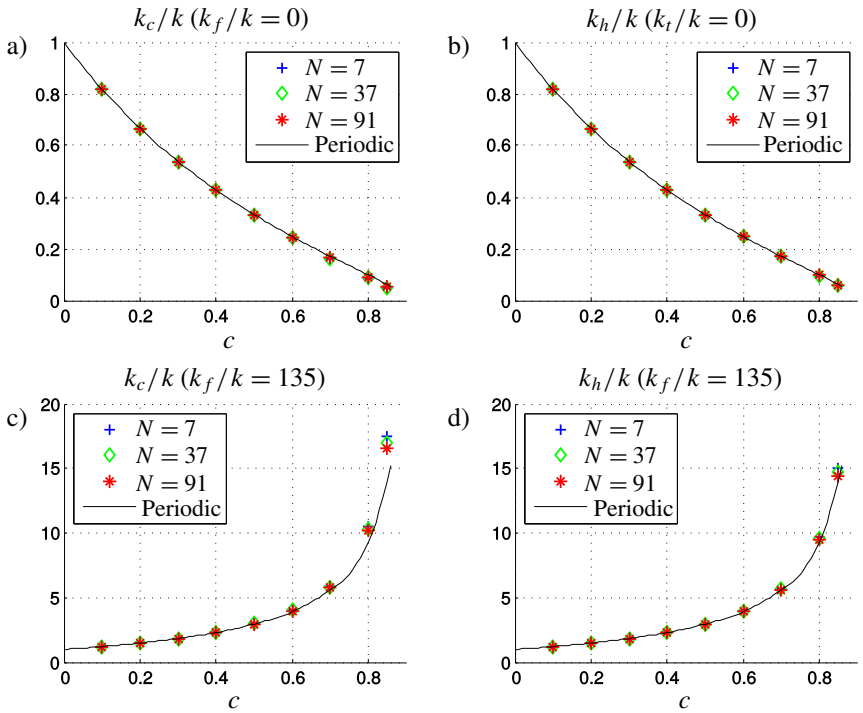

Figure 5. Normalized effective conductivity for hexagonal arrays: a) circular equivalent inhomogeneity, $k_f/k = 0$; b) hexagonal equivalent inhomogeneity, $k_f/k = 0$; c) circular equivalent inhomogeneity, $k_f/k = 135$; d) hexagonal equivalent inhomogeneity, $k_f/k = 135$.

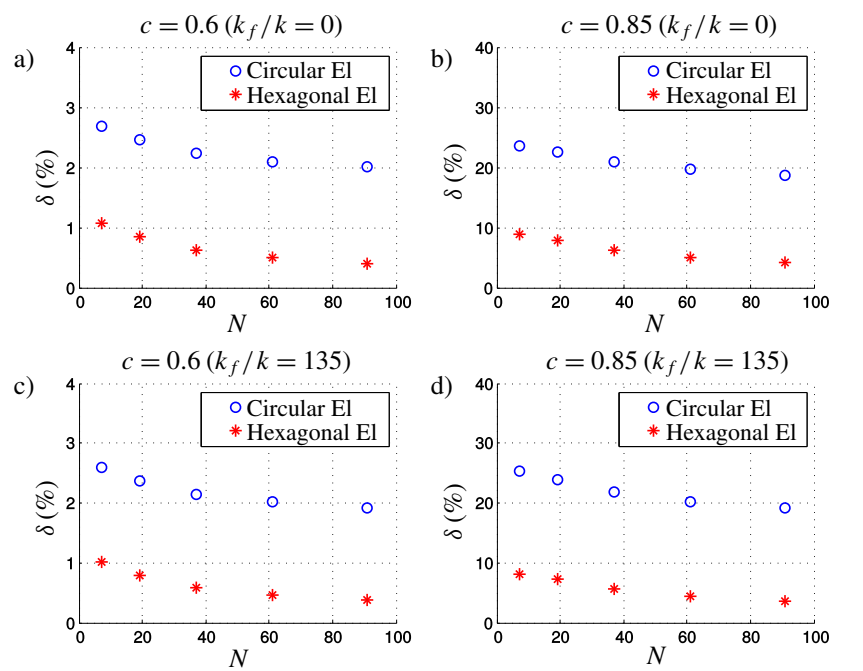

Figure 6. Relative error of normalized effective conductivity $\delta = |k_c - k_{\text{per}}|/k_{\text{per}}$ for circular equivalent inhomogeneity, $\delta = |k_h - k_{\text{per}}|/k_{\text{per}}$ for hexagonal equivalent inhomogeneity.

properties of the materials than that employing circular shape. In addition, we demonstrated numerically that hexagonal inhomogeneities possess remarkable properties. Under the action of a uniform temperature gradient, the averages of the temperature within the inhomogeneity preserves the structure of the applied far-fields. These "strange" properties of symmetric inhomogeneities can be proved theoretically for more general classes of two- and three- dimensional anisotropic and nonuniform harmonic materials using virtually the same arguments as those used in [Mogilevskaya and Stolarski 2015] for elastic problems.

Acknowledgments

The first author gratefully acknowledges the support from the Theodore W. Bennett Chair, University of Minnesota. Special thanks to Volodymyr I. Kushch and Yuri A. Godin for providing benchmark results for hexagonal arrays.

References

[Dobroskok and Linkov 2009] A. A. Dobroskok and A. M. Linkov, "Complex variable equations and the numerical solution of harmonic problems for piecewise-homogeneous media", *J. Appl. Math. Mech.* **73**:3 (2009), 313–325.

[Dong and Lo 2013] C. Y. Dong and S. H. Lo, "An integral equation formulation of anti-plane inhomogeneities", *Eng. Anal. Bound. Elem.* **37**:11 (2013), 1416–1425.

[Eshelby 1957] J. D. Eshelby, "The determination of the elastic field of an ellipsoidal inclusion, and related problems", *Proc. R. Soc. A.* **241** (1957), 376–396.

[Eshelby 1959] J. D. Eshelby, "The elastic field outside an ellipsoidal inclusion", *Proc. R. Soc. A* **252** (1959), 561–569.

[Eshelby 1961] J. D. Eshelby, "Elastic inclusions and inhomogeneities", pp. 87–140 in *Progress in solid mechanics*, vol. 2, edited by I. N. Sneddon and R. Hill, North-Holland, Amsterdam, 1961.

[Godin 2013] Y. A. Godin, "Effective complex permittivity tensor of a periodic array of cylinders", *J. Math. Phys.* **54**:5 (2013), 053505.

[Hasselman and Johnson 1987] D. P. H. Hasselman and L. F. Johnson, "Effective thermal conductivity of composites with interfacial thermal barrier resistance", *J. Compos. Mater.* **21**:6 (1987), 508–515.

[Honein et al. 1992] E. Honein, T. Honein, and G. Herrmann, "On two circular inclusions in harmonic problems", *Quart. Appl. Math.* **50**:3 (1992), 479–499.

[Jasiuk et al. 1992] I. Jasiuk, J. Chen, and M. F. Thorpe, "Elastic properties of two-dimensional composites containing polygonal holes", pp. 61–73 in *Processing, fabrication and manufacturing of composite materials*, vol. 35, edited by T. S. Srivatsan and E. L. Lavernia, ASME, New York, 1992.

[Jasiuk et al. 1994] I. Jasiuk, J. Chen, and M. F. Thorpe, "Elastic moduli of two dimensional materials with polygonal and elliptical holes", *Appl. Mech. Rev.* **47**:1S (1994), S18–S28.

[Koroteeva et al. 2010] O. Koroteeva, S. G. Mogilevskaya, S. Crouch, and E. Gordeliy, "A computational technique for evaluating the effective thermal conductivity of isotropic porous materials", *Eng. Anal. Bound. Elem.* **34**:9 (2010), 793–801.

[Kushch 2013] V. I. Kushch, *Micromechanics of composites: multipole expansion approach*, Butterworth Heinemann, Amsterdam, 2013.

[Kushch and Knyazeva 2016] V. I. Kushch and A. G. Knyazeva, "Finite cluster model and effective conductivity of a composite with non-randomly oriented elliptic inclusions", *Acta Mech.* **227**:1 (2016), 113–126.

[Kushch and Sevostianov 2015] V. I. Kushch and I. Sevostianov, "Effective elastic moduli of a particulate composite in terms of the dipole moments and property contribution tensors", *Int. J. Solids Struct.* **53** (2015), 1–11.

[Kushch and Sevostianov 2016] V. I. Kushch and I. Sevostianov, "Maxwell homogenization scheme as a rigorous method of micromechanics: application to effective conductivity of a composite with spheroidal particles", *Int. J. Eng. Sci.* **98** (2016), 36–50.

[Kushch et al. 2013] V. I. Kushch, S. G. Mogilevskaya, H. Stolarski, and S. Crouch, "Evaluation of the effective elastic moduli of particulate composites based on Maxwell's concept of equivalent inhomogeneity: microstructure-induced anisotropy", *J. Mech. Mater. Struct.* **8**:5-7 (2013), 283–303.

[Kushch et al. 2014] V. I. Kushch, I. Sevostianov, and V. S. Chernobai, "Effective conductivity of composite with imperfect contact between elliptic fibers and matrix: Maxwell's homogenization scheme", *Int. J. Eng. Sci.* **83** (2014), 146–161.

[Kuster and Toksöz 1974] G. T. Kuster and M. N. Toksöz, "Velocity and attenuation of seismic waves in two-phase media, part I: theoretical formulations", *Geophys.* **39**:5 (1974), 587–606.

[Levin et al. 2012] V. Levin, S. Kanaun, and M. Markov, "Generalized Maxwell's scheme for homogenization of poroelastic composites", *Int. J. Eng. Sci.* **61** (2012), 75–86.

[Linkov 2002] A. M. Linkov, *Boundary integral equations in elasticity theory*, Kluwer, Dordrecht, 2002.

[Lu 1998] S.-Y. Lu, "Effective conductivities of aligned spheroid dispersions estimated by an equivalent inclusion model", *J. Appl. Phys.* **84**:5 (1998), 2647–2655.

[Lu and Song 1996] S. Lu and J. Song, "Effective conductivity of composites with spherical inclusions: effect of coating and detachment", *J. Appl. Phys.* **79**:2 (1996), 609–618.

[Maxwell 1892] J. C. Maxwell, *Treatise on electricity and magnetism*, vol. 1, 3rd ed., Clarendon Press, Oxford, United Kingdom, 1892.

[McCartney 2010] L. N. McCartney, "Maxwell's far-field methodology predicting elastic properties of multiphase composites reinforced with aligned transversely isotropic spheroids", *Philos. Mag.* **90**:31-32 (2010), 4175–4207.

[McCartney and Kelly 2008] L. N. McCartney and A. Kelly, "Maxwell's far-field methodology applied to the prediction of properties of multi-phase isotropic particulate composites", *Proc. R. Soc. A* **464**:2090 (2008), 423–446.

[Milton 2002] G. W. Milton, *The theory of composites*, Cambridge Monographs on Applied and Computational Mathematics **6**, Cambridge University Press, 2002.

[Mogilevskaya and Crouch 2013] S. G. Mogilevskaya and S. L. Crouch, "Combining Maxwell's methodology with the BEM for evaluating the two-dimensional effective properties of composite and micro-cracked materials", *Comput. Mech.* **51**:4 (2013), 377–389.

[Mogilevskaya and Nikolskiy 2015] S. G. Mogilevskaya and D. V. Nikolskiy, "The shape of Maxwell's equivalent inhomogeneity and 'strange' properties of regular polygons and other symmetric domains", *Quart. J. Mech. Appl. Math.* **68**:4 (2015), 363–385.

[Mogilevskaya and Stolarski 2015] S. G. Mogilevskaya and H. K. Stolarski, "On 'strange' properties of some symmetric inhomogeneities", *Proc. R. Soc. A.* **471**:2179 (2015), art. id 2015157.

[Mogilevskaya et al. 2010] S. G. Mogilevskaya, S. L. Crouch, H. K. Stolarski, and A. Benusiglio, "Equivalent inhomogeneity method for evaluating the effective elastic properties of unidirectional multi-phase composites with surface/interface effects", *Int. J. Solids Struct.* **47**:3-4 (2010), 407–418.

[Mogilevskaya et al. 2012a] S. G. Mogilevskaya, V. I. Kushch, O. Koroteeva, and S. L. Crouch, "Equivalent inhomogeneity method for evaluating the effective conductivities of isotropic particulate composites", *J. Mech. Mater. Struct.* **7**:1 (2012), 103–117.

[Mogilevskaya et al. 2012b] S. G. Mogilevskaya, H. K. Stolarski, and S. L. Crouch, "On Maxwell's concept of equivalent inhomogeneity: when do the interactions matter?", *J. Mech. Phys. Solids* **60**:3 (2012), 391–417.

[Mogilevskaya et al. 2013] S. G. Mogilevskaya, V. I. Kushch, H. K. Stolarski, and S. L. Crouch, "Evaluation of the effective elastic moduli of tetragonal fiber-reinforced composites based on Maxwell's concept of equivalent inhomogeneity", *Int. J. Solids Struct.* **50**:25-26 (2013), 4161–4172.

[Pyatigorets and Mogilevskaya 2011] A. V. Pyatigorets and S. G. Mogilevskaya, "Evaluation of effective transverse mechanical properties of transversely isotropic viscoelastic composite materials", *J. Compos. Mater.* **45**:25 (2011), 2641–2658.

[Sevostianov 2014] I. Sevostianov, "On the shape of effective inclusion in the Maxwell homogenization scheme for anisotropic elastic composites", *Mech. Mater.* **75** (2014), 45–59.

[Sevostianov and Giraud 2013] I. Sevostianov and A. Giraud, "Generalization of Maxwell homogenization scheme for elastic material containing inhomogeneities of diverse shape", *Int. J. Eng. Sci.* **64** (2013), 23–36.

[Sevostianov and Kachanov 2011] I. Sevostianov and M. Kachanov, "Elastic fields generated by inhomogeneities: far-field asymptotics, its shape dependence and relation to the effective elastic properties", *Int. J. Solids Struct.* **48**:16-17 (2011), 2340–2348.

[Shen and Li 2004] L. Shen and J. Li, "A numerical simulation for effective elastic moduli of plates with various distributions and sizes of cracks", *Int. J. Solids Struct.* **41**:26 (2004), 7471–7492.

[Shen and Yi 2000] L. Shen and S. Yi, "New solutions for effective elastic moduli of microcracked solids", *Int. J. Solids Struct.* **37**:26 (2000), 3525–3534.

[Shen and Yi 2001] L. Shen and S. Yi, "An effective inclusion model for effective moduli of heterogeneous materials with ellipsoidal inhomogeneities", *Int. J. Solids Struct.* **38**:32-33 (2001), 5789–5805.

[Torquato 2002] S. Torquato, *Random heterogeneous materials: microstructure and macroscopic properties*, Interdisciplinary Applied Mathematics **16**, Springer, New York, 2002.

[Weng 2010] G. J. Weng, "A dynamical theory for the Mori–Tanaka and Ponte Castañeda–Willis estimates", *Mech. Mater.* **42**:9 (2010), 886–893.

Received 4 Apr 2016. Revised 6 Oct 2016. Accepted 12 Oct 2016.

SOFIA G. MOGILEVSKAYA: mogil003@umn.edu
Department of Civil, Environmental, and Geo-Engineering, University of Minnesota, 500 Pillsbury Drive SE, Minneapolis, MN 55455, United States

DMITRY NIKOLSKIY: nikol047@umn.edu
Department of Civil, Environmental, and Geo-Engineering, University of Minnesota, 500 Pillsbury Drive SE, Minneapolis, MN 55455, United States

JOURNAL OF MECHANICS OF MATERIALS AND STRUCTURES
Vol. 12, No. 2, 2017
dx.doi.org/10.2140/jomms.2017.12.193

INTERFACIAL MICROSCOPIC BOUNDARY CONDITIONS ASSOCIATED WITH BACKSTRESS-BASED HIGHER-ORDER GRADIENT CRYSTAL PLASTICITY THEORY

MITSUTOSHI KURODA

A strategy for modeling various interfacial boundary conditions associated with a higher-order gradient crystal plasticity theory is proposed. The gradient theory employed is based on the concept of the backstress that is produced in response to the spatial variation of the geometrically necessary dislocation densities. To set arbitrary interfacial boundary conditions for the crystallographic slip at the continuum level, a model with a single scalar quantity that aims to control the slipping rate at an interface is introduced. This scalar quantity is intended to represent the resultant effects of microscopic mechanisms such as absorption, emission, and transmission of the dislocations at an interface or a grain boundary (GB). As a realistic application of this basic idea, an orientation-dependent GB model is proposed, which incorporates effects of the degree of misorientation between the adjacent grains as well as the orientation of the GB plane relative to the grains. To illustrate capabilities of the proposed model, the bicrystalline micropillar compression problem is considered. Finite element simulations are performed for the bicrystalline micropillars including either a large-angle grain boundary (LAGB) or a coherent twin boundary (CTB) parallel to the compression axis. The numerical results are qualitatively compared with experimental observations reported in the literature. It is shown that the proposed GB model has a capability to represent the overall material responses associated with both LAGB and CTB using the same material parameter values.

1. Introduction

Size-dependent mechanical behaviors are usually observed in metallic materials at the micrometer or smaller scales. Predictions of size-dependent material responses are particularly important in the fields of small-scale electromechanical systems and nanostructured metallic materials. A considerable number of studies have been done so far with the aim of incorporating the size-effect into plasticity theories since the pioneering work of Aifantis [1984; 1987]. Since the studies of Kröner [1963] and Mindlin [1964], nonlocal or higher-order gradient effects in elasticity have been discussed and investigated (e.g., [Gutkin and Aifantis 1999; Bacca et al. 2013]).

The crystal plasticity theory (e.g., [Peirce et al. 1983; Asaro and Needleman 1985]) is a physically based model that accounts for the mechanisms of crystallographic slips in metals. However, it does not account for any size effects intrinsic in the materials. Extensions of the conventional crystal plasticity theory to incorporate the size effects have been proposed in many studies so far.

One of the methods of introducing the size effects into crystal plasticity theory is to formulate plastic-strain-gradient-dependent work hardening laws (e.g., [Acharya and Bassani 2000; Ohashi 2005]). Spatial

Keywords: strain gradient plasticity, crystal plasticity, interfaces, grain boundaries, geometrically necessary dislocations.

gradients of plastic strain (or crystallographic slips) correspond to the densities of geometrically necessary dislocations (GNDs) [Ashby 1970; Fleck et al. 1994]. The size effects can be introduced into conventional crystal plasticity models by assuming that the GNDs contribute to the increase in work hardening. In this type of modeling, only scalar quantities that represent the hardness of slip systems are augmented by a contribution from the GNDs. Therefore, the formulation of the boundary-value problem remains the same as that in the conventional theories. Only the tractions or prescribed displacements on the surfaces of a body are considered as the boundary conditions, and prescribing values of slips or their gradients at the boundaries is outside the scope.

Another method of incorporating the size effects, which is of interest in the present study, is higher-order extensions of the conventional theory (e.g., [Gurtin 2002; 2008a; Borg 2007; Yefimov et al. 2004b; Evers et al. 2004; Arsenlis et al. 2004; Bayley et al. 2006; Levkovitch and Svendsen 2006]). These higher-order theories open up the possibility of modeling extra boundary conditions for slips and their gradients at an interface or a grain boundary. Higher-order gradient crystal plasticity theories have been developed with two different trends so far. According to the classification proposed by Kuroda and Tvergaard [2008b], they are referred to as the "work-conjugate type" and "non-work-conjugate type" of theories. The first type is based on the concept of higher-order stresses that are introduced as work conjugates to spatial gradients of crystallographic slips and higher-order tractions that are postulated to exist as work conjugates to crystallographic slips on external surfaces or internal interfaces (e.g., [Gurtin 2002; 2008a]). This type introduces, as the major premise, a virtual work principle extended with the higher-order quantities and their work conjugates. Equilibrium or balance equations in the form of partial differential equations are derived from this premised virtual work statement. The second type is based on the concept of a *backstress*, that is, a long-range internal stress produced by an array of GNDs. The backstress effect can be incorporated directly into the conventional framework of a crystal plasticity theory (e.g., [Groma et al. 2003; Yefimov et al. 2004b; Evers et al. 2004; Arsenlis et al. 2004; Kuroda and Tvergaard 2006]). According to the classical dislocation theory, the spatial gradient of GND density is the origin of the backstress (equivalently, the internal stress), and superposition of the backstress and the externally induced resolved shear stress is taken to be an effective shear stress that activates slip deformations [Evers et al. 2004]. This second type of theory has a higher-order nature in the sense that extra boundary conditions for the crystallographic slips can be imposed, but it does not directly rely on higher-order stress quantities. Some mathematical equivalence between these two types of higher-order gradient crystal plasticity theories has been emphasized by Kuroda and Tvergaard [2008a; 2008b].

In the context of higher-order gradient crystal plasticity theories, two kinds of extreme extra boundary conditions have been mostly considered in previous applications. One is the *microscopically hard* condition, which supposes situations that all dislocations stop at the boundary and consequently the slip or its rate is fully constrained at the boundary. The other is the *microscopically free* condition, which assumes that the higher-order traction is zero in the work-conjugate type formulation [Gurtin 2002] or no GND density is required at the boundary in the non-work-conjugate type formulation [Evers et al. 2004; Kuroda and Tvergaard 2008b]. Gurtin and Needleman [2005] proposed a model of grain boundary behavior within the work-conjugate type framework, which accounts for a flow of the Burgers vector across the GB, and suggested, as an example, the *defect-free* condition, which assumes that the Burgers vector flow out of one grain is equal to that into the adjacent grain. Recently, Gurtin [2008b] has proposed another model of grain boundary conditions, which accounts for grain misorientation and grain-boundary

orientation relative to the grains. Van Beers et al. [2013] proposed a model of grain boundary interface mechanics based on a mixed treatment of the work-conjugate and non-work-conjugate formulations, in which the slip rates at the grain boundary are assumed to be governed by bulk-induced and energetic interfacial higher-order microforces. Ekh et al. [2011] proposed a grain boundary model in which a newly defined grain boundary microstress is assumed to activate the slip at the boundary, depending on the misorientation between the adjacent grains. Wulfinghoff et al. [2013] and Bayerschen et al. [2015] proposed a gradient plasticity model with an interface yield condition that accounts for the resistance of grain boundaries against plastic flow occurrence. They used an equivalent strain rather than slips on the individual slip systems as a fundamental field variable in order to simplify the formulation of the model.

Recently, for the purpose of clarifying the nature and roles of grain boundaries, experimental studies on bicrystalline micropillars have been conducted. Ng and Ngan [2009] and Imrich et al. [2014] independently showed that a large-angle grain boundary (LAGB) can act as a strong barrier to mobile dislocations, leading to a significant dislocation pile-up and an increase in dislocation density, for the size range (diameter or edge length of micropillars) of 6–7 μm. In contrast, Kunz et al. [2011] reported a completely opposite observation on submicron-sized bicrystalline pillars. The grain boundaries in their specimens seemed to act as sinks absorbing dislocations. Kim et al. [2015] stated that the LAGB in their submicrometer-sized bicrystalline pillar showed an ability to nucleate dislocations and did not act as a strong barrier to dislocations. These observations confirm that the nature of grain boundaries is complex and is not simply a function of the orientation of the boundary with respect to the grains or the relative misorientation of the grains. According to the studies of Ng and Ngan [2009], Kunz et al. [2011], and Imrich et al. [2014], for micropillars of different sizes, the distance from the grain boundary to the free surface may have some influence on the nature of the grain boundaries. Imrich et al. [2014] further carried out compression tests on a bicrystalline micropillar with a size of $\sim 4\,\mu$m and a coherent twin boundary (CTB). The CTB sample showed mechanical behavior very similar to that of single-crystalline samples, as if no grain boundary had existed. Hirouchi and Shibutani [2014] also conducted compression tests on copper bicrystalline micropillars with $\Sigma 3$ CTB and found that the bicrystalline micropillars exhibited a stress-strain response and deformation behavior fundamentally similar to those of single-crystalline micropillars having one of the crystal orientations that constitutes the bicrystalline micropillars.

In the present study, an alternative strategy for treating the higher-order interfacial boundary conditions within the non-work-conjugate type (or backstress-based) framework of the gradient crystal plasticity theory is proposed. To treat various interfacial boundary conditions for the crystallographic slip in a simplified manner, a model with a single scalar quantity that aims to control the slipping rate at an interface is introduced. This scalar quantity represents the resistance of an interface or a grain boundary to slip occurrence, which results from finer-scale phenomena such as absorption, emission, and transmission of the dislocations that are not resolved in the continuum modeling of crystal plasticity. As mentioned above, the grain boundary nature observed in experiments reported in the literature is complex. The real mechanism by which the observed grain boundary behavior is manifested has not been clarified sufficiently at present. Given this circumstance, the proposed model may seem to be rather phenomenological. However, it has plenty of room for extension, which can incorporate geometric relations of adjacent grains, grain boundary yielding, and many other phenomena that are likely to occur at the grain boundaries and internal interfaces. The present model may also be used to represent specific characteristics of external surfaces partially penetrable to dislocations, which may correspond to surfaces

having fragile oxide layers or microscopically incomplete contact surfaces. The first part of the paper is devoted to illustrating the basic idea of the proposed model and demonstration of its fundamental nature through analysis of a typical benchmark problem, i.e., the constrained simple shear problem. In the following parts, a generalization of the model and its application to a practical problem are presented. The bicrystalline micropillar compression problem is adopted to illustrate the efficiency of the proposed model.

2. Illustrations of basic idea

2.1. ***Backstress-based higher-order gradient crystal plasticity theory: the simplest version.*** To illustrate the fundamental nature of the proposition introduced in the present paper, we confine our attention to a backstress-based higher-order gradient crystal plasticity theory that is as simple as possible but not too simple [Kuroda and Tvergaard 2006]. In the subsequent sections that are devoted to its generalization and application to a practical problem, we will employ a much more generalized version of the theory [Kuroda and Tvergaard 2008a; 2008b].

Under a small strain assumption, the total strain rate $\dot{\boldsymbol{E}}$ is assumed to be decomposed into elastic and plastic parts:

$$\dot{\boldsymbol{E}} = (\nabla \otimes \dot{\boldsymbol{u}})_{\mathrm{sym}} = \dot{\boldsymbol{E}}^{\mathrm{e}} + \dot{\boldsymbol{E}}^{\mathrm{p}}, \tag{1}$$

where $\dot{\boldsymbol{u}}$ is the displacement rate vector, ∇ is the spatial gradient operator, $\otimes$ is the tensor product, the subscript sym denotes the symmetric part of the tensor, the superscripts e and p stand for "elastic" and "plastic", respectively, and a superposed dot denotes the material-time derivative.

Hooke's law is applied to represent elasticity,

$$\dot{\boldsymbol{E}}^{\mathrm{e}} = \boldsymbol{C}^{-1} : \dot{\boldsymbol{\sigma}}, \tag{2}$$

where $\boldsymbol{C}$ is a fourth-order elasticity modulus tensor, the superscript -1 denotes the tensor inverse, and $\boldsymbol{\sigma}$ is a symmetric (Cauchy) stress. Plastic deformation is assumed to take place through a single slip:

$$\dot{\boldsymbol{E}}^{\mathrm{p}} = \dot{\gamma}\, \boldsymbol{P}, \quad \boldsymbol{P} = (\boldsymbol{s} \otimes \boldsymbol{m})_{\mathrm{sym}}, \tag{3}$$

where $\dot{\gamma}$ is the slip rate, $\boldsymbol{s}$ and $\boldsymbol{m}$ are the unit vectors specifying the slip direction and slip plane normal, respectively, and $\boldsymbol{P}$ is the Schmid tensor. In this simplified theory, it is assumed that $\boldsymbol{s}$ and $\boldsymbol{m}$ constitute a planar slip system, i.e., they are both on the X_1-X_2 plane and $\boldsymbol{p} = \boldsymbol{s} \times \boldsymbol{m}$ is parallel to the X_3-axis.

The yield plane in the stress space is defined by

$$f = |\tau - \tau_{\mathrm{b}}| - g = 0, \tag{4}$$

where τ, τ_{b}, and g are the resolved shear stress (RSS), backstress, and critical resolved shear stress (CRSS) respectively given by

$$\tau = \boldsymbol{\sigma} : \boldsymbol{P}, \quad \tau_{\mathrm{b}} = \beta \nabla \rho_{\mathrm{G}} \cdot \boldsymbol{s}, \quad g = \tau_0 + h \int_0^t |\dot{\gamma}|\, \mathrm{d}t. \tag{5}$$

Here, ρ_{G} is the geometrically necessary dislocation (GND) density, β is a coefficient for dimensional consistency with dimensions of [force $\times$ length], which is assumed to be constant, τ_0 is an initial value

of CRSS, h is a slip hardening modulus taken to be constant for simplicity, and t is time. The GND density ρ_{G} must satisfy the relation [Ashby 1970; Arsenlis and Parks 1999]

$$\rho_{\mathrm{G}} + \frac{1}{b}\nabla\gamma \cdot \boldsymbol{s} = 0, \tag{6}$$

where b is the magnitude of the Burgers vector. Note that ρ_{G} in $(5)_2$ and (6) represents the density of edge-type GNDs[1] as we consider the planar slip system.

For continued plastic deformation, the stress point must remain on the yield plane; therefore,

$$\dot{f} = \frac{\partial \tau}{\partial \boldsymbol{\sigma}} : \dot{\boldsymbol{\sigma}} - \beta \nabla \dot{\rho}_{\mathrm{G}} \cdot \boldsymbol{s} - h\dot{\gamma} = 0, \tag{7}$$

which leads to

$$\dot{\gamma} = \frac{\boldsymbol{P} : \boldsymbol{C} : \dot{\boldsymbol{E}} - \beta \nabla \dot{\rho}_{\mathrm{G}} \cdot \boldsymbol{s}}{A}, \quad A = \boldsymbol{P} : \boldsymbol{C} : \boldsymbol{P} + h. \tag{8}$$

In the derivation of the above relation, it is assumed that the signs of $\dot{\gamma}$ and $\tau - \tau_{\mathrm{b}}$ are identified. Substituting (8) into (3), and combining it with (2) and (1), we have the elastoplasticity constitutive relation

$$\dot{\boldsymbol{\sigma}} = \boldsymbol{C}^{\mathrm{ep}} : \dot{\boldsymbol{E}} + \frac{\beta}{A}\boldsymbol{C} : \boldsymbol{P} \nabla \dot{\rho}_{\mathrm{G}} \cdot \boldsymbol{s}, \tag{9}$$

where

$$\boldsymbol{C}^{\mathrm{ep}} = \boldsymbol{C} - \frac{1}{A}(\boldsymbol{C} : \boldsymbol{P}) \otimes (\boldsymbol{P} : \boldsymbol{C}). \tag{10}$$

Now, we introduce an incremental form of the virtual work principle as

$$\int_V \dot{\tilde{\boldsymbol{E}}} : \dot{\boldsymbol{\sigma}} \, \mathrm{d}V = \int_{S_t} \dot{\tilde{\boldsymbol{u}}} \cdot \dot{\underline{\boldsymbol{t}}} \, \mathrm{d}S, \quad \dot{\tilde{\boldsymbol{E}}} = (\dot{\tilde{\boldsymbol{u}}} \otimes \nabla)_{\mathrm{sym}}. \tag{11}$$

Here, $\dot{\tilde{\boldsymbol{u}}}$ is the virtual displacement rate that takes zero on part of the surface, S_u, where real displacement rates are prescribed, otherwise it can take any arbitrary value, and $\dot{\underline{\boldsymbol{t}}}$ is the surface traction rate prescribed on the remaining part of the surface, S_t (recall that formally we write $S = S_t \cup S_u$ with the total surface S of the body under consideration). Substituting (9) into (11) gives

$$\int_V \dot{\tilde{\boldsymbol{E}}} : \boldsymbol{C}^{\mathrm{ep}} : \dot{\boldsymbol{E}} \, \mathrm{d}V + \int_V \dot{\tilde{\boldsymbol{E}}} : \boldsymbol{C} : \boldsymbol{P} \frac{\beta}{A} \nabla \dot{\rho}_{\mathrm{G}} \cdot \boldsymbol{s} \, \mathrm{d}V = \int_{S_t} \dot{\tilde{\boldsymbol{u}}} \cdot \dot{\underline{\boldsymbol{t}}} \, \mathrm{d}S. \tag{12}$$

Equation (12) has two independent variables, $\dot{\boldsymbol{u}}$ and $\dot{\rho}_{\mathrm{G}}$, which cannot be determined by a single equation.

Now, we view (6) as an additional governing equation implying that the GND density balances with the spatial gradient of a slip in the slip direction. A weak form of the incremental relation of (6) becomes

$$\int_V \tilde{\rho}\dot{\rho}_{\mathrm{G}} \, \mathrm{d}V - \int_V \frac{1}{b}\nabla\tilde{\rho} \cdot \boldsymbol{s}\dot{\gamma} \, \mathrm{d}V = -\int_{S_\gamma} \frac{1}{b}\tilde{\rho}\boldsymbol{n} \cdot \boldsymbol{s}\underline{\dot{\gamma}} \, \mathrm{d}S, \tag{13}$$

where $\tilde{\rho}$ is a virtual weighting function that is zero on part of the surface, S_ρ, where $\dot{\rho}_{\mathrm{G}}$ is prescribed, otherwise it can take any arbitrary value, $\boldsymbol{n}$ is a unit normal to the boundary, and $\underline{\dot{\gamma}}$ is a slip rate prescribed

[1] Different researchers sometimes use different sign conventions for the GND densities. The sign convention for the edge-type GND density in (6) follows that introduced by Arsenlis and Parks [1999].

on part of the surface, S_γ (formally we consider $S = S_\rho \cup S_\gamma$), except for the special case of $\boldsymbol{n}\cdot\boldsymbol{s} = 0$, where $\underline{\dot{\gamma}}$ must be free of any constraint. Substituting (8) into (13) gives

$$-\int_V \frac{1}{bA}\nabla\tilde{\rho}\cdot(\boldsymbol{s}\otimes\boldsymbol{P}):\boldsymbol{C}:\dot{\boldsymbol{E}}\,\mathrm{d}V + \int_V\left[\tilde{\rho}\dot{\rho}_{\mathrm{G}} + \frac{\beta}{bA}\nabla\tilde{\rho}\cdot(\boldsymbol{s}\otimes\boldsymbol{s})\cdot\nabla\dot{\rho}_{\mathrm{G}}\right]\mathrm{d}V = -\int_{S_\gamma}\frac{1}{b}\tilde{\rho}\boldsymbol{n}\cdot\boldsymbol{s}\underline{\dot{\gamma}}\,\mathrm{d}S. \quad (14)$$

2.2. ***Treatment of microscopic boundary conditions: a proposition.*** In previous studies [Evers et al. 2004; Kuroda and Tvergaard 2006; 2008a; 2008b], the following two types of microscopic boundary condition have been considered:

- Microscopically hard condition:

$$\boldsymbol{n}\cdot\boldsymbol{s}\underline{\dot{\gamma}} = 0, \quad (15)$$

- Microscopically free condition:

$$\dot{\rho}_{\mathrm{G}} = 0. \quad (16)$$

In general cases of $\boldsymbol{n}\cdot\boldsymbol{s} \neq 0$, (15) is equivalent to $\underline{\dot{\gamma}} = 0$.

An alternative representation of the microscopic boundary conditions is considered. Suppose that the value of $\underline{\dot{\gamma}}$ coincides with $\dot{\gamma}$ given by (8) for $\boldsymbol{n}\cdot\boldsymbol{s} \neq 0$. In this case, the boundary is said to be *transparent*, i.e., it possesses the same property as that of the bulk part of the material. Now, we formally write the slip rate at the boundary as

$$\underline{\dot{\gamma}} = \phi\dot{\gamma}, \quad (17)$$

where ϕ is a dimensionless scalar quantity. Then, the two extreme boundary conditions can be written as

$$\phi = 1 \text{ for the transparent condition,} \quad (18)$$

$$\phi = 0 \text{ for the microscopically hard condition.} \quad (19)$$

Thus, the domain of ϕ is naturally assumed to be

$$0 \le \phi \le 1. \quad (20)$$

A value of ϕ within $0 < \phi < 1$ gives a relaxed microscopic boundary condition for the slip at an interface.

Substituting (17) with (8) into (14) gives

$$-\int_V \frac{1}{bA}\nabla\tilde{\rho}\cdot(\boldsymbol{s}\otimes\boldsymbol{P}):\boldsymbol{C}:\dot{\boldsymbol{E}}\,\mathrm{d}V + \int_{S_\gamma}\frac{\phi}{bA}\tilde{\rho}\boldsymbol{n}\cdot(\boldsymbol{s}\otimes\boldsymbol{P}):\boldsymbol{C}:\dot{\boldsymbol{E}}\,\mathrm{d}S$$
$$+\int_V\left[\tilde{\rho}\dot{\rho}_{\mathrm{G}} + \frac{\beta}{bA}\nabla\tilde{\rho}\cdot(\boldsymbol{s}\otimes\boldsymbol{s})\cdot\nabla\dot{\rho}_{\mathrm{G}}\right]\mathrm{d}V - \int_{S_\gamma}\frac{\phi\beta}{bA}\tilde{\rho}\boldsymbol{n}\cdot(\boldsymbol{s}\otimes\boldsymbol{s})\cdot\nabla\dot{\rho}_{\mathrm{G}}\,\mathrm{d}S = 0. \quad (21)$$

The present treatment of the boundary may also represent specific characteristics of external surfaces. For example, a strongly passivated surface is modeled by $\phi = 0$, and an external surface coated by an incomplete or fragile thin oxide layer that is partially penetrable to dislocations may be modeled by $0 < \phi < 1$. It is noted that Yefimov et al. [2004a] have assumed a condition equivalent to $\phi = 1$ (i.e., $\underline{\dot{\gamma}} = \dot{\gamma}$) to represent a perfect free surface of a bent foil specimen.

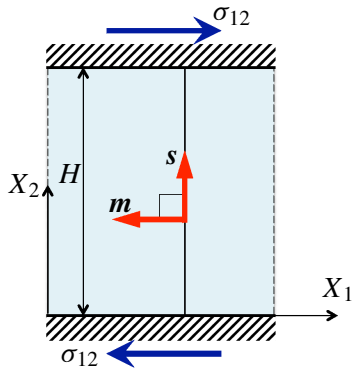

Figure 1. Constrained simple shear problem of a strip with an infinite lateral length and a single slip system whose slip direction is parallel to the thickness direction. The microscopically hard condition is imposed on the bottom surface, whereas flexible boundary conditions ($0 \le \phi \le 1$) are adopted on the upper surface.

2.3. ***Finite element equation.*** A finite element equation for the present model is derived straightforwardly from (12) and (21), choosing $\dot{\boldsymbol{u}}$ and $\dot{\rho}_{\mathrm{G}}$ as the nodal quantities to be solved. It is written as

$$\begin{bmatrix} \boldsymbol{K}_{(uu)} & \boldsymbol{K}_{(u\rho)} \\ \boldsymbol{K}_{(\rho u)} & \boldsymbol{K}_{(\rho\rho)} \end{bmatrix} \begin{Bmatrix} \dot{\boldsymbol{U}} \\ \dot{\boldsymbol{P}}_{\mathrm{G}} \end{Bmatrix} = \begin{Bmatrix} \dot{\boldsymbol{F}} \\ \boldsymbol{0} \end{Bmatrix}, \tag{22}$$

where $\{\dot{\boldsymbol{U}}\}$ is a vectorial array of nodal values of $\dot{\boldsymbol{u}}$, $\{\dot{\boldsymbol{P}}_{\mathrm{G}}\}$ is a vectorial array of nodal values of $\dot{\rho}_{\mathrm{G}}$, $[\boldsymbol{K}_{(\mathrm{ab})}]$ (where "a" and "b" stand for "u" or "ρ") are the corresponding stiffness matrices, and $\{\dot{\boldsymbol{F}}\}$ is a vectorial array of nodal forces, which corresponds to the right-hand side of (12). Actual numerical computations are performed using an adoptive forward Euler time integration scheme proposed by Yamada et al. [1968].

2.4. ***Illustrative examples.*** To illustrate the effects of the proposed microscopic boundary conditions, the constrained simple shear problem is considered. A strip with a height H in the X_2-direction and an infinite length in the X_1-direction is subjected to simple shear (Figure 1). This material has only one slip system whose slip direction and slip plane normal coincide with X_2- and negative X_1-directions, respectively. The bottom surface is assumed to act as a microscopically hard boundary (i.e., $\phi = 0$), whereas various values of ϕ in the range $0 \le \phi \le 1$ are applied to the top surface to see the fundamental nature of the proposed boundary model. The displacement rate $\dot{U}$ in the X_1-direction on the top surface is prescribed, and the macroscopic shear strain Γ is defined as $\Gamma = U/H$.

The thickness of the strip is discretized with 60 quadrilateral elements in the thickness (X_2-) direction, and only one element is assigned in the lateral (X_1-) direction. Periodic conditions are applied to both sides of the finite element model. The serendipity shape functions are used to interpolate the displacement rate field, while the bilinear shape functions are employed to interpolate the GND density rate field. The coordinates of the nodes in the bilinear four-node elements are set to be identical to those of the corner nodes in the serendipity eight-node elements. The Gaussian quadrature with 2×2 points is used for volume integrals and that with 2 points is used for surface integrals. This combination of the

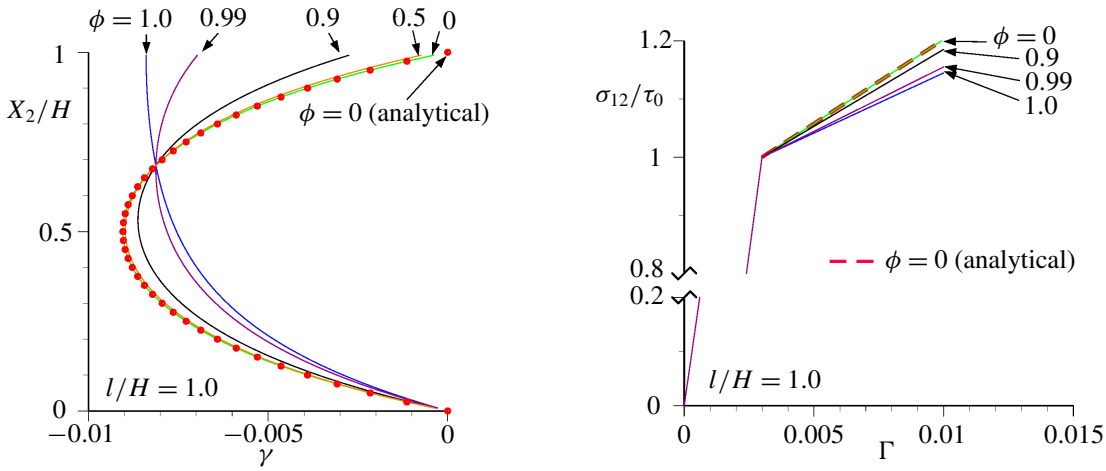

Figure 2. Computational results for constrained simple shear problem with relaxed microscopic boundary conditions at the upper surface for a relative length scale of $l/H = 1.0$. Distributions of slip in the thickness direction at a macroscopic shear strain Γ of 0.01 (left). Curves of shear stress versus macroscopic shear strain (right).

shape functions and the Gaussian quadrature order gives satisfactory numerical results free of volumetric locking and unexpected stress oscillation phenomena [Kuroda 2011; 2015].

The material constants are $\mu/\tau_0 = 333.3$ (μ is the shear elastic modulus) and $h/\tau_0 = 16.67$. The coefficient β in $(5)_2$ is formulated as

$$\beta = l^2 b \tau_0, \tag{23}$$

where l is a constant material length scale.

The responses of the strip with a size of $l/H = 1$ are shown in Figure 2. The distributions of slip γ in the X_2-direction at $\Gamma = 0.01$ are depicted[2] in Figure 2 (left) for ϕ values of $0 \le \phi \le 1$. Curves of the shear stress σ_{12} (that equals $-\tau$) versus Γ are plotted in Figure 2 (right). For $\phi = 0$ (i.e., the microscopically hard condition), the analytical solution [Bittencourt et al. 2003] is also shown to validate the quality of the present finite element solutions. In Figure 2 (left), it is seen that the constraint on γ at $X_2 = H$ is released with the increase in ϕ. The slip distribution profile for $\phi = 0.5$ is comparable to that for $\phi = 0$. Even for $\phi = 0.9$, the value of γ at $X_2 = H$ is still smaller than half of the maximum of γ. In the range of $\phi > 0.9$, the slip distribution profile is sensitively changed with ϕ. For $\phi = 1$, the condition of $\mathrm{d}\dot{\gamma}/\mathrm{d}X_2 = 0$ (equivalently, $\dot{\rho}_{\mathrm{G}} = 0$ in this case) is established.

The distributions of slip at $\Gamma = 0.01$ for a relative length scale of $l/H = 0.3$ are depicted in Figure 3. In this case, clear *boundary layers* are formed. The overall behavior associated with the change in ϕ is similar to that for $l/H = 1$. Variation of the stress-strain curves due to a change in the interfacial

[2]The values of γ are computed at the Gaussian points and they are constant within each element in the present problem. The smoothly plotted curves shown in Figure 2 (left), as well as in Figure 3, are obtained using the values of γ evaluated at the positions of the *corner nodes* as the average of values in the adjacent elements. However, the values at the boundaries of the body cannot be evaluated in this manner. Thus, the computed curves do not reach the boundaries at $X_2/H = 0$ and 1 in Figures 2 (left) and 3.

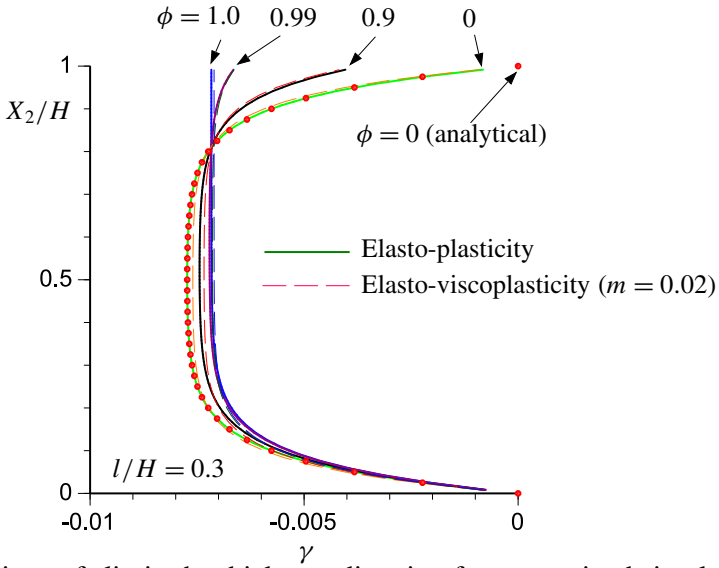

Figure 3. Distributions of slip in the thickness direction for constrained simple shear problem with relaxed microscopic boundary conditions at the upper surface for a relative length scale of $l/H = 0.3$ at $\Gamma = 0.01$.

microscopic boundary conditions is very small in the case of $l/H = 0.3$, and their depiction is omitted. The trend is fundamentally the same as that shown in Figure 2 (right) for $l/H = 1.0$.

In addition to the rate-independent elasto-plasticity analysis, an elasto-viscoplastic version of the theory, which has been frequently employed in previous studies [Kuroda and Tvergaard 2006; 2008a; 2008b; El-Naaman et al. 2016], is examined here. The power law relation is used, instead of the yield condition (4), given as

$$\dot{\gamma} = \operatorname{sgn}(\tau - \tau_{\mathrm{b}})\dot{\gamma}_0 \left(\frac{|\tau - \tau_{\mathrm{b}}|}{g} \right)^{1/m}, \tag{24}$$

where m is a rate sensitivity exponent and $\dot{\gamma}_0$ is a reference slip rate. In the present example, m is chosen to be 0.02, which is a realistic value for common metals at room temperature, and $\dot{\gamma}_0$ is identified with $\dot{\Gamma}$ in the computations. In the limit $m \to 0$, (24) reduces to (4). In the finite element computations of the elasto-viscoplastic version, (13) is directly used for the GND density analysis, as in previous studies [Kuroda and Tvergaard 2006; 2008a; 2008b]. Equation (17) with (24) is applied to the right-hand side of (13). It has been confirmed that the responses of an elasto-viscoplastic material governed by (24) with the microscopic boundary conditions prescribed by the use of (17) approximate the corresponding elasto-plasticity responses, as observed in Figure 3. Note that an extrapolation is required to evaluate a value of $\dot{\gamma}$ at the edge of the element at the boundary because $\dot{\gamma}$ is computed inside the element in the present theory. In the present simple shear problem with the finite element type used here, the value of $\dot{\gamma}$ is constant within each element, and this constant value has been used as the extrapolated value at the edge of the element at the upper end of the finite element model. The effect of such extrapolation on the solution is subordinated in an appropriately discretized finite element meshing.

2.5. ***Three-dimensional, multislip description of the theory.*** In the above, we confined our attention to the simplified theory with a single-slip system in the two-dimensional setting to illustrate the basic idea of

the interfacial boundary condition newly proposed. The three-dimensional form of the theory with multi-slip systems (but still in the small strain regime [Kuroda and Tvergaard 2008b]) is briefly described below.

For multislip conditions, adoption of the viscoplastic formulation is advantageous because it is free from the problem of the unique determination of the slip rate on each slip system, which is encountered in rate-independent crystal plasticity analyses. Thus, (24) is extended to

$$\dot{\gamma}^{(\alpha)} = \operatorname{sgn}(\tau^{(\alpha)} - \tau_{\mathrm{b}}^{(\alpha)})\dot{\gamma}_0 \left(\frac{|\tau^{(\alpha)} - \tau_{\mathrm{b}}^{(\alpha)}|}{g^{(\alpha)}} \right)^{1/m}, \tag{25}$$

where α is the slip system number, and

$$\tau^{(\alpha)} = \boldsymbol{\sigma} : \boldsymbol{P}^{(\alpha)}; \quad \boldsymbol{P}^{(\alpha)} = (\boldsymbol{s}^{(\alpha)} \otimes \boldsymbol{m}^{(\alpha)})_{\mathrm{sym}}, \tag{26}$$

$$g^{(\alpha)} = \tau_0 + \int_0^t \sum_{\beta} h^{(\alpha\beta)} |\dot{\gamma}^{(\beta)}| \, \mathrm{d}t, \tag{27}$$

$$\tau_{\mathrm{b}}^{(\alpha)} = l^2 b \tau_0 (\nabla \rho_{\mathrm{G(e)}}^{(\alpha)} \cdot \boldsymbol{s}^{(\alpha)} + \nabla \rho_{\mathrm{G(s)}}^{(\alpha)} \cdot \boldsymbol{p}^{(\alpha)}). \tag{28}$$

Here, $h^{(\alpha\beta)}$ is a slip hardening moduli matrix that can incorporates latent hardening effects[3], $\rho_{\mathrm{G(e)}}^{(\alpha)}$ is the density of the edge-type GNDs, $\rho_{\mathrm{G(s)}}^{(\alpha)}$ is the density of the screw-type GNDs, and $\boldsymbol{p}^{(\alpha)} = \boldsymbol{s}^{(\alpha)} \times \boldsymbol{m}^{(\alpha)}$. In (28), interactions between the slip systems are neglected for simplicity within the present paper. More elaborate backstress models with the slip system interactions were proposed by Evers et al. [2004] and Bayley et al. [2006], and were used in [Kuroda and Tvergaard 2008a; 2008b] and [Kuroda 2013].

Weak forms of the incremental relations of the edge- and screw-type GND density balances[4] are, respectively,

$$\int_V \tilde{\rho} \dot{\rho}_{\mathrm{G(e)}}^{(\alpha)} \, \mathrm{d}V - \int_V \frac{1}{b} \nabla \tilde{\rho} \cdot \boldsymbol{s}^{(\alpha)} \dot{\gamma}^{(\alpha)} \, \mathrm{d}V = - \int_{S_\gamma} \frac{1}{b} \tilde{\rho} \boldsymbol{n} \cdot \boldsymbol{s}^{(\alpha)} \underline{\dot{\gamma}}^{(\alpha)} \, \mathrm{d}S, \tag{29}$$

$$\int_V \tilde{\rho} \dot{\rho}_{\mathrm{G(s)}}^{(\alpha)} \, \mathrm{d}V - \int_V \frac{1}{b} \nabla \tilde{\rho} \cdot \boldsymbol{p}^{(\alpha)} \dot{\gamma}^{(\alpha)} \, \mathrm{d}V = - \int_{S_\gamma} \frac{1}{b} \tilde{\rho} \boldsymbol{n} \cdot \boldsymbol{p}^{(\alpha)} \underline{\dot{\gamma}}^{(\alpha)} \, \mathrm{d}S, \tag{30}$$

with

$$\underline{\dot{\gamma}}^{(\alpha)} = \phi^{(\alpha)} \dot{\gamma}^{(\alpha)}. \tag{31}$$

A finite strain version of the theory has been given in [Kuroda and Tvergaard 2008a]. Equations for the finite strain version are not repeated here for brevity.

3. Strategy for generalization of $\phi^{(\alpha)}$

Consider a body composed of two parts (which may be grains), A and B, with a grain boundary (GB) or an interface S_{GB} (Figure 4). Under multislip situations, the expression of the present boundary model (17) is extended to

$$\underline{\dot{\gamma}}_{\mathrm{A}}^{(\alpha)} = \phi_{\mathrm{A}}^{(\alpha)} \dot{\gamma}_{\mathrm{A}}^{(\alpha)} \text{ on } S_{\mathrm{GB(A)}} \quad \text{and} \quad \underline{\dot{\gamma}}_{\mathrm{B}}^{(\beta)} = \phi_{\mathrm{B}}^{(\beta)} \dot{\gamma}_{\mathrm{B}}^{(\beta)} \text{ on } S_{\mathrm{GB(B)}}, \tag{32}$$

[3]Recently, a model of size-dependent latent hardening has been proposed by Bardella et al. [2013]. Such an effect has yet to be introduced in the present model.

[4]Different researchers use different sign conventions for the screw-type GND density. The sign convention for the screw-type GND density in (30) follows that used by Gurtin [2002; 2008b].

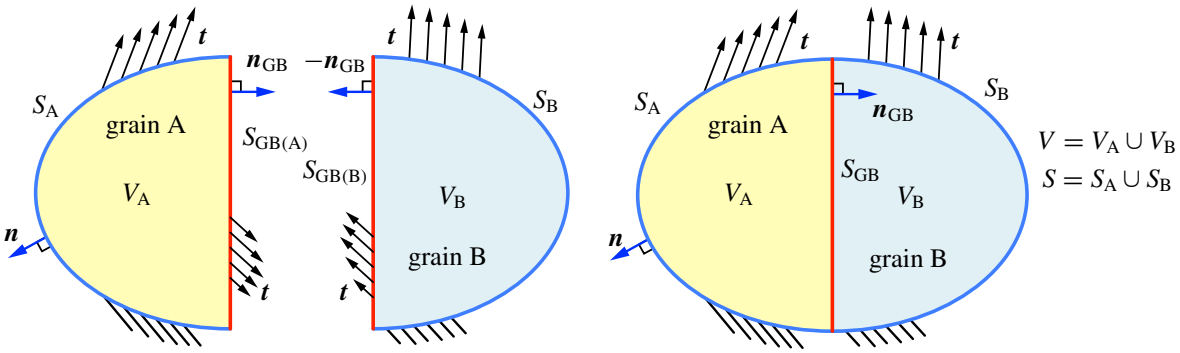

Figure 4. Schematic illustration of a body with a grain boundary. Separated description of grains A and B (left); grains A and B joined into a single body (right).

where the subscripts A and B denote that the corresponding quantities belongs to grain A or B, and the superscript α and β represent the slip system number given within grains A and B, respectively, and $S_{GB(A)}$ and $S_{GB(B)}$ are the interfacial surfaces seen from grains A and B, respectively. In general, the continuum modeling of crystal plasticity, in which crystallographic slips are taken as a fundamental deformation process, cannot directly resolve the individual dislocation behaviors such as absorption, emission (or subsequent reemission), and transmission, which would be observed at a finer scale. The resultant amount of slip rate resulting from these multiple phenomena is quantified via $\phi_I^{(i)}$ (with $I = \mathrm{A}$ or B and $i = \alpha$ or β for brevity). The coefficient $\phi_I^{(i)}$ is said to give a mesoscopic representation of the resistance of the interface to slip occurrence. In this modeling, the value of $\phi_{\mathrm{A}}^{(\alpha)}$ for grain A may be determined independently of information from grain B, and vice versa, for a supposed situation where the boundary on the grain A side acts as the dislocation sink and source, whereas the boundary on the grain B side functions as a strong barrier to dislocations. On the other hand, it is possible to consider grain interactions. Even in that case, it is reasonable to consider that $\phi_I^{(i)}$ does not become more than unity because the slip behavior at a point infinitesimally close to the GB must be governed by the mechanical conditions at that point located *inside* the grain. A negative $\phi_I^{(i)}$ is also inconsistent with the mechanical conditions at the point infinitesimally close to the GB. Available experimental data is not sufficient for formulating a unique form for the function $\phi_I^{(i)}$. However, it is generally expected that $\phi_I^{(i)}$ will be affected by a relative misorientation of the grains; the orientation of the GB relative to the grains; the spacing between the GB and the external surface; the thickness, structure, and amount of precipitation of the GB; temperature; and maybe some other factors.

In the current modeling, $\dot{\underline{\gamma}}_{\mathrm{A}}^{(\alpha)}$ at a point on the grain A side of the interface depends only on the slip rate $\dot{\gamma}_{\mathrm{A}}^{(\alpha)}$ in grain A. One might conceive a more elaborate and complicated formulation of $\dot{\underline{\gamma}}_{\mathrm{A}}^{(\alpha)}$ that also incorporates the influences of the slip rates $\dot{\gamma}_{\mathrm{B}}^{(\beta)}$ in grain B. This coupling, which induces a significant complexity in the formulation and computational procedure, is omitted in the present study. Nevertheless, this simple model has the capability to represent a rather wide range of material responses at the micrometer scale, as will be demonstrated in the next section.

In the following application, we consider a simple formulation that only takes into account the geometrical configuration of the slip systems and the GB plane (i.e., the degree of misorientation between

grains A and B, and the orientation of the GB plane relative to the grains):

$$\phi_{\mathrm{A}}^{(\alpha)} = (\max_{\beta} \bar{C}_{\mathrm{AB}}^{(\alpha\beta)})^{\nu}, \quad \phi_{\mathrm{B}}^{(\beta)} = (\max_{\alpha} \bar{C}_{\mathrm{AB}}^{(\alpha\beta)})^{\nu}, \tag{33}$$

where ν (≥ 0) is a scaling exponent, and the moduli $\bar{C}_{\mathrm{AB}}^{(\alpha\beta)}$ represent the degree of misorientation between the two adjacent grains and the GB orientation relative to those grains. The moduli $\bar{C}_{\mathrm{AB}}^{(\alpha\beta)}$ are given by

$$\begin{aligned} \bar{C}_{\mathrm{AB}}^{(\alpha\beta)} &= \left| \boldsymbol{s}_{\mathrm{A}}^{(\alpha)} \cdot \boldsymbol{s}_{\mathrm{B}}^{(\beta)} \right| \left| \bar{\boldsymbol{q}}_{\mathrm{A}}^{(\alpha)} \cdot \bar{\boldsymbol{q}}_{\mathrm{B}}^{(\beta)} \right|, \\ \bar{\boldsymbol{q}}_{\mathrm{A}}^{(\alpha)} &= \frac{\boldsymbol{m}_{\mathrm{A}}^{(\alpha)} \times \boldsymbol{n}_{\mathrm{GB}}}{\| \boldsymbol{m}_{\mathrm{A}}^{(\alpha)} \times \boldsymbol{n}_{\mathrm{GB}} \|}, \quad \bar{\boldsymbol{q}}_{\mathrm{B}}^{(\beta)} = \frac{\boldsymbol{m}_{\mathrm{B}}^{(\beta)} \times \boldsymbol{n}_{\mathrm{GB}}}{\| \boldsymbol{m}_{\mathrm{B}}^{(\beta)} \times \boldsymbol{n}_{\mathrm{GB}} \|}, \end{aligned} \tag{34}$$

where $\boldsymbol{n}_{\mathrm{GB}}$ is the GB normal that points from grain A to grain B, and $\boldsymbol{s}_I^{(i)}$ and $\boldsymbol{m}_I^{(i)}$ are respectively the slip direction and the slip plane normal that constitute the slip systems in each grain. The condition $0 \leq \bar{C}_{\mathrm{AB}}^{(\alpha\beta)} \leq 1$ leads to $0 \leq \phi_I^{(i)} \leq 1$. The basic idea for $\bar{C}_{\mathrm{AB}}^{(\alpha\beta)}$ can be found in [Clark et al. 1992], and it has recently been employed by Knorr et al. [2015] and Kheradmand et al. [2016] to evaluate the *slip transfer resistance of neighboring grains*[5] in problems of crack initiation at grain boundaries and deformation in micrometer-sized bicrystals. Figure 5 shows a schematic diagram of the geometrical configuration of the slip systems and the GB plane, which characterize values of $\bar{C}_{\mathrm{AB}}^{(\alpha\beta)}$. Using $\kappa_{\mathrm{AB}}^{(\alpha\beta)}$ to denote the angle between intersection lines of opposite slip planes from the neighboring grains on the GB plane and $\theta_{\mathrm{AB}}^{(\alpha\beta)}$ to denote the angle between the slip directions of opposite slip systems of the neighboring grains, then we can write $\bar{C}_{\mathrm{AB}}^{(\alpha\beta)} = |\cos\theta_{\mathrm{AB}}^{(\alpha\beta)}||\cos\kappa_{\mathrm{AB}}^{(\alpha\beta)}|$. In the current formulation of (33), the slip resistance is determined by the most orientationally favorable slip system in the neighboring grain, which has the largest value of $\bar{C}_{\mathrm{AB}}^{(\alpha\beta)}$. One of the most critical situations described using this model may be coherent twin boundaries (CTBs). Consider that the slip system α in grain A and the slip system β in grain B have the same Burgers vector that is parallel to the CTB plane (i.e., a cross slip occurs across the CTB). Thus, $\phi_I^{(i)}$ takes unity regardless of the value of ν since $\bar{C}_{\mathrm{AB}}^{(\alpha\beta)}$ takes unity. This represents a fully transparent characteristic of the GB showing no resistance to slip occurrence. It is noted that Gurtin [2008b] derived similar grain interaction moduli,

$$C_{\mathrm{AB}}^{(\alpha\beta)} = \boldsymbol{s}_{\mathrm{A}}^{(\alpha)} \cdot \boldsymbol{s}_{\mathrm{B}}^{(\beta)} (\boldsymbol{m}_{\mathrm{A}}^{(\alpha)} \times \boldsymbol{n}_{\mathrm{GB}}) \cdot (\boldsymbol{m}_{\mathrm{B}}^{(\beta)} \times \boldsymbol{n}_{\mathrm{GB}}) \quad \text{for} \quad 0 \leq |C_{\mathrm{AB}}^{(\alpha\beta)}| \leq 1,$$

in the context of a different modeling of the GB. The main difference between (34) and Gurtin's moduli is whether $\boldsymbol{m}_I^{(i)} \times \boldsymbol{n}_{\mathrm{GB}}$ are normalized to unit vectors. The values of $|C_{\mathrm{AB}}^{(\alpha\beta)}|$ do not reach unity for the pair of slip systems positioned in the cross slip configuration at the GB. If $|C_{\mathrm{AB}}^{(\alpha\beta)}|$ is used in (33), such a model shows a GB response harder than that predicted using $\bar{C}_{\mathrm{AB}}^{(\alpha\beta)}$.

When $\boldsymbol{m}_I^{(i)}$ is parallel to $\boldsymbol{n}_{\mathrm{GB}}$, then the value of $\bar{\boldsymbol{q}}_I^{(i)}$ is indeterminant, but simultaneously $\boldsymbol{s}_I^{(i)} \cdot \boldsymbol{n}_{\mathrm{GB}} = 0$. In this case, $\dot{\gamma}_I^{(i)}$ is free from constraint,[6] as is understood directly from (13). The interpretation that a GB parallel to the slip plane does not act as an obstacle to slip deformation is physically acceptable [Kuroda and Tvergaard 2008b].

[5] Kheradmand et al. [2016] defined the grain boundary transmission factor as $\omega_{\mathrm{AB}}^{(\alpha\beta)} = 1 - |\boldsymbol{s}_{\mathrm{A}}^{(\alpha)} \cdot \boldsymbol{s}_{\mathrm{B}}^{(\beta)}||\bar{\boldsymbol{q}}_{\mathrm{A}}^{(\alpha)} \cdot \bar{\boldsymbol{q}}_{\mathrm{B}}^{(\beta)}| = 1 - |\cos\theta_{\mathrm{AB}}^{(\alpha\beta)}||\cos\kappa_{\mathrm{AB}}^{(\alpha\beta)}|$. The angles $\theta_{\mathrm{AB}}^{(\alpha\beta)}$ and $\kappa_{\mathrm{AB}}^{(\alpha\beta)}$ are depicted in Figure 5. They used $\omega_{\mathrm{AB}}^{(\alpha\beta)}$ in the context of the qualitative interpretation of their experimental results, and they did not apply it to numerical simulations.

[6] In the actual numerical computations, use of an arbitrary value of $\bar{C}_{\mathrm{AB}}^{(\alpha\beta)}$ for the case of $\boldsymbol{s}_I^{(i)} \cdot \boldsymbol{n}_{\mathrm{GB}} = 0$ is sufficient to get the exact solution of the interfacial slip rate.

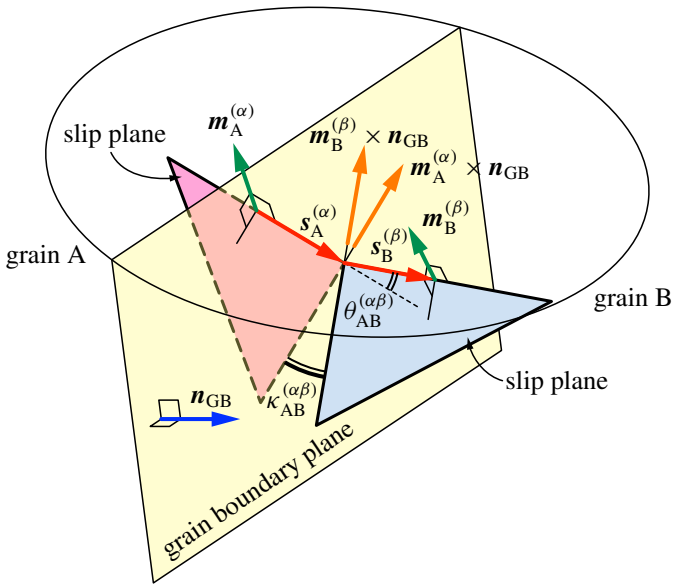

Figure 5. Schematic diagram of the geometrical configuration of the slip systems and the GB plane.

When $\nu = 1$, it is assumed that the amount of the interfacial slip depends linearly on the geometrical configuration of the GB plane and adjacent grains. A value of the exponent ν smaller than unity gives a more active plastic flow at the GB, whereas a large ν suppresses the plastic flow at the boundary. Kheradmand et al. [2016] suggested that transferability of the GB rapidly decreases when the critical condition $\left|\cos\theta_{\mathrm{AB}}^{(\alpha\beta)}\right|\left|\cos\kappa_{\mathrm{AB}}^{(\alpha\beta)}\right| \le \cos 15^\circ \cdot \cos 15^\circ = 0.933$ holds. If we postulate that a hard-type GB is practically represented with $\phi \approx 0.5$, as is expected from the observation in Figure 2 (left), ν is assumed to be ~ 10.

4. Application to a practical problem: bicrystalline micropillar compression

4.1. ***Problem formulation.*** To illustrate the effect of the higher-order boundary conditions in a practical problem of a small sized body, the bicrystalline micropillar compression problem is considered. The finite element model of an f.c.c. bicrystal micropillar with a square cross section is considered, as shown in Figure 6 (left). The aspect ratio of the gauge length H to the edge length W is selected to be 2.3 [Shade et al. 2012; Kuroda 2013]. A plane GB is assumed at $X_1 = 0$ with an initial unit normal of $\boldsymbol{n}_0^{\mathrm{GB}} = (-1, 0, 0)$ in the undeformed configuration. The portion for $X_1 \ge 0$ is assigned as grain A, and that for $X_1 < 0$ is assigned as grain B. Although the specific material and experimental data are not strictly quoted and no parameter fitting study is intended in the present computations, several practical conditions are taken from the study of Imrich et al. [2014] who employed copper single- and bicrystalline micropillars.

Three models of bicrystalline micropillars with different sets of crystal orientations are considered. The first model includes an arbitrary large-angle grain boundary (LAGB), and the other two models have a coherent twin boundary (CTB). In the LAGB micropillar, the [3 1 0] and [1 $\bar{3}$ 26] directions are chosen to be parallel to the sample axis (the X_3-direction) and X_1-direction, respectively, for grain A. The [4 0 $\bar{1}$]

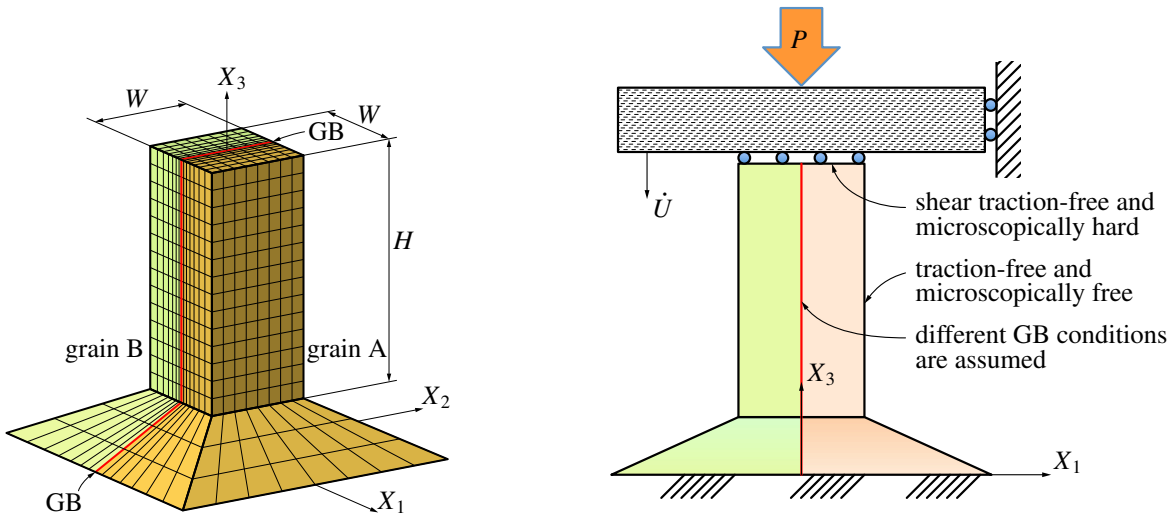

Figure 6. Bicrystalline micropillar compression problem. Finite element model (left); schematic illustration of the boundary conditions (right).

and [3 $\bar{1}$ 12] directions coincide with the X_3- and X_1-directions, respectively, for grain B. The two grains have a difference of 22.8° in orientation around [1 $\bar{3}$ 4]. One of the CTB micropillars, which is designated as CTB-1, has crystal orientations such that the [1 $\bar{1}$ 0] direction is parallel to the X_3-direction and the [1 1 1] direction coincides with the X_1-direction. The crystal orientations of grains A and B are in mirror symmetry about the GB plane, i.e., the orientation of grain A rotated at 180° around the [1 1 1] direction coincides with that of grain B. Each grain has four potentially active slip systems that have the same (highest) Schmid factors = 0.4082 (see [Imrich et al. 2014, Figure 6] for better understanding). Two of these slip systems have the Burgers vectors parallel to the GB plane ($\phi_I^{(i)} = 1$ for the two slip systems). In the other CTB micropillar, which is designated as CTB-2, the crystal orientations considered in CTB-1 are rotated 7.5° about the X_1-axis (counterclockwise rotation in the X_2-X_3 plane). Owing to this tilt, the number of potentially active slip systems is reduced to one in each grain. This unique potentially active slip system has a Schmid factor of 0.4553 and its Burgers vector remains parallel to the GB plane (and also $\phi_I^{(i)} = 1$ for this slip system). All other slip systems have Schmid factors smaller than 0.4. This configuration is rather similar to that of a group of samples employed in [Hirouchi and Shibutani 2014].

The finite strain version of the theory [Kuroda and Tvergaard 2008a] is used. The same theory has already been applied to single-crystal micropillar compression analysis by Kuroda [2013]. The elastic constants are chosen to be $c_{11} = 171$ GPa, $c_{12} = 122$ GPa, and $c_{44} = 69.1$ GPa [Berryman 2005]. The initial slip resistance τ_0 is taken to be 30 MPa for the LAGB micropillar and 50 MPa for the CTB micropillar [Imrich et al. 2014]. The slip hardening modulus h_0 ($= h^{(\alpha\beta)}$) is set to zero for simplicity and also as a reference to the experimental observation of very weak work hardening for single-crystal copper micropillars in [Imrich et al. 2014]. The rate sensitivity parameter m is taken to be 0.05. The length scale l is taken as $l/W = 0.8$.

In the finite element computations, the displacement field is solved using three-dimensional brick-type twenty-node (serendipity) elements with $2 \times 2 \times 2$ Gauss points (i.e., reduced integration) and the GND

density field is solved using three-dimensional brick-type eight-node (bilinear) elements with $2 \times 2 \times 2$ Gauss points (i.e., full integration). The coordinates of the nodes in the eight-node elements are set to be identical to those of the corner nodes in the twenty-node elements.

The axial displacement $\dot{U}$, taken to be positive in the negative X_3-direction, is assigned to the top surface at a nominal strain rate of $\dot{\epsilon}_{\mathrm{N}} = \dot{U}/H = f_{\mathrm{S}}^{(\max)}\dot{\gamma}_0$ with $f_{\mathrm{S}}^{(\max)}$ being the highest absolute values of the nominal Schmid factors among those for all slip systems in the bicrystalline micropillar. A schematic illustration of boundary conditions of the micropillar model is given in Figure 6 (right). A nominal compressive stress is defined as the sum of the nodal forces, P, in the negative X_3-direction, divided by the initial cross-sectional area W^2. Every material point (the nodes in finite element analysis) on the top surface is free to move laterally and will be released from the rigid platen when the normal (contact) stress at that point, which was negative (compressive) at the initial stage of loading, becomes zero. This simply models the case where the friction between the top surface and the loading platen is very low. Regarding the slip rates on the top surface, the microscopically hard condition ($\phi^{(\alpha)} = 0$) is adopted. The contact between the sample top and the loading platen, which are both sufficiently flat, is likely to correspond to this condition. Very few slip lines are often observed on the top surfaces of micropillars after testing (e.g., [Uchic et al. 2004]). This supports the validity of assuming the microscopically hard condition on the top surface. On the traction free surfaces (i.e., on the lateral surface of the gauge region and on the upper surface of the substrate), the microscopically free condition, which corresponds to the null GND condition, is assumed. All the degrees of freedom for displacements on the bottom surface of the substrate are fully constrained, and the microscopically hard condition is assumed on the bottom surface. This setting does not much affect the computational results because essentially the slips are not activated near the bottom surface of the substrate.

Next, we consider the microscopic boundary conditions at the boundary between grains A and B. The following four conditions for the GB are assumed.

Hard GB:	$\phi_I^{(i)} = 0$,
Transparent GB:	$\phi_I^{(i)} = 1$,
Orientation-dependent GB I:	Equations (33) and (34) with $\nu = 1$,
Orientation-dependent GB II:	Equations (33) and (34) with $\nu = 10$.

Although the values of $\bar{C}_{\mathrm{AB}}^{(\alpha\beta)}$ will vary owing to the lattice rotations in each grain under general finite deformations, the updates of $\bar{C}_{\mathrm{AB}}^{(\alpha\beta)}$ are omitted for simplicity and the initial values of $\bar{C}_{\mathrm{AB}}^{(\alpha\beta)}$ are used throughout the computations. This simplification may not significantly affect the results, because the overall nominal compressive strain of the samples will be lower than 10%.

4.2. ***Results.*** The computed curves of nominal compressive stress versus nominal compressive strain for the LAGB, CTB-1, and CTB-2 samples are shown in Figure 7. Computational results using the conventional crystal plasticity model with no account of the size effect [Asaro and Needleman 1985] are also shown in these graphs for comparison. In the case of the hard GB, high strain hardening behavior is observed for all the cases of LAGB, CTB-1, and CTB-2. The significant hardening seen here is solely attributed to the development of the backstresses near the hard GB, around which steep gradients of the slips are generated owing to the constraint on the slips. This typical behavior of the backstresses associated with the accumulation of the GNDs is illustrated in detail in Figures 9 and 10, focusing on

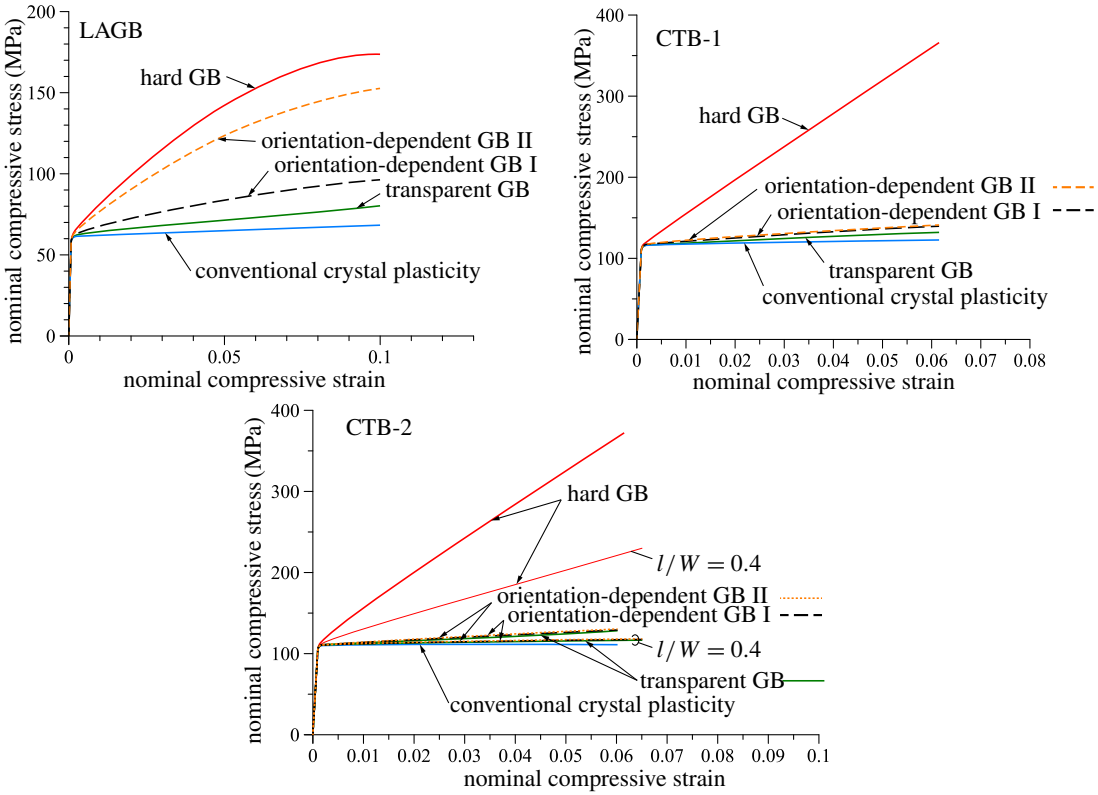

Figure 7. Computed curves of nominal compressive stress versus nominal compressive strain for bicrystalline micropillars with different GB conditions. LAGB samples (left); CTB-1 samples (right); CTB-2 samples (bottom). The length scale is chosen to be $l/W = 0.8$ unless indicated otherwise. In the graphs, "Conventional crystal plasticity" denotes the result obtained using the conventional size-independent crystal plasticity model of Asaro and Needleman [1985]. Orientation-dependent GB II corresponds to $\nu = 10$ and orientation-dependent GB I corresponds to $\nu = 1$.

the results for CTB-2, which has the simplest deformation mechanism and is relevant for understanding the fundamental mechanical behavior.

For LAGB, the computation with the hard GB has predicted high strain hardening behavior, which seems to be consistent with that observed in the experimental stress–strain curve [Imrich et al. 2014]. The orientation-dependent GB II (with $\nu = 10$) also leads to high amounts of strain hardening comparable to that predicted by the hard GB, because the values of $\phi_I^{(i)}$ computed with $\bar{C}_{\mathrm{AB}}^{(\alpha\beta)}$ values of $0 < \bar{C}_{\mathrm{AB}}^{(\alpha\beta)} < 1$ are significantly decreased by the exponent $\nu = 10$. The values of $\phi_I^{(i)}$ for the primary slip systems on the grains A and B sides are respectively 0.360 and 0.525, which give sufficiently hard interface responses as expected from the slip distribution profile shown in Figure 2 (left). The correspondence between the current numerical and the experimental results partly supports the view that LAGB functions as a barrier to dislocations. On the other hand, the orientation-dependent GB I (with $\nu = 1$) and the transparent GB predict a rather low strain hardening behavior.

In the cases of the CTB-1 and CTB-2 samples that have the crystal orientations with the mirror symmetry about the GB plane, the nominal stress-strain curves are nearly linear. The computations with the orientation-dependent GBs (both I and II) exhibit very weak (or almost no) hardening that is consistent with that observed in the experimental stress-strain curves reported in [Imrich et al. 2014] and [Hirouchi and Shibutani 2014]. These curves are close to those for the transparent GB. In the CTB-1 sample, there are four active slip systems in each grain, which have the same highest Schmid factor. Two of these have the Burgers vectors whose directions are parallel to the GB. Even on these slip systems, large amounts of backstresses are produced owing to pileups of screw GNDs when the hard GB is assumed (i.e., a strong slip gradient is produced in the direction perpendicular to the Burgers vector on the slip plane). In the cases of the orientation-dependent GBs (both I and II), these slip systems have $\phi_I^{(i)} = 1$, and thus the GB exhibits no resistance to slips. Such a transparent nature of CTB has already been suggested by Imrich et al. [2014]. The CTB-2 sample explains this condition more clearly due to its simplicity. The CTB-2 sample has only one active slip system whose Burgers vector is parallel to the GB plane in each grain. Hirouchi and Shibutani [2014] conducted compression tests on bicrystalline micropillars having active slip systems nearly parallel to the GB, which are similar to those in the CTB-2 samples. They observed that their stress-strain curves were fundamentally equivalent to those for the single-crystalline samples that showed minimal (almost no) strain hardening. This coincidence supports the view that the CTBs have fundamentally no resistance to slips.

Figure 8 shows the deformations and contours of slips on the primary slip systems whose Burgers vectors are parallel to the GB surface for the CTB-2 samples at a nominal compressive strain of 0.06. The deformation modes predicted with the transparent GB (Figure 8b), the orientation-dependent GB I (Figure 8c) and the orientation-dependent GB II (Figure 8d) are composed of two outer *dead* zones and one distinct central *shear* zone that fully penetrates the body of the pillar. This deformation mode is fairly consistent with the experimental observation by Hirouchi and Shibutani [2014] and it is also similar to that of a single-slip single-crystal micropillar. Comparing the results shown in Figures 8b, 8c, and 8d, the samples with the orientation-dependent GBs (both I and II) exhibited more activated slips on the primary slip systems than the sample with the transparent GB. In these cases, only $\phi_I^{(i)}$ for the slip systems positioned in the cross slip configuration (including the primary slip system) show unity. Smaller values of $\phi_I^{(i)}$ for the other slip systems (including the secondary and tertiary slip systems) indicate the suppression of slip activations at the GB. In the case of the transparent GB, all slip systems have $\phi_I^{(i)} = 1$; thus, the secondary and tertiary slip systems could be activated much more easily than those in the case of the orientation-dependent GBs. Such a distinct appearance of the shear zone may support the properness of the present orientation-dependent GB models. The hard GB does not lead to a visible shear zone and causes less amounts of slip, as shown in Figure 8a. The conventional theory provides no constraint of the slip at every boundary because it has no higher-order microscopic boundary conditions. The conventional theory does not predict the fully penetrating uniform shear zone, but predicts a weakly concentrated and heterogeneous shear area (Figure 8e). Introduction of both the gradient effect and the microscopic boundary conditions is necessary to reproduce the typical deformation mode with the penetrating shear zone, as emphasized by Kuroda [2013].

Figure 9 shows the distributions of the screw GND densities on the primary slip systems in the CTB-2 samples with different GB conditions. In the case of the hard GB (Figure 9 (upper-left)), the screw GNDs significantly accumulate at the GB. In the cases of the transparent GB (Figure 9 (upper-right)),

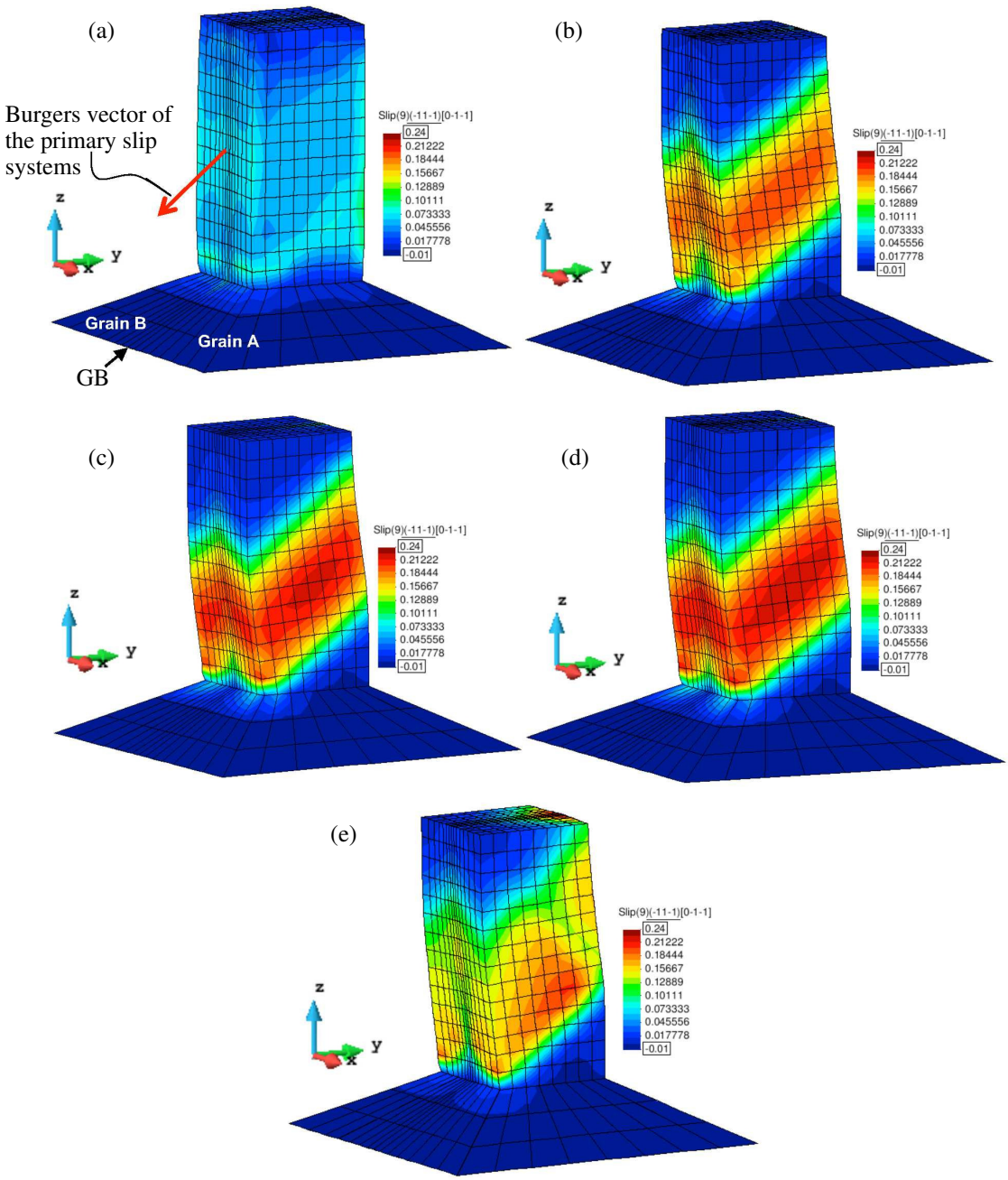

Figure 8. Deformed meshes and contours of slip on the primary slip systems for CBT-2 samples with different GB conditions at a nominal compressive strain of 0.06. The length scale is chosen to be $l/W = 0.8$. The Burgers vectors of the primary slip systems are parallel to the grain boundary. Hard GB (a); transparent GB (b); orientation-dependent GB I ($\nu = 1$) (c); orientation-dependent GB II ($\nu = 10$) (d); conventional size-independent crystal plasticity model (e).

the orientation-dependent GB I (Figure 9 (lower-left)), and the orientation-dependent GB II (Figure 9 (lower-right)), the screw GND densities are much lower than that for the hard GB case. Figure 10 depicts the distributions of the backstresses on the primary slip systems in the CTB-2 samples with different GB conditions. Significant amounts of backstresses were produced at the GB in the case of the hard GB (Figure 10 (upper-left)). The influence of the backstress produced near the GB is observed as apparently strong strain hardening in the stress–strain curves (Figure 7). The backstresses produced in the transparent GB sample (Figure 10 (upper-right)), the orientation-dependent GB I sample (Figure 10 (lower-left)), and the orientation-dependent GB II sample (Figure 10 (lower-right)) are much smaller than that produced in the hard GB samples. Consequently, very small amounts of strain hardening appear in the stress-strain relations and this trend is consistent with experimental observations.

The length scale of $l/W = 0.8$ has been used thus far in the present application shown above. Results for a different value of the length scale, $l/W = 0.4$, are additionally shown in Figure 7 (bottom) for comparison. The nominal stress for the hard GB sample is significantly lowered by the decrease in the length scale. The nominal stresses for the transparent GB sample, the orientation-dependent GB I sample and the orientation-dependent GB II sample become close to that for the conventional plasticity result. But, the overall deformation behaviors of the samples with $l/W = 0.4$ are very similar to those shown in Figures 8–10, although their depictions are omitted.

5. Discussion

5.1. ***On the predictability of the model.*** From the comparison of the present numerical results of the micropillar compression problem with experimental observations in the literature, it can be said that the GB has the transparent nature if the opposite slip systems from the neighboring grains are positioned in the cross slip configuration. The GB models given by (33) with (34), i.e., the orientation-dependent GB I (with $\nu = 1$) and orientation-dependent GB II (with $\nu = 10$) in the application, represent this nature. The experimentally observed mechanical response of the samples with CTB is characterized by these models. The orientation-dependent GB II (with $\nu = 10$) also predicts the experimentally observed material response of the LAGB sample showing the significant amount of strain hardening. This finding partly supports the soundness of the assumption that the amount of slip at the GB nonlinearly depends on the moduli $\bar{C}_{\mathrm{AB}}^{(\alpha\beta)}$. As mentioned in the Introduction, however, opposite observations have been reported [Kunz et al. 2011; Kim et al. 2015], i.e., LAGBs in submicrometer-sized bicrystalline pillars did not act as strong barriers to moving dislocations nor caused additional strain hardening. Such behavior can be apparently described with a low value of ν (e.g., $\nu \approx 1$ or lower), although its physical mechanism is not known at present.

The present model only considers the geometrical configuration of the slip systems and the GB plane. Incorporation of other possible effects, e.g., yielding of the GB at a certain stage of deformation, temperature dependence, and interaction between the GB and the external surface, is left for future studies.

As mentioned in Section 3, in the current model, $\underline{\dot{\gamma}}_{\mathrm{A}}^{(\alpha)}$ at a point on the grain A side of the interface is determined only by the slip rate $\dot{\gamma}_{\mathrm{A}}^{(\alpha)}$ in grain A. A more elaborate formulation of $\underline{\dot{\gamma}}_{\mathrm{A}}^{(\alpha)}$ that also considers the influences of the slip rates $\dot{\gamma}_{\mathrm{B}}^{(\beta)}$ in grain B may be conceived. Such coupling induces a significant complexity in the formulation and also in the computational procedure that demands the use of a kind of *joint element*. This results in a tremendous increase in the size of the system of the equations

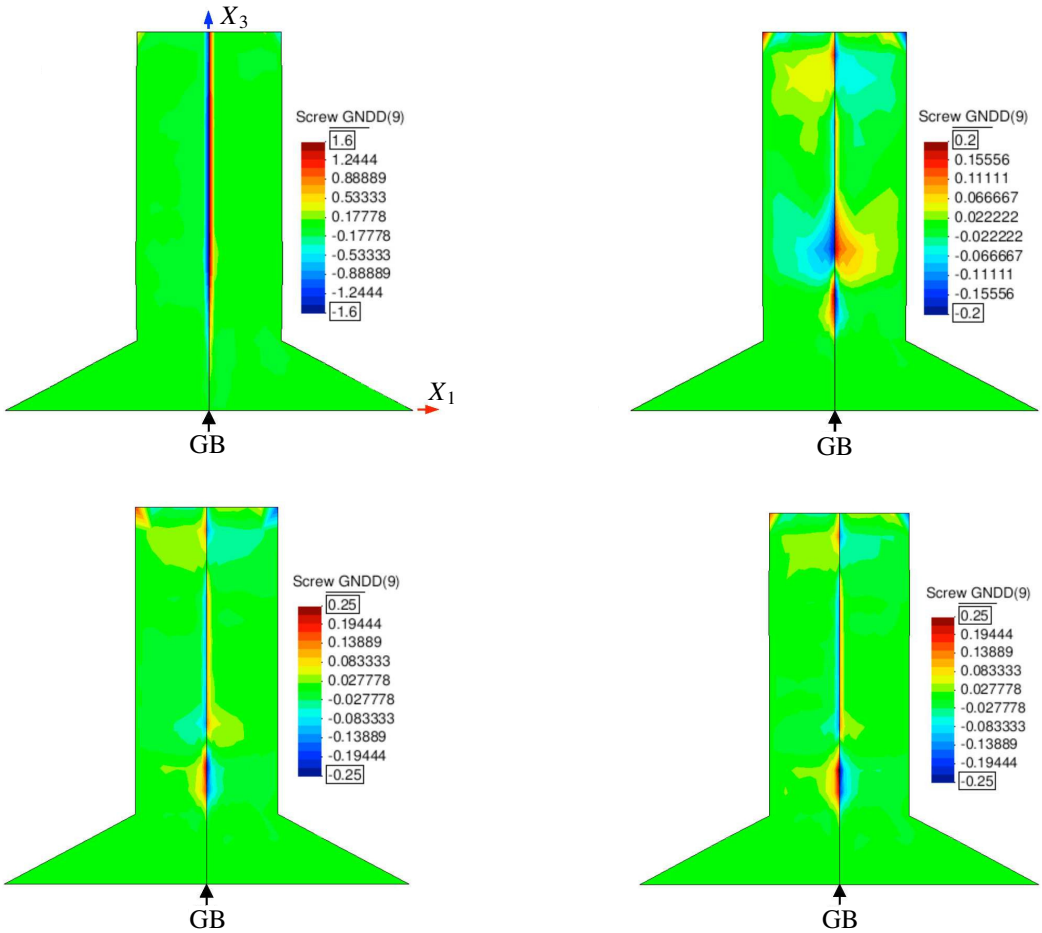

Figure 9. Contours of the screw GND densities (nondimensionalized as $\rho^{(\alpha)}_{\mathrm{G(s)}} bl$) on the primary slip systems in the middle cross section (X_1-X_3 plane views) for CTB-2 samples with different GB conditions at a nominal compressive strain of 0.06. The Burgers vectors of the primary slip systems are parallel to the grain boundary. The length scale is chosen to be $l/W = 0.8$. Hard GB (upper-left); transparent GB (upper-right); orientation-dependent GB I ($\nu = 1$) (lower-left); orientation-dependent GB II ($\nu = 10$) (lower-right).

especially in cases of three-dimensional analysis of a polycrystal. The proposed model with the omission of this coupling is simple. Nevertheless, it has the capability to represent the overall material responses associated with both LAGB and CTB using the same material parameter values.

The present treatment of the microscopic boundary conditions may also efficiently represent peculiar microscopic characteristics of external surfaces. For example, an external surface coated by an incomplete or fragile thin oxide layer that is partially penetrable to dislocations may be modeled by $0 < \phi^{(\alpha)} < 1$ with appropriate constitutive modeling of $\phi^{(\alpha)}$. This is also left for future studies.

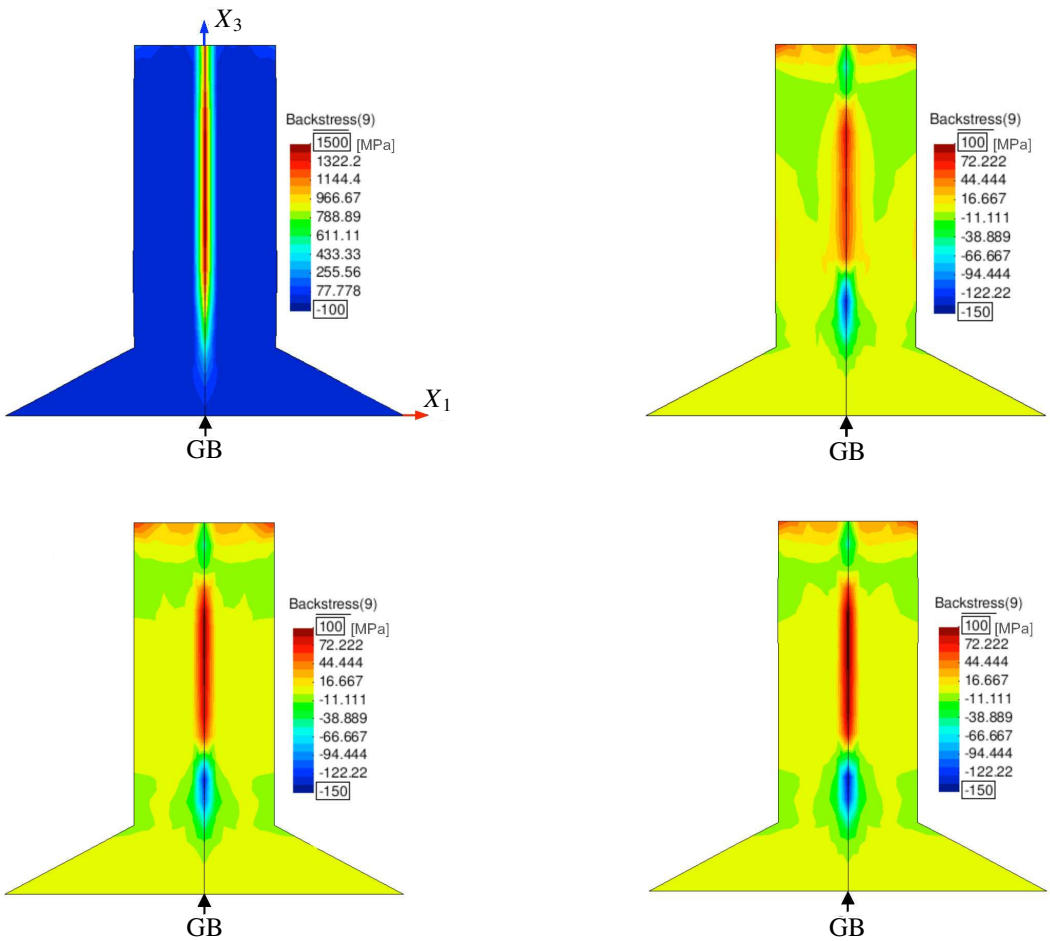

Figure 10. Contours of the backstresses on the primary slip systems in the middle cross section (X_1-X_3 plane views) for CTB-2 samples with different GB conditions at a nominal compressive strain of 0.06. The Burgers vectors of the primary slip systems are parallel to the grain boundary. The length scale is chosen to be $l/W = 0.8$. Hard GB (upper-left); transparent GB (upper-right); orientation-dependent GB I ($\nu = 1$) (lower-left); orientation-dependent GB II ($\nu = 10$) (lower-right).

5.2. ***On the formulation of the model.*** The non-work-conjugate type (or backstress-based) strain gradient plasticity formulation, on which the current theory is based, can be converted to the work-conjugate type representation, as has been discussed by Kuroda and Tvergaard [2006; 2008a; 2008b] and Ertürk et al. [2009]. A virtual work expression that is the basis of the latter type is derived as follows. We use mathematical expressions for the finite strain conditions, referring to [Kuroda and Tvergaard 2008a], but the fundamental points do not differ from those of its small strain version [Kuroda and Tvergaard 2008b]. According to the kinematics of crystal plasticity, the virtual velocity gradient $\tilde{\boldsymbol{L}}$ can be represented by

$$\tilde{\boldsymbol{L}} = \dot{\tilde{\boldsymbol{u}}} \otimes \nabla = \tilde{\boldsymbol{L}}^{\mathrm{e}} + \sum_{\alpha} \dot{\tilde{\gamma}}^{(\alpha)} \bar{\boldsymbol{s}}^{(\alpha)} \otimes \bar{\boldsymbol{m}}^{(\alpha)}, \tag{35}$$

where $\dot{\tilde{\boldsymbol{u}}}$ is a virtual velocity, ∇ is redefined as the spatial gradient operator with respect to the current (deformed) configuration, $\tilde{\boldsymbol{L}}^{\mathrm{e}}$ is a virtual elastic distortion rate, $\dot{\tilde{\gamma}}^{(\alpha)}$ is a virtual slip rate, and $\bar{\boldsymbol{s}}^{(\alpha)}$ and $\bar{\boldsymbol{m}}^{(\alpha)}$ are the slip direction and slip plane normal vectors in the deformed configuration, respectively (a superposed bar denotes that the quantity is evaluated in the deformed configuration). Using the elastic-plastic decomposition of $\tilde{\boldsymbol{L}}$ in (35), the conventional virtual work principle is written as

$$\int_V \left(\boldsymbol{\sigma} : \tilde{\boldsymbol{L}}^{\mathrm{e}} + \sum_\alpha \tau^{(\alpha)} \dot{\tilde{\gamma}}^{(\alpha)} \right) \mathrm{d}V = \int_S \boldsymbol{t} \cdot \dot{\tilde{\boldsymbol{u}}} \, \mathrm{d}S. \tag{36}$$

Here, V and S are respectively the volume and the boundary surface of the body in the deformed configuration.

If the backstress on each slip system can be expressed as the divergence of a vector quantity [7], $\boldsymbol{\xi}^{(\alpha)}$, i.e.,

$$\tau_{\mathrm{b}}^{(\alpha)} = -\nabla \cdot \boldsymbol{\xi}^{(\alpha)}, \tag{37}$$

then we can rewrite the yield condition as

$$\tau^{(\alpha)} + \nabla \cdot \boldsymbol{\xi}^{(\alpha)} = \pi^{(\alpha)} \tag{38}$$

with the definition $\pi^{(\alpha)} = \mathrm{sgn}(\tau^{(\alpha)} + \nabla \cdot \boldsymbol{\xi}^{(\alpha)}) g^{(\alpha)}$, where $g^{(\alpha)}$ is the CRSS of each slip system. Substituting (38) into (36) and applying the divergence theorem and integration by parts, (36) can be further expressed as

$$\int_V \boldsymbol{\sigma} : \tilde{\boldsymbol{L}}^{\mathrm{e}} \, \mathrm{d}V + \sum_\alpha \int_V (\pi^{(\alpha)} \dot{\tilde{\gamma}}^{(\alpha)} + \boldsymbol{\xi}^{(\alpha)} \cdot \nabla \dot{\tilde{\gamma}}^{(\alpha)}) \, \mathrm{d}V = \int_S \boldsymbol{t} \cdot \dot{\tilde{\boldsymbol{u}}} \, \mathrm{d}S + \sum_\alpha \int_S \bar{\boldsymbol{n}} \cdot \boldsymbol{\xi}^{(\alpha)} \dot{\tilde{\gamma}}^{(\alpha)} \, \mathrm{d}S. \tag{39}$$

This equation exactly corresponds to the virtual work principle expression introduced by Gurtin [2002] as the major premise of the theory. In (39), the quantities $\boldsymbol{\xi}^{(\alpha)}$ may be viewed as microscopic stresses that are work-conjugate to the slip rate gradients, and the quantities $\bar{\boldsymbol{n}} \cdot \boldsymbol{\xi}^{(\alpha)}$ appearing on the boundary are considered as *microscopic tractions*.

Next, we consider two pieces of material, grains A and B, as shown in Figure 4 (left), which will form a single body with a GB, as illustrated in Figure 4 (right). The virtual work expression of (39) is applied to each of the grains shown in Figure 4 (left), recognizing the potential GB surfaces $S_{\mathrm{GB(A)}}$ and $S_{\mathrm{GB(B)}}$ with unit normal $\bar{\boldsymbol{n}}_{\mathrm{GB}}$ and $-\bar{\boldsymbol{n}}_{\mathrm{GB}}$, which are respectively expediently distinguished from the outer surfaces S_{A} and S_{B}:

$$\begin{aligned} &\int_{V_{\mathrm{A}}} \boldsymbol{\sigma} : \tilde{\boldsymbol{L}}^{\mathrm{e}} \, \mathrm{d}V + \sum_\alpha \int_{V_{\mathrm{A}}} (\pi^{(\alpha)} \dot{\tilde{\gamma}}^{(\alpha)} + \boldsymbol{\xi}^{(\alpha)} \cdot \nabla \dot{\tilde{\gamma}}^{(\alpha)}) \, \mathrm{d}V \\ &\qquad = \int_{S_{\mathrm{A}}} \boldsymbol{t} \cdot \dot{\tilde{\boldsymbol{u}}} \, \mathrm{d}S + \int_{S_{\mathrm{GB(A)}}} \boldsymbol{t} \cdot \dot{\tilde{\boldsymbol{u}}} \, \mathrm{d}S + \sum_\alpha \left(\int_{S_{\mathrm{A}}} \bar{\boldsymbol{n}} \cdot \boldsymbol{\xi}^{(\alpha)} \dot{\tilde{\gamma}}^{(\alpha)} \, \mathrm{d}S + \int_{S_{\mathrm{GB}(A)}} \bar{\boldsymbol{n}}_{\mathrm{GB}} \cdot \boldsymbol{\xi}^{(\alpha)} \dot{\tilde{\gamma}}^{(\alpha)} \, \mathrm{d}S \right), \end{aligned} \tag{40}$$

[7] If we assume that $\boldsymbol{\xi}^{(\alpha)} = -l^2 b \tau_0 [\bar{\rho}_{\mathrm{G(e)}}^{(\alpha)} \bar{\boldsymbol{s}}^{(\alpha)} + \bar{\rho}_{\mathrm{G(s)}}^{(\alpha)} \bar{\boldsymbol{p}}^{(\alpha)}]$, the backstress relation becomes $\tau_{\mathrm{b}}^{(\alpha)} = l^2 b \tau_0 (\nabla \bar{\rho}_{\mathrm{G(e)}}^{(\alpha)} \cdot \bar{\boldsymbol{s}}^{(\alpha)} + \nabla \bar{\rho}_{\mathrm{G(s)}}^{(\alpha)} \cdot \bar{\boldsymbol{p}}^{(\alpha)} + \bar{\rho}_{\mathrm{G(e)}}^{(\alpha)} \nabla \cdot \bar{\boldsymbol{s}}^{(\alpha)} + \bar{\rho}_{\mathrm{G(s)}}^{(\alpha)} \nabla \cdot \bar{\boldsymbol{p}}^{(\alpha)})$. The last two terms in parentheses on the right-hand side, $\bar{\rho}_{\mathrm{G(e)}}^{(\alpha)} \nabla \cdot \bar{\boldsymbol{s}}^{(\alpha)}$ and $\bar{\rho}_{\mathrm{G(s)}}^{(\alpha)} \nabla \cdot \bar{\boldsymbol{p}}^{(\alpha)}$, were omitted in the numerical computations performed in the present paper. These terms do not have any notable effect when there is only a moderate amount of deformation [Kuroda and Tvergaard 2008a].

$$\int_{V_\mathrm{B}} \boldsymbol{\sigma} : \tilde{\boldsymbol{L}}^\mathrm{e}\,\mathrm{d}V + \sum_\alpha \int_{V_\mathrm{B}} (\pi^{(\alpha)}\dot{\tilde{\gamma}}^{(\alpha)} + \boldsymbol{\xi}^{(\alpha)} \cdot \nabla\dot{\tilde{\gamma}}^{(\alpha)})\,\mathrm{d}V$$
$$= \int_{S_\mathrm{B}} \boldsymbol{t}\cdot\dot{\tilde{\boldsymbol{u}}}\,\mathrm{d}S + \int_{S_{\mathrm{GB(B)}}} \boldsymbol{t}\cdot\dot{\tilde{\boldsymbol{u}}}\,\mathrm{d}S + \sum_\alpha \left(\int_{S_\mathrm{B}} \bar{\boldsymbol{n}}\cdot\boldsymbol{\xi}^{(\alpha)}\dot{\tilde{\gamma}}^{(\alpha)}\,\mathrm{d}S - \int_{S_{\mathrm{GB(B)}}} \bar{\boldsymbol{n}}_\mathrm{GB}\cdot\boldsymbol{\xi}^{(\alpha)}\dot{\tilde{\gamma}}^{(\alpha)}\,\mathrm{d}S \right). \quad (41)$$

Here we assume that no displacement gap (no sliding nor crack opening) at the GB occurs, i.e., $\dot{\tilde{\boldsymbol{u}}}|_\mathrm{A} = \dot{\tilde{\boldsymbol{u}}}|_\mathrm{B}$ and $\boldsymbol{\sigma}|_\mathrm{A}\cdot\bar{\boldsymbol{n}}_\mathrm{GB} - \boldsymbol{\sigma}|_\mathrm{B}\cdot\bar{\boldsymbol{n}}_\mathrm{GB} = \boldsymbol{0}$. Now, we bond grains A and B as depicted in Figure 4 (right), and then consider the addition of (40) and (41),

$$\int_V \boldsymbol{\sigma} : \tilde{\boldsymbol{L}}^\mathrm{e}\,\mathrm{d}V + \sum_\alpha \int_V (\pi^{(\alpha)}\dot{\tilde{\gamma}}^{(\alpha)} + \boldsymbol{\xi}^{(\alpha)}\cdot\nabla\dot{\tilde{\gamma}}^{(\alpha)})\,\mathrm{d}V$$
$$= \int_S \boldsymbol{t}\cdot\dot{\tilde{\boldsymbol{u}}}\,\mathrm{d}S + \sum_\alpha \left(\int_S \bar{\boldsymbol{n}}\cdot\boldsymbol{\xi}^{(\alpha)}\dot{\tilde{\gamma}}^{(\alpha)}\,\mathrm{d}S \right) + \sum_\alpha \left(\int_{S_\mathrm{GB}} \left[(\bar{\boldsymbol{n}}_\mathrm{GB}\cdot\boldsymbol{\xi}^{(\alpha)}\dot{\tilde{\gamma}}^{(\alpha)})|_\mathrm{A} - (\bar{\boldsymbol{n}}_\mathrm{GB}\cdot\boldsymbol{\xi}^{(\alpha)}\dot{\tilde{\gamma}}^{(\alpha)})|_\mathrm{B} \right] \mathrm{d}S \right). \quad (42)$$

According to the expression of (42), we may view the power expenditure at the GB per unit area as

$$\sum_\alpha \{[\![\bar{\boldsymbol{n}}_\mathrm{GB}\cdot\boldsymbol{\xi}^{(\alpha)}\dot{\gamma}^{(\alpha)}]\!]\}, \quad (43)$$

where $[\![\bullet]\!] = (\bullet)|_\mathrm{A} - (\bullet)|_\mathrm{B}$ indicates the jump across S_GB.

Gurtin and Needleman [2005] proposed another expression for the power expenditure at the GB in the small strain context,

$$\sum_\alpha \{[\![\bar{\boldsymbol{n}}_\mathrm{GB}\cdot\boldsymbol{\xi}^{(\alpha)}\dot{\gamma}^{(\alpha)}]\!]\} = \boldsymbol{K} : [\![\dot{\boldsymbol{H}}^\mathrm{p}\cdot(\bar{\boldsymbol{n}}_\mathrm{GB}\times)]\!] \geq 0, \quad (44)$$

where $\boldsymbol{K}$ is an internal force tensor distributed over the GB, which is defined as a power-conjugate to the tensor[8] $[\![\dot{\boldsymbol{H}}^\mathrm{p}\cdot(\bar{\boldsymbol{n}}_\mathrm{GB}\times)]\!]$, where $\dot{\boldsymbol{H}}^\mathrm{p}_I = \sum_\alpha \dot{\gamma}^{(\alpha)}_I \bar{\boldsymbol{s}}^{(\alpha)}_I \otimes \bar{\boldsymbol{m}}^{(\alpha)}_I$ (the subscript I stands for A or B) and the sign of inequality indicates the dissipation condition. In particular, the ideal condition $[\![\dot{\boldsymbol{H}}^\mathrm{p}]\!](\bar{\boldsymbol{n}}_\mathrm{GB}\times) = \boldsymbol{0}$ represents a balanced Burgers vector flow, which means that the flow out of grain A is equal to that into grain B. Gurtin and Needleman [2005] called this the defect-free condition. Okumura et al. [2007] performed finite element analysis of a two-dimensional polycrystal (16 f.c.c. grains) unit cell model with adoption of the defect-free condition at the GBs, and reported that the defect-free condition led to a result rather similar to that predicted with a microfree condition $\bar{\boldsymbol{n}}_\mathrm{GB}\cdot\boldsymbol{\xi}^{(\alpha)}_I = 0$. Later, Gurtin [2008b] proposed another GB model in which constitutive relations are given to the *interfacial microforces*, $\lambda^{(\alpha)}_\mathrm{A} \equiv \bar{\boldsymbol{n}}_\mathrm{GB}\cdot\boldsymbol{\xi}^{(\alpha)}|_\mathrm{A}$ and $\lambda^{(\alpha)}_\mathrm{B} \equiv -\bar{\boldsymbol{n}}_\mathrm{GB}\cdot\boldsymbol{\xi}^{(\alpha)}|_\mathrm{B}$ (that appear in (42) and (43)), via thermodynamic consideration based on the *GB free energy* newly proposed and defined. Computational applications of this GB model have been reported in [Özdemir and Yalçinkaya 2014].

In contrast, in the non-work-conjugate approach on which the current model is based, the weak form of the GND density evolution equation (i.e., (13), (29) and (30)) with the surface integral term gives a deduction of the concomitant boundary conditions. In this context, it is natural to consider directly the boundary conditions for the interfacial slip rate, which can be assumed to represent the resultant effects of absorption, emission, and transmission of the dislocations at the GB.

[8] $(\boldsymbol{a}\times)_{ij} = e_{ikj}a_k$, where $\boldsymbol{a}$ is a vector and e_{ikj} is the permutation symbol.

6. Conclusions

In the present paper, a basic strategy for setting arbitrary interfacial microscopic boundary conditions associated with a backstress-based (non-work-conjugate type) higher-order gradient crystal plasticity theory was proposed. A simple model of the GB behavior was considered, which incorporates a nonlinear dependence of a geometrical correlation between orientations of the slip systems and the GB plane on the amount of slip rate at the GB. The model was examined in analyses of the bicrystalline micropillar compression problem. According to qualitative comparison with the experimental results reported in the literature, the model has the capability to represent the overall material responses associated with both LAGB and CTB using the same material parameter values.

Acknowledgments

This work is partly supported by a JSPS Grant-in-Aid for Scientific Research (B), Grant number KAKENHI 25289001.

References

[Acharya and Bassani 2000] A. Acharya and J. L. Bassani, "Lattice incompatibility and a gradient theory of crystal plasticity", *J. Mech. Phys. Solids* **48**:8 (2000), 1565–1595.

[Aifantis 1984] E. C. Aifantis, "On the microstructural origin of certain inelastic models", *J. Eng. Mater. Tech.* **106**:4 (1984), 326–330.

[Aifantis 1987] E. C. Aifantis, "The physics of plastic deformation", *Int. J. Plasticity* **3**:3 (1987), 211–247.

[Arsenlis and Parks 1999] A. Arsenlis and D. M. Parks, "Crystallographic aspects of geometrically-necessary and statistically-stored dislocation density", *Acta Mater.* **47**:5 (1999), 1597–1611.

[Arsenlis et al. 2004] A. Arsenlis, D. M. Parks, R. Becker, and V. V. Bulatov, "On the evolution of crystallographic dislocation density in non-homogeneously deforming crystals", *J. Mech. Phys. Solids* **52**:6 (2004), 1213–1246.

[Asaro and Needleman 1985] R. J. Asaro and A. Needleman, "Overview no. 42: texture development and strain hardening in rate dependent polycrystals", *Acta Metal.* **33**:6 (1985), 923–953.

[Ashby 1970] M. F. Ashby, "The deformation of plastically non-homogeneous materials", *Philos. Mag.* **21**:170 (1970), 399–424.

[Bacca et al. 2013] M. Bacca, D. Bigoni, F. D. Corso, and D. Veber, "Mindlin second-gradient elastic properties from dilute two-phase Cauchy-elastic composites, part I: Closed form expression for the effective higher-order constitutive tensor", *Int. J. Solids Struct.* **50**:24 (2013), 4010–4019.

[Bardella et al. 2013] L. Bardella, J. Segurado, A. Panteghini, and J. Llorca, "Latent hardening size effect in small-scale plasticity", *Model. Simul. Mater. Sci. Eng.* **21**:5 (2013), 055009.

[Bayerschen et al. 2015] E. Bayerschen, M. Stricker, S. Wulfinghoff, D. Weygand, and T. Böhlke, "Equivalent plastic strain gradient plasticity with grain boundary hardening and comparison to discrete dislocation dynamics", *Proc. R. Soc. A* **471**:2184 (2015), 19.

[Bayley et al. 2006] C. J. Bayley, W. A. M. Brekelmans, and M. G. D. Geers, "A comparison of dislocation induced back stress formulations in strain gradient crystal plasticity: size-dependent mechanics of materials", *Int. J. Solids Struct.* **43**:24 (2006), 7268–7286.

[van Beers et al. 2013] P. R. M. van Beers, G. J. McShane, V. G. Kouznetsova, and M. G. D. Geers, "Grain boundary interface mechanics in strain gradient crystal plasticity", *J. Mech. Phys. Solids* **61**:12 (2013), 2659–2679.

[Berryman 2005] J. G. Berryman, "Bounds and self-consistent estimates for elastic constants of random polycrystals with hexagonal, trigonal, and tetragonal symmetries", *J. Mech. Phys. Solids* **53**:10 (2005), 2141–2173.

[Bittencourt et al. 2003] E. Bittencourt, A. Needleman, M. E. Gurtin, and E. van der Giessen, "A comparison of nonlocal continuum and discrete dislocation plasticity predictions", *J. Mech. Phys. Solids* **51**:2 (2003), 281–310.

[Borg 2007] U. Borg, "A strain gradient crystal plasticity analysis of grain size effects in polycrystals", *Eur. J. Mech. A* **26**:2 (2007), 313–324.

[Clark et al. 1992] W. A. T. Clark, R. H. Wagoner, Z. Y. Shen, T. C. Lee, I. M. Robertson, and H. K. Birnbaum, "On the criteria for slip transmission across interfaces in polycrystals", *Scripta Metall. Mater.* **26**:2 (1992), 203–206.

[Ekh et al. 2011] M. Ekh, S. Bargmann, and M. Grymer, "Influence of grain boundary conditions on modeling of size-dependence in polycrystals", *Acta Mech.* **218**:1 (2011), 103–113.

[El-Naaman et al. 2016] S. A. El-Naaman, K. L. Nielsen, and C. F. Niordson, "On modeling micro-structural evolution using a higher order strain gradient continuum theory", *Int. J. Plasticity* **76** (2016), 285–298.

[Ertürk et al. 2009] İ. Ertürk, J. A. W. van Dommelen, and M. G. D. Geers, "Energetic dislocation interactions and thermodynamical aspects of strain gradient crystal plasticity theories", *J. Mech. Phys. Solids* **57**:11 (2009), 1801–1814.

[Evers et al. 2004] L. P. Evers, W. A. M. Brekelmans, and M. G. D. Geers, "Non-local crystal plasticity model with intrinsic SSD and GND effects", *J. Mech. Phys. Solids* **52**:10 (2004), 2379–2401.

[Fleck et al. 1994] N. A. Fleck, G. M. Muller, M. F. Ashby, and J. W. Hutchinson, "Strain gradient plasticity: theory and experiment", *Acta Metall. Mater.* **42**:2 (1994), 475–487.

[Groma et al. 2003] I. Groma, F. F. Csikor, and M. Zaiser, "Spatial correlations and higher-order gradient terms in a continuum description of dislocation dynamics", *Acta Mater.* **51**:5 (2003), 1271–1281.

[Gurtin 2002] M. E. Gurtin, "A gradient theory of single-crystal viscoplasticity that accounts for geometrically necessary dislocations", *J. Mech. Phys. Solids* **50**:1 (2002), 5–32.

[Gurtin 2008a] M. E. Gurtin, "A finite-deformation, gradient theory of single-crystal plasticity with free energy dependent on densities of geometrically necessary dislocations", *Int. J. Plasticity* **24**:4 (2008), 702–725.

[Gurtin 2008b] M. E. Gurtin, "A theory of grain boundaries that accounts automatically for grain misorientation and grain-boundary orientation", *J. Mech. Phys. Solids* **56**:2 (2008), 640–662.

[Gurtin and Needleman 2005] M. E. Gurtin and A. Needleman, "Boundary conditions in small-deformation, single-crystal plasticity that account for the Burgers vector", *J. Mech. Phys. Solids* **53**:1 (2005), 1–31.

[Gutkin and Aifantis 1999] M. Y. Gutkin and E. C. Aifantis, "Dislocations in the theory of gradient elasticity", *Scripta Mater.* **40**:5 (1999), 559–566.

[Hirouchi and Shibutani 2014] T. Hirouchi and Y. Shibutani, "Mechanical responses of copper bicrystalline micro pillars with $\Sigma 3$ coherent twin boundaries by uniaxial compression tests", *Mater. Trans.* **55**:1 (2014), 52–57.

[Imrich et al. 2014] P. J. Imrich, C. Kirchlechner, C. Motz, and G. Dehm, "Differences in deformation behavior of bicrystalline Cu micropillars containing a twin boundary or a large-angle grain boundary", *Acta Mater.* **73** (2014), 240–250.

[Kheradmand et al. 2016] N. Kheradmand, A. F. Knorr, M. Marx, and Y. Deng, "Microscopic incompatibility controlling plastic deformation of bicrystals", *Acta Mater.* **106** (2016), 219–228.

[Kim et al. 2015] Y. Kim, S. Lee, J. B. Jeon, Y.-J. Kim, B.-J. Lee, S. H. Oh, and S. M. Han, "Effect of a high angle grain boundary on deformation behavior of Al nanopillars", *Scripta Mater.* **107** (2015), 5–9.

[Knorr et al. 2015] A. F. Knorr, M. Marx, and F. Schaefer, "Crack initiation at twin boundaries due to slip system mismatch", *Scripta Mater.* **94** (2015), 48–51.

[Kröner 1963] E. Kröner, "On the physical reality of torque stresses in continuum mechanics", *Int. J. Eng. Sci.* **1**:2 (1963), 261–278.

[Kunz et al. 2011] A. Kunz, S. Pathak, and J. R. Greer, "Size effects in Al nanopillars: single crystalline vs. bicrystalline", *Acta Mater.* **59**:11 (2011), 4416–4424.

[Kuroda 2011] M. Kuroda, "On large-strain finite element solutions of higher-order gradient crystal plasticity", *Int. J. Solids Struct.* **48**:24 (2011), 3382–3394.

[Kuroda 2013] M. Kuroda, "Higher-order gradient effects in micropillar compression", *Acta Mater.* **61**:7 (2013), 2283–2297.

[Kuroda 2015] M. Kuroda, "Strain gradient plasticity: a variety of treatments and related fundamental issues", Chapter 9, pp. 199–218 in *From creep damage mechanics to homogenization methods: a liber amicorum to celebrate the birthday of Nobutada Ohno*, edited by H. Altenbach et al., Advanced Structural Materials **64**, Springer, Cham, 2015.

[Kuroda and Tvergaard 2006] M. Kuroda and V. Tvergaard, "Studies of scale dependent crystal viscoplasticity models", *J. Mech. Phys. Solids* **54**:9 (2006), 1789–1810.

[Kuroda and Tvergaard 2008a] M. Kuroda and V. Tvergaard, "A finite deformation theory of higher-order gradient crystal plasticity", *J. Mech. Phys. Solids* **56**:8 (2008), 2573–2584.

[Kuroda and Tvergaard 2008b] M. Kuroda and V. Tvergaard, "On the formulations of higher-order strain gradient crystal plasticity models", *J. Mech. Phys. Solids* **56**:4 (2008), 1591–1608.

[Levkovitch and Svendsen 2006] V. Levkovitch and B. Svendsen, "On the large-deformation- and continuum-based formulation of models for extended crystal plasticity", *Int. J. Solids Struct.* **43**:24 (2006), 7246–7267.

[Mindlin 1964] R. D. Mindlin, "Micro-structure in linear elasticity", *Arch. Rational Mech. Anal.* **16** (1964), 51–78.

[Ng and Ngan 2009] K. S. Ng and A. H. W. Ngan, "Deformation of micron-sized aluminium bi-crystal pillars", *Philos. Mag.* **89**:33 (2009), 3013–3026.

[Ohashi 2005] T. Ohashi, "Crystal plasticity analysis of dislocation emission from micro voids", *Int. J. Plasticity* **21**:11 (2005), 2071–2088.

[Okumura et al. 2007] D. Okumura, Y. Higashi, K. Sumida, and N. Ohno, "A homogenization theory of strain gradient single crystal plasticity and its finite element discretization", *Int. J. Plasticity* **23**:7 (2007), 1148–1166.

[Özdemir and Yalçinkaya 2014] İ. Özdemir and T. Yalçinkaya, "Modeling of dislocation-grain boundary interactions in a strain gradient crystal plasticity framework", *Comput. Mech.* **54**:2 (2014), 255–268.

[Peirce et al. 1983] D. Peirce, R. J. Asaro, and A. Needleman, "Material rate dependence and localized deformation in crystalline solids", *Acta Metallurgica* **31**:12 (1983), 1951–1976.

[Shade et al. 2012] P. A. Shade, M. D. Uchic, D. M. Dimiduk, G. B. Viswanathan, R. Wheeler, and H. L. Fraser, "Size-affected single-slip behavior of René N5 microcrystals", *Mater. Sci. Eng. A* **535** (2012), 53–61.

[Uchic et al. 2004] M. D. Uchic, D. M. Dimiduk, J. N. Florando, and W. D. Nix, "Sample dimensions influence strength and crystal plasticity", *Science* **305**:5686 (2004), 986–989.

[Wulfinghoff et al. 2013] S. Wulfinghoff, E. Bayerschen, and T. Böhlke, "A gradient plasticity grain boundary yield theory", *Int. J. Plasticity* **51** (2013), 33–46.

[Yamada et al. 1968] Y. Yamada, N. Yoshimura, and T. Sakurai, "Plastic stress-strain matrix and its application for the solution of elastic-plastic problems by the finite element method", *Int. J. Mech. Sci.* **10**:5 (1968), 343–354.

[Yefimov et al. 2004a] S. Yefimov, E. van der Giessen, and I. Groma, "Bending of a single crystal: discrete dislocation and nonlocal crystal plasticity simulations", *Model. Simul. Mater. Sci. Eng.* **12**:6 (2004), 1069.

[Yefimov et al. 2004b] S. Yefimov, I. Groma, and E. van der Giessen, "A comparison of a statistical-mechanics based plasticity model with discrete dislocation plasticity calculations", *J. Mech. Phys. Solids* **52**:2 (2004), 279–300.

Received 20 May 2016. Revised 13 Aug 2016. Accepted 13 Sep 2016.

MITSUTOSHI KURODA: kuroda@yz.yamagata-u.ac.jp
Graduate School of Science and Engineering, Mechanical Systems Engineering, Yamagata University, Jonan 4-3-16, Yonezawa, Yamagata 992-8510, Japan

JOURNAL OF MECHANICS OF MATERIALS AND STRUCTURES
Vol. 12, No. 2, 2017
dx.doi.org/10.2140/jomms.2017.12.219

CONJUGATE STRESS/STRAIN BASE PAIRS FOR PLANAR ANALYSIS OF BIOLOGICAL TISSUES

ALAN D. FREED, VEYSEL EREL AND MICHAEL R. MORENO

A theoretical framework is presented for the analysis of planar membranes based upon a triangular (as opposed to a polar) decomposition of the deformation gradient. This leads to a distillation of the deformation gradient into three distinct modes. Each mode can, in principle, be individually activated in an experiment. Measures of stress are shown to exist for each mode of strain so that the stress power can be decomposed into independent additive parts. The outcome is a set of three conjugate stress/strain base pairs (each being a pair of scalars) from which constitutive equations can be constructed for planar solids without relying on tensor invariants to cast the theory. Explicit and implicit elastic models are derived that, when convolved, produce a material model whose stress/strain response is indicative of soft biological tissues. Stress/strain curves for each conjugate pairing are constructed from published experimental data. The model describes these data.

1. Introduction

Recent advances in regenerative medicine include the ability to tune the mechanical properties of engineered tissue constructs, e.g., [Amensag and McFetridge 2014; Kharaziha et al. 2013; Xie et al. 2015]. With the advent of this capability, the challenges have become these: what mechanical properties have relevance when designing a tissue-engineered construct? What should the target values for these mechanical properties be? Ideally, an engineered tissue graft, say, would possess the same mechanical properties as the native tissue, and integrate seamlessly with respect to mechanical performance. Most efforts to characterize the mechanical properties of tissue-engineered constructs have been based on numerous simplifying assumptions (linear, homogeneous, isotropic) that typically treat the engineered construct as a linear elastic material. These assumptions enable uniaxial mechanical tests to be conducted wherein, e.g., a quasielastic modulus and a tensile strength can be determined. Unfortunately, this form of mechanical characterization is ineffective at providing insight into how well an engineered tissue actually mimics the native tissue *in vivo*. Biological tissues are complex materials that typically undergo large deformations. They also exhibit complex mechanical behaviors that likely include a nonlinear stress/strain curve, mechanical anisotropy, and a viscoelastic response.

The utility of treating an engineered tissue construct as a linear elastic material when establishing mechanical properties is that it enables one-to-one comparisons between materials. A quasimodulus and the tensile strength are physical parameters, each corresponding with a specific measurable physical property; however, the quasimodulus lacks uniqueness. The issue is this: soft tissues are not linear elastic.

Veysel Erel received financial support from the Ministry of National Education, Turkey. Michael R. Moreno received financial support from an NSF GOALI award.
Keywords: thermodynamic conjugate pairs, distortion, Gram–Schmidt decomposition, membrane, soft tissues.

To address this nonlinearity, Fung [1993, §7.12] proposed an exponential strain-energy function of the form

$$W = \tfrac{1}{2}(q + c(\mathrm{e}^{Q} - 1)),$$

whose parameters q and Q are quadratic forms in strain described by

$$q = a_{ijk\ell}E_{ij}E_{k\ell} \quad \text{and} \quad Q = b_{ijk\ell}E_{ij}E_{k\ell},$$

with E_{ij} denoting strain components evaluated in a Lagrangian coordinate frame. There are nine constants to parameterize for the planar case: c, four $a_{ijk\ell}$ and four $b_{ijk\ell}$, because $a_{ijk\ell} = a_{k\ell ij}$ and $b_{ijk\ell} = b_{k\ell ij}$ with $i, j = 1, 2$. Unfortunately, in this framework, there is no analog to an elastic modulus, i.e., there is no parameter that corresponds with some unique, measurable, mechanical property. This system of equations is indeterminable. In practice, data is gathered and a nonlinear least squares fit is used to "solve" the system. Numerous combinations of constants ($a_{ijk\ell}$, $b_{ijk\ell}$, c) usually exist, each representing a reasonable mathematical solution. Even though these parameters have utility in their ability to fit a curve to the data, they (unfortunately) cannot be compared between fits of different materials or samples because the model parameters themselves lack uniqueness and physical interpretation.

This unintended side effect of the Fung approach compromises its utility for the practical purpose of designing engineered tissues with the intent of mimicking Mother Nature. Without unique and physical material parameters, it is difficult to use such an approach for engineering synthesis, which is evident in the apparent absence of models like Fung's in the tissue engineering literature. This fundamental need of the practicing tissue engineer motivated our study.

We seek a material model for planar membranes whose parameters are true material constants in that their values are unique, physical and readily extracted from stress/strain curves. Future work will focus on applying our model to tissue engineering. Here we focus on deriving the model.

The methodology developed herein leads to a material model described by three distinct stress/strain curves. Each unique curve is characterized by three parameters. So our model and Fung's model are both described in terms of nine parameters. The difference being that our model is comprised of three uncoupled responses, a response for each conjugate pairing, with data from each mode having sensitivity to its three independent parameters. Whereas, Fung's model, e.g., is described over the whole of two-space wherein all nine parameters must be fit simultaneously, and getting a data set that is rich enough to secure parameter sensitivity to all of its model parameters is problematic at best. The presumed independence of the thermodynamic conjugate pairs in our approach greatly facilitates parameterization of our model. The theory derived in this paper does not follow a conventional approach, viz., it is not constructed from invariant theory; rather, it is founded upon the following conjecture.

Hypothesis. The governing tensors for stress and the rate of deformation can be encoded into a set of independent conjugate base pairs wherein each stress/strain conjugate pair is a scalar pair. Individual constitutive equations govern the response of each base pair, which may be elastic, viscoelastic, etc., as determined from experiment. After the separate constitutive equations for all base pairs have been solved, their constituents can be decoded to update the tensorial states of stress and the rate of deformation. An admissible encoding/decoding algorithm is one-to-one.

The paper begins with a discussion of kinematics, including a discussion of the difference between three frames of reference that are used: the Lagrangian frame, a material frame, and the Eulerian frame.

In this material frame, work can be decomposed into three parts: dilation, squeeze and shear. From here it is possible to extract three conjugate stress/strain pairs, one describing each deformation mode. They are generalized displacements and tractions in the terminology of Hill [1978]. An encoding/decoding algorithm is put forward that maps tensor components into conjugate base pairs and then back again. The thermodynamic couplings of Kelvin and Poynting are addressed. Explicit and implicit elastic solids are derived for planar membranes that, when convolved, transform into a constitutive theory that is suitable for describing soft biological tissues. The model is demonstrated by fitting it to experimental data taken from the literature.

There are five appendices. The first two compare the polar and triangular decompositions of the deformation gradient for planar deformations. The third addresses acquisition of the components for deformation and stress from planar experiments. The fourth derives stress power in terms of the triangular decomposition. And the fifth decomposes the triangular description for deformation into three distinct modes: dilation, squeeze and shear.

2. Kinematics

A theoretical framework is presented in this document for the analysis of materials that are planar sheets whose utility is expected to reside in engineering design and synthesis. Experiments done on planar membranes have a long history in the biomechanics literature, primarily studied for the purpose of parameterizing material models [Grashow et al. 2006; Humphrey et al. 1987; Lanir and Fung 1974; Sacks 1999; 2000; Sacks and Chuong 1993]. It is assumed that extensions and tractions are determined, to sufficient accuracy, by the deformation of the middle surface of a sheet and, as such, the theory can be cast in $\mathbb{R}^2$. Membrane thickness need not enter into the construction. Influences arising from membrane curvature [Evans and Skalak 1979; Helfrich 1973; Humphrey 1998] are neglected because the radii of curvature are taken to be infinite. For the interested, tension-field theory [Pipkin 1986; Steigmann 1990] should be a viable approach to handle wrinkling, which is not addressed herein.

A material particle of interest is located at position $\boldsymbol{X}$ in a reference state at time t_0 that at current time t is located by a different position vector $\boldsymbol{x}$. The motion of this particle is described by a vector function $\boldsymbol{x} = \boldsymbol{\chi}(\boldsymbol{X}, t)$ that is invertible in the sense that a complementary vector function $\boldsymbol{X} = \overset{-1}{\boldsymbol{\chi}}(\boldsymbol{x}, t)$ exists so that $\boldsymbol{X} = \overset{-1}{\boldsymbol{\chi}}(\boldsymbol{\chi}(\boldsymbol{X}, t), t)$ [Truesdell and Noll 2004]. Motions are considered to be sufficiently smooth so that the required derivatives exist. A particle traverses its path of motion $\boldsymbol{\chi}$ through space with a velocity of $\boldsymbol{v} = \partial\boldsymbol{\chi}(\boldsymbol{X}, t)/\partial t = \dot{\boldsymbol{x}}$.

An areal element $\mathrm{d}A$ of infinitesimal extent within a planar membrane consists of a dense set of point particles filling a connected region in $\mathbb{R}^2$ at time t_0. This same collection of material particles corresponds with another areal element $\mathrm{d}a$ at time t. From the conservation of mass comes $\mathrm{d}m = \rho_0\,\mathrm{d}A = \rho\,\mathrm{d}a$. This areal element has a fixed mass of $\mathrm{d}m$ with planar densities $\rho_0 = \mathrm{d}m/\mathrm{d}A$ and $\rho = \mathrm{d}m/\mathrm{d}a$ at times t_0 and t, and is considered to undergo affine motions.

Deformation at a particle is described by the gradient of its motion $\boldsymbol{\chi}$ taken with respect to its position $\boldsymbol{X}$ that produces a two-point tensor field $\mathbf{F}$ described by

$$\mathbf{F} = \frac{\partial\boldsymbol{\chi}(\boldsymbol{X}, t)}{\partial\boldsymbol{X}}, \quad \text{which is commonly written as} \quad \mathbf{F} = \frac{\partial\boldsymbol{x}}{\partial\boldsymbol{X}}. \tag{1a}$$

Its inverse $\mathbf{F}^{-1}$ exists because the Jacobian of deformation $J := \det \mathbf{F} = \mathrm{d}a/\mathrm{d}A = \rho_0/\rho$ must be positive from the conservation of mass, thereby allowing one to write

$$\mathbf{F}^{-1} = \frac{\partial \overset{-1}{\boldsymbol{\chi}}(\boldsymbol{x}, t)}{\partial \boldsymbol{x}}, \quad \text{which is commonly written as} \quad \mathbf{F}^{-1} = \frac{\partial \boldsymbol{X}}{\partial \boldsymbol{x}}. \tag{1b}$$

The deformation gradient is a linear transformation that maps tangent vectors between the current (Eulerian) and reference (Lagrangian) configurations with a push-forward map of $\mathrm{d}\boldsymbol{x} = \mathbf{F}\,\mathrm{d}\boldsymbol{X}$ and a pull-back map of $\mathrm{d}\boldsymbol{X} = \mathbf{F}^{-1}\mathrm{d}\boldsymbol{x}$. Symmetric and upper-triangular decompositions of the deformation gradient and its inverse are presented in Appendix A and Appendix B for the case of planar membranes.

3. Base vectors

At this point in our development we deviate from the path normally followed by decomposing the deformation gradient $\mathbf{F}$ into a product between an orthogonal rotation $\mathbf{Q}$ and an upper-triangular distortion $\tilde{\mathbf{F}}$, see Appendix B, instead of as a product between another orthogonal tensor $\mathbf{R}$ ($\neq \mathbf{Q}$) and a symmetric stretch $\mathbf{U}$, see Appendix A. Specifically, we adopt a **QR** (Gram–Schmidt) decomposition of $\mathbf{F}$ introduced into the mechanics literature by Srinivasa [2012] who expressed it as $\mathbf{F} = \mathbf{Q}\tilde{\mathbf{F}}$.[1] He explored using this decomposition in lieu of adopting the polar decomposition $\mathbf{F} = \mathbf{RU}$ used throughout mechanics. Rosakis [1990] also derived an upper-triangular decomposition for the deformation gradient by considering materials with a preferred material orientation, his interests being phase transformations and twinning in crystals. He did not use the **QR** matrix decomposition from linear algebra in his kinematic analysis. Freed and Srinivasa [2015] derived the components for $\ln \tilde{\mathbf{F}}$, considering its applicability as a strain measure, and have studied $\tilde{\mathbf{F}}$ for a variety of boundary value problems used in material characterization.

There are three sets of orthogonal base vectors to sort out when using this approach for kinematic analysis, as depicted in Figure 1. They are rectangular Cartesian coordinate frames. There is a natural set of Lagrangian base vectors $\{\mathbf{n}_1, \mathbf{n}_2\}$. The Lagrangian base vectors rotate from an Eulerian frame $\{\mathbf{e}_1, \mathbf{e}_2\}$ via an orthogonal matrix $[\mathbf{R}]$ that comes from the polar decomposition of $\mathbf{F}$, viz., $\mathbf{F} = \mathbf{RU}$. The Eulerian frame is typically considered to be fixed in space, e.g., a coordinate frame in one's laboratory, through which the body translates, rotates and deforms over time. There is also a set of material base vectors $\{\mathbf{m}_1, \mathbf{m}_2\}$ that rotate from the Eulerian frame via an orthogonal matrix $[\mathbf{Q}]$ that comes from the **QR** decomposition of $\mathbf{F}$, viz., $\mathbf{F} = \mathbf{Q}\tilde{\mathbf{F}}$. In the material frame $\{\mathbf{m}_1, \mathbf{m}_2\}$, direction $\mathbf{m}_1$ remains tangent to a physical material line at the coordinate origin [Srinivasa 2012]. Maps between the three sets of base vectors obey

$$\mathbf{m}_\xi = \mathbf{e}_i\, Q^i_\xi, \tag{2a}$$

$$\mathbf{n}_I = \mathbf{e}_i\, R^i_I, \tag{2b}$$

$$\mathbf{n}_I = \mathbf{m}_\xi\, \tilde{R}^\xi_I = \mathbf{m}_\xi [Q^{-1}]^\xi_i\, R^i_I, \tag{2c}$$

and therefore $\tilde{\mathbf{R}} := \mathbf{Q}^{\mathsf{T}}\mathbf{R}$, as drawn in Figure 1. Here lower-case Latin indices associate with the Eulerian frame $\{\mathbf{e}_1, \mathbf{e}_2\}$, upper-case Latin indices associate with the Lagrangian frame $\{\mathbf{n}_1, \mathbf{n}_2\}$, Greek indices

[1] Notation $\mathbf{Q}\tilde{\mathbf{F}}$ is chosen over notation **QR** because $\mathbf{R}$ is commonly used in the polar decomposition of the deformation gradient to denote its rotational component, whereas, in the mathematics literature $\mathbf{R}$ in **QR** denotes a right-triangular matrix that we call distortion. Srinivasa [2012] introduced his notation to avoid potential confusion within the mechanics community.

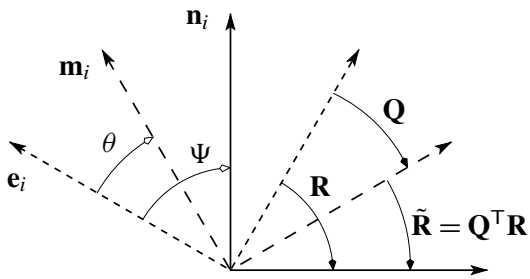

Figure 1. The Lagrangian (natural) base vectors $\mathbf{n}_i$ are located by a rotation $\mathbf{R}$ through an angle ψ measured from an Eulerian coordinate frame with base vectors $\mathbf{e}_i$, therefore $\mathbf{n}_i = \mathbf{e}_i\mathbf{R}$, where $i = 1, 2$. Rotation $\mathbf{R}$ is established through a polar decomposition of the deformation gradient $\mathbf{F} = \mathbf{RU}$. Similarly, the material base vectors $\mathbf{m}_i$ are located by a rotation $\mathbf{Q}$ through an angle θ measured from the Eulerian base vectors $\mathbf{e}_i$, hence $\mathbf{m}_i = \mathbf{e}_i\mathbf{Q}$. Rotation $\mathbf{Q}$ is established through a triangular decomposition of the deformation gradient $\mathbf{F} = \mathbf{Q}\tilde{\mathbf{F}}$. The Lagrangian frame $\{\mathbf{n}_i\}$ rotates relative to the material frame $\{\mathbf{m}_i\}$ through a rotation $\tilde{\mathbf{R}} = \mathbf{Q}^{\mathsf{T}}\mathbf{R}$, i.e., $\mathbf{n}_i = \mathbf{m}_i\tilde{\mathbf{R}}$, with angle $\psi - \theta$. Clockwise rotations are considered to be positive.

associate with the material frame $\{\mathbf{m}_1, \mathbf{m}_2\}$, and repeated indices sum according to Einstein's summation convention.

In many boundary value problems used to characterize materials, the material $\{\mathbf{m}_i\}$ and natural $\{\mathbf{n}_i\}$ frames will be coincident. Pure shear is an example where all three coordinate frames are distinct [Freed and Srinivasa 2015].

To make things more precise, and to shed some light onto the subject, we cast the contravariant vector equation $\mathrm{d}\boldsymbol{x} = \mathbf{F}\,\mathrm{d}\boldsymbol{X}$ into its various component forms. First, consider a polar decomposition of the deformation gradient described by components

$$\mathrm{d}x^i = F^i_I \mathrm{d}X^I = R^i_J U^J_I \mathrm{d}X^I. \tag{3a}$$

Second, consider an upper-triangular decomposition of the deformation gradient described by

$$\mathrm{d}x^i = F^i_I \mathrm{d}X^I = Q^i_\xi \tilde{F}^\xi_I \mathrm{d}X^I. \tag{3b}$$

From these formulæ, it immediately follows that there also exists a displacement vector described by

$$\mathrm{d}\tilde{x}^\xi = \tilde{F}^\xi_I \mathrm{d}X^I = \tilde{R}^\xi_J U^J_I \mathrm{d}X^I \tag{3c}$$

so that

$$\mathrm{d}x^i = Q^i_\xi \mathrm{d}\tilde{x}^\xi, \tag{3d}$$

wherein distortion $\tilde{\mathbf{F}}$ is decomposed into a polar form of $\tilde{\mathbf{F}} = \tilde{\mathbf{R}}\mathbf{U}$ with $\mathrm{d}\tilde{\boldsymbol{x}} = \tilde{\mathbf{F}}\,\mathrm{d}\boldsymbol{X}$. The deformation gradient $\mathbf{F}$ is the same in formulæ (3a) and (3b); however, their decompositions are quite different.

We now relax our notation from that of general tensors to Cartesian tensors without loss of generality. The rotations $\mathbf{R}$ and $\mathbf{Q}$ in (3) are two-state fields, but the states are different between them: rotation $\mathbf{R} = R_{ij}\mathbf{e}_i \otimes \mathbf{n}_j$ vs. rotation $\mathbf{Q} = Q_{ij}\mathbf{e}_i \otimes \mathbf{m}_j$. Stretch is a Lagrangian field in that $\mathbf{U} = U_{ij}\mathbf{n}_i \otimes \mathbf{n}_j$ while distortion is a two-point tensor $\tilde{\mathbf{F}} = \tilde{F}_{ij}\mathbf{m}_i \otimes \mathbf{n}_j$ like the deformation gradient $\mathbf{F} = F_{ij}\mathbf{e}_i \otimes \mathbf{n}_j$. The matrix

representations for rotation $[\mathbf{Q}]$ and distortion $[\tilde{\mathbf{F}}]$ can be obtained in a straightforward manner from both theory and experiment, see Appendix B and Appendix C.

4. Stress power

The rate at which mechanical work is being done on a planar membrane by external tractions (forces per unit reference length), also known as the stress power, is a mechanical property that is independent of the coordinate frame used to quantify it [Hill 1978]. In the material frame $\{\mathbf{m}_i\}$, stress power becomes (see Appendix D for the derivation)

$$\dot{W} = \operatorname{tr}(\tilde{\mathbf{S}}\tilde{\mathbf{L}}) = \tilde{S}_{11}\tilde{L}_{11} + \tilde{S}_{22}\tilde{L}_{22} + \tilde{S}_{12}\tilde{L}_{12}, \tag{4}$$

where the material stress $\tilde{\mathbf{S}} := \mathbf{Q}^{\mathsf{T}}\mathbf{S}\mathbf{Q}$ has symmetric components $\tilde{S}_{ij}$, whereby $\tilde{\mathbf{S}} = \tilde{S}_{ij}\mathbf{m}_i \otimes \mathbf{m}_j$ with $\mathbf{S} = S_{ij}\mathbf{e}_i \otimes \mathbf{e}_j$ being the symmetric Kirchhoff [1852] stress, while the material velocity gradient $\tilde{\mathbf{L}} := \dot{\tilde{\mathbf{F}}}\tilde{\mathbf{F}}^{-1}$ has upper triangular components $\tilde{L}_{ij}$ such that $\tilde{\mathbf{L}} = \tilde{L}_{ij}\mathbf{m}_i \otimes \mathbf{m}_j$.

Substituting the decomposition for $\tilde{\mathbf{L}}$ from (E.3) and (E.4) into formula (4) allows the stress power to be decomposed into three additive components, viz.,

$$\dot{W} = \dot{W}^{\circ} + \dot{W}^{\square} + \dot{W}^{\angle}. \tag{5a}$$

This result is independent of any constitutive assumption to be imposed. The three constituents are:

(1) Stress power resulting from a distortion caused by uniform dilation:

$$\dot{W}^{\circ} := \operatorname{tr}(\tilde{\mathbf{S}}\tilde{\mathbf{L}}^{\circ}) = (\tilde{S}_{11} + \tilde{S}_{22})\,\tfrac{1}{2}(\dot{a}/a + \dot{b}/b). \tag{5b}$$

(2) Stress power resulting from a distortion caused by squeeze:

$$\dot{W}^{\square} := \operatorname{tr}(\tilde{\mathbf{S}}\tilde{\mathbf{L}}^{\square}) = (\tilde{S}_{11} - \tilde{S}_{22})\,\tfrac{1}{2}(\dot{a}/a - \dot{b}/b). \tag{5c}$$

(3) Stress power resulting from a distortion caused by shear:

$$\dot{W}^{\angle} := \operatorname{tr}(\tilde{\mathbf{F}}^{-1}\tilde{\mathbf{S}}\tilde{\mathbf{F}}\tilde{\mathbf{L}}^{\angle}) = (a/b)\tilde{S}_{12}\dot{\gamma}. \tag{5d}$$

An examination of the arguments in the traces of (5) leads one to conclude that there are two stresses to consider. One stress $\tilde{\mathbf{S}}$ for the diagonal contributions, and another stress $\tilde{\mathbf{F}}^{-1}\tilde{\mathbf{S}}\tilde{\mathbf{F}}$ for the off-diagonal contribution. This observation is consistent with Hill's findings [1978].

5. Transformed state: a basis for stress and strain

Classical constructions for describing the constitutive response of a continuum are usually formulated as an application of invariant theory [Rivlin and Smith 1969; Spencer 1972]. Criscione [2003] has argued that although the mathematical theory of invariants is elegant, its utility is flawed because of a covariance that exists between the classic invariants, thereby making parameterization of an ensuing model a daunting task. Addressing this flaw, Criscione et al. [2000; 2003a; 2003b] put forward physically based sets of strain invariants that are orthogonal to one another in the isotropic case, and nearly orthogonal to one another in the anisotropic case. Unfortunately, these strain invariants have been found to be difficult

to work with for experimentalists, and experimentalists are often the ones tasked with parameterizing some specified material model.

Motivated by Criscione's work, yet another approach for constitutive construction is put forward here. It is one possible adaptation of our hypothesis. Although we are of the opinion that there is great promise in our approach, the utility of our construction in engineering practice remains to be assessed by its users over time. Our approach is, we believe, particularly advantageous for experimentalists, see Appendix C.

The methodology put forward is not based upon invariant theory. Instead, linear transformations are introduced that establish a set of conjugate stress/strain basis pairs from which constitutive equations can be formulated in a rigorous way. In other words, we seek a set of generalized displacements q_i and their conjugate tractions p_i so that $\mathrm{d}W = \sum_i p_i \, \mathrm{d}q_i$ provides a coordinate invariant Pfaffian [Hill 1978]. Such a set is not unique, so conjugate pairs ought to be chosen where paired responses are observed to be independent of one another. As with physical laws, their presumed independence cannot be proved theoretically, only disproved experimentally, if at all. If disproved for a certain scenario, that would not necessarily invalidate the utility of a particular conjugate pairing; rather, it would bracket its range of applicability.

An inspection of (4) suggests that one introduce a set of variables expressing the stress power as

$$\mathrm{d}W = \pi \, \mathrm{d}\delta + \sigma \, \mathrm{d}\varepsilon + \tau \, \mathrm{d}\gamma, \tag{6}$$

where $\{\pi, \delta\}$ is a stress/strain conjugate pair of scalars describing uniform dilation, $\{\sigma, \varepsilon\}$ is a stress/strain conjugate pair of scalars describing squeeze, and $\{\tau, \gamma\}$ is a stress/strain conjugate pair of scalars describing shear. In other words, strains δ, ε and γ comprise a set of generalized displacements, viz., $\{\mathbf{q}\} = \{\delta \; \varepsilon \; \gamma\}^{\mathsf{T}}$, while stresses π, σ and τ comprise a set of generalized tractions, viz., $\{\mathbf{p}\} = \{\pi \; \sigma \; \tau\}^{\mathsf{T}}$, such that (6) is a coordinate-invariant description for the work of deformation $\mathrm{d}W$. One admissible encoding/decoding scheme for (6) that is in accordance with our hypothesis is introduced below.

5.1. ***Encoding.*** Inspired by Becker [1893], we consider an encoding of the conjugate tensor fields $\tilde{\mathbf{S}}$ and $\tilde{\mathbf{L}}$ that describes a stress basis with constituents

$$\pi := \tilde{S}_{11} + \tilde{S}_{22}, \tag{7a}$$

$$\sigma := \tilde{S}_{11} - \tilde{S}_{22}, \tag{7b}$$

$$\tau := \frac{a}{b}\tilde{S}_{12}, \tag{7c}$$

whose conjugate strain basis (which have exact differentials for rates) has constituents

$$\delta := \ln\sqrt{ab} \qquad \mathrm{d}\delta = \tfrac{1}{2}(\mathrm{d}a/a + \mathrm{d}b/b), \tag{7d}$$

$$\varepsilon := \ln\sqrt{a/b} \quad \text{with} \quad \mathrm{d}\varepsilon = \tfrac{1}{2}(\mathrm{d}a/a - \mathrm{d}b/b), \tag{7e}$$

$$\gamma \qquad\qquad \mathrm{d}\gamma, \tag{7f}$$

wherein parameters a, b and γ are established from $\mathbf{F}$ via (B.2) or (B.4) for theory, and from Figure 2 and (C.1) for experiment. Each generalized displacement has a rate that is an exact differential. As such, these displacements are two-state fields, independent of the path traversed between states. Consequently, each generalized displacement defined above is a viable measure for strain. This does not, however, imply that $\mathrm{d}W$ is independent of path. As for the conjugate tractions, π is commonly referred to as the

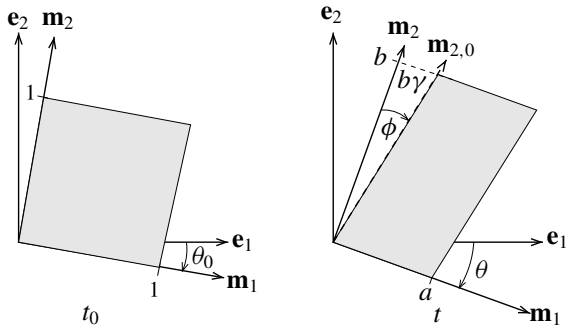

Figure 2. General kinematic analysis for the homogeneous distortion of a unit square into a parallelogram. Extensions a and b and shear $\gamma = \tan\phi$ are the kinematic parameters to be measured. Coordinate directions $\mathbf{e}_1$ and $\mathbf{e}_2$ are orthogonal, as are coordinate directions $\mathbf{m}_1$ and $\mathbf{m}_2$. Angle θ rotates $\{\mathbf{e}_i\}$ into $\{\mathbf{m}_i\}$ and is drawn in its positive sense. Directions $\mathbf{e}_1$ and $\mathbf{e}_2$ are spatial and align with the axes of the load frame. Orthogonal axes $\mathbf{m}_1$ and $\mathbf{m}_2$ can be thought of as being painted onto the material in some reference state t_0 at a angle of θ_0 from the spatial frame $\{\mathbf{e}_i\}$. In a deformed state t, material axis $\mathbf{m}_1$ remains the same, now rotated by an angle of θ from the spatial frame $\{\mathbf{e}_i\}$, however, the material line originally describing the $\mathbf{m}_2$ direction (drawn as $\mathbf{m}_{2,0}$ in the deformed configuration) may no longer be orthogonal to $\mathbf{m}_1$. The angular difference, ϕ, is the angle of shear. Direction $\mathbf{m}_1$ will often be selected to associate with a feature of interest in the sample being tested, e.g., a fiber direction.

surface tension, σ is the first normal stress difference found in the rheology literature [Bird et al. 1987a], and τ is a shear stress normalized by the extent of elongation that is present. Substituting (7) into (5) and rearranging leads to (6). No assumption has been made regarding material constitution. No application of invariant theory has been imposed in this construction.

Evans and Skalak [1979] and Lubarda [2010] considered a multiplicative decomposition for $\mathbf{F}$ of $\mathbf{F} = \mathbf{F}_a\mathbf{F}_d$ wherein $\mathbf{F}_a = \sqrt{\lambda_1\lambda_2}(\mathbf{e}_1 \otimes \mathbf{e}_1 + \mathbf{e}_2 \otimes \mathbf{e}_2)$ and $\mathbf{F}_d = (1/\sqrt{\lambda_1\lambda_2})(\lambda_1\mathbf{e}_1 \otimes \mathbf{n}_1 + \lambda_2\mathbf{e}_2 \otimes \mathbf{n}_2)$, which they call the areal and deviatoric parts of the deformation gradient, respectively, where unit vectors $\mathbf{n}_1$ and $\mathbf{n}_2$ are the eigenvectors of stretch (they are not the Lagrangian base vectors). Our decomposition is similar in purpose to theirs, but distinct in form and physics from theirs.

5.2. ***Decoding.*** For an encoding to be admissible, there must be a unique decoding such that the overall encoding/decoding algorithm is one-to-one. The decoding that associates with the encoding put forward in (7) describes a distortion tensor $\tilde{\mathbf{F}}$ that populates as

$$[\tilde{\mathbf{F}}] = \begin{bmatrix} e^{\delta} & 0 \\ 0 & e^{\delta} \end{bmatrix} \begin{bmatrix} e^{\varepsilon} & 0 \\ 0 & e^{-\varepsilon} \end{bmatrix} \begin{bmatrix} 1 & \gamma \\ 0 & 1 \end{bmatrix} = \begin{bmatrix} e^{\delta+\varepsilon} & e^{\delta+\varepsilon}\gamma \\ 0 & e^{\delta-\varepsilon} \end{bmatrix}, \tag{8a}$$

with an inverse of

$$[\tilde{\mathbf{F}}]^{-1} = \begin{bmatrix} 1 & -\gamma \\ 0 & 1 \end{bmatrix} \begin{bmatrix} e^{-\varepsilon} & 0 \\ 0 & e^{\varepsilon} \end{bmatrix} \begin{bmatrix} e^{-\delta} & 0 \\ 0 & e^{-\delta} \end{bmatrix} = \begin{bmatrix} e^{-\varepsilon-\delta} & -e^{\varepsilon-\delta}\gamma \\ 0 & e^{\varepsilon-\delta} \end{bmatrix}, \tag{8b}$$

whose affiliated material velocity gradient $\tilde{\mathbf{L}}$ populates as

$$[\tilde{\mathbf{L}}] = \begin{bmatrix} \dot{\delta} & 0 \\ 0 & \dot{\delta} \end{bmatrix} + \begin{bmatrix} \dot{\varepsilon} & 0 \\ 0 & -\dot{\varepsilon} \end{bmatrix} + \begin{bmatrix} 0 & \mathrm{e}^{2\varepsilon}\dot{\gamma} \\ 0 & 0 \end{bmatrix} = \begin{bmatrix} \dot{\delta}+\dot{\varepsilon} & \mathrm{e}^{2\varepsilon}\dot{\gamma} \\ 0 & \dot{\delta}-\dot{\varepsilon} \end{bmatrix}. \tag{8c}$$

Because the deformation $\mathbf{F}$ and velocity $\mathbf{L} := \dot{\mathbf{F}}\mathbf{F}^{-1}$ gradients are typically known *a priori*, the material rotation $\mathbf{Q}$ and spin $\boldsymbol{\Xi} := \dot{\mathbf{Q}}\mathbf{Q}^{\mathsf{T}}$ tensors follow immediately via

$$\mathbf{Q} = \mathbf{F}\tilde{\mathbf{F}}^{-1} \quad \text{and} \quad \boldsymbol{\Xi} = \mathbf{W} - \tilde{\mathbf{W}}, \tag{8d}$$

with $\mathbf{W} := \frac{1}{2}(\mathbf{L} - \mathbf{L}^{\mathsf{T}})$ and $\tilde{\mathbf{W}} := \frac{1}{2}\big(\tilde{\mathbf{L}} - \tilde{\mathbf{L}}^{\mathsf{T}}\big)$ being their respective vorticities.

Furthermore, the material stress tensor populates according to a decoding scheme of

$$[\tilde{\mathbf{S}}] = \frac{1}{2}\begin{bmatrix} \pi & 0 \\ 0 & \pi \end{bmatrix} + \frac{1}{2}\begin{bmatrix} \sigma & 0 \\ 0 & -\sigma \end{bmatrix} + \begin{bmatrix} 0 & \mathrm{e}^{-2\varepsilon}\tau \\ \mathrm{e}^{-2\varepsilon}\tau & 0 \end{bmatrix} = \begin{bmatrix} \frac{1}{2}(\pi+\sigma) & \mathrm{e}^{-2\varepsilon}\tau \\ \mathrm{e}^{-2\varepsilon}\tau & \frac{1}{2}(\pi-\sigma) \end{bmatrix}, \tag{9a}$$

where stresses π, σ and τ are usually quantified through constitutive equations, but could also be measured experimentally, see Appendix C. The material stress rate therefore populates as

$$[\dot{\tilde{\mathbf{S}}}] = \begin{bmatrix} \frac{1}{2}(\dot{\pi}+\dot{\sigma}) & \mathrm{e}^{-2\varepsilon}(\dot{\tau} - 2\tau\dot{\varepsilon}) \\ \mathrm{e}^{-2\varepsilon}(\dot{\tau} - 2\tau\dot{\varepsilon}) & \frac{1}{2}(\dot{\pi}-\dot{\sigma}) \end{bmatrix}, \tag{9b}$$

that when rotated into the Eulerian frame becomes

$$\overset{\bullet}{\mathbf{S}} = \mathbf{Q}\dot{\tilde{\mathbf{S}}}\mathbf{Q}^{\mathsf{T}}, \quad \overset{\bullet}{\mathbf{S}} := \frac{\mathrm{d}\mathbf{S}}{\mathrm{d}t} + \mathbf{S}\boldsymbol{\Xi} - \boldsymbol{\Xi}\mathbf{S} \quad \text{where} \quad \mathbf{S} = \mathbf{Q}\tilde{\mathbf{S}}\mathbf{Q}^{\mathsf{T}}, \tag{9c}$$

with $\mathbf{S}$ being the symmetric Kirchhoff [1852] stress, $\mathrm{d}\mathbf{S}/\mathrm{d}t$ being its material derivative, and $\overset{\bullet}{\mathbf{S}}$ describing an objective corotational rate. This objective rate is akin to the polar rate of Green and Naghdi [1965] and Dienes [1979], but with $\mathbf{Q}$ replacing $\mathbf{R}$.

A brief discussion of rate is in order. The question to be answered is this: in what frame does the *material*, not the observer, sense its environment? It is in that frame that the appropriate time derivative to use is the partial derivative. We stipulate that it is within an embedded coordinate frame where this occurs, as developed by Oldroyd [1950] and adopted by his followers, e.g., [Bird et al. 1987a; 1987b; Lodge 1964; 1974]. These constructions employ general tensor fields defined over curvilinear coordinate frames whose coordinate axes are described by the same set of material particles over time. Within the confines of Cartesian tensors, the material frame $\{\mathbf{m}_i\}$ is the closest that one can get to mimicking an embedded curvilinear coordinate frame, because the $\mathbf{m}_1$ coordinate line remains tangent to the 1 material curve, and the 12 coordinate plane with normal $\mathbf{m}_1 \times \mathbf{m}_2$ remains tangent to the 12 material surface [Freed and Srinivasa 2015; Srinivasa 2012]. They are tangents at the origin of coordinate frame $\{\mathbf{m}_1, \mathbf{m}_2, \mathbf{m}_3\}$. It is here where the partial derivative most accurately approximates its actual physical rate, within the confines of employing rectangular Cartesian tensors.

5.3. ***Encoding/decoding maps.*** To show the one-to-one mapping property of this encoding/decoding algorithm, the generalized displacement rates obey the linear mapping

$$\begin{Bmatrix}\dot{q}_1\\ \dot{q}_2\\ \dot{q}_3\end{Bmatrix} := \begin{Bmatrix}\dot{\delta}\\ \dot{\varepsilon}\\ \dot{\gamma}\end{Bmatrix} = \begin{bmatrix}1/2 & 1/2 & 0\\ 1/2 & -1/2 & 0\\ 0 & 0 & \mathrm{e}^{-2\varepsilon}\end{bmatrix}\begin{Bmatrix}\tilde{L}_{11}\\ \tilde{L}_{22}\\ \tilde{L}_{12}\end{Bmatrix}, \tag{10a}$$

while their associated tractions obey the linear mapping

$$\begin{Bmatrix}p_1\\ p_2\\ p_3\end{Bmatrix} := \begin{Bmatrix}\pi\\ \sigma\\ \tau\end{Bmatrix} = \begin{bmatrix}1 & 1 & 0\\ 1 & -1 & 0\\ 0 & 0 & \mathrm{e}^{2\varepsilon}\end{bmatrix}\begin{Bmatrix}\tilde{S}_{11}\\ \tilde{S}_{22}\\ \tilde{S}_{12}\end{Bmatrix}, \tag{10b}$$

which are invertible maps in that

$$\begin{Bmatrix}\tilde{L}_{11}\\ \tilde{L}_{22}\\ \tilde{L}_{12}\end{Bmatrix} = \begin{bmatrix}1 & 1 & 0\\ 1 & -1 & 0\\ 0 & 0 & \mathrm{e}^{2\varepsilon}\end{bmatrix}\begin{Bmatrix}\dot{\delta}\\ \dot{\varepsilon}\\ \dot{\gamma}\end{Bmatrix} \tag{11a}$$

and

$$\begin{Bmatrix}\tilde{S}_{11}\\ \tilde{S}_{22}\\ \tilde{S}_{12}\end{Bmatrix} = \begin{bmatrix}1/2 & 1/2 & 0\\ 1/2 & -1/2 & 0\\ 0 & 0 & \mathrm{e}^{-2\varepsilon}\end{bmatrix}\begin{Bmatrix}\pi\\ \sigma\\ \tau\end{Bmatrix}, \tag{11b}$$

where $\tilde{S}_{21} = \tilde{S}_{12}$. These are maps between continuum mechanics variables and generalized thermodynamic variables. They obey $\dot{W} = \tilde{S}_{11}\tilde{L}_{11} + \tilde{S}_{22}\tilde{L}_{22} + \tilde{S}_{12}\tilde{L}_{12} = \pi\dot{\delta} + \sigma\dot{\varepsilon} + \tau\dot{\gamma}$, as they must. Selecting an encoding/decoding map is key to one's construction of a model that satisfies our hypothesis. It is akin to selecting a set of invariants to use for constitutive construction, but no invariants have been used here.

The encoding/decoding algorithm of (7)–(11) describes an isotropic material response in the sense that an imposed state of uniform stress (i.e., $\pi > 0$, $\sigma = 0$ and $\tau = 0$) will cause a uniform response in strain (viz., $\delta > 0$, $\varepsilon = 0$ and $\gamma = 0$). An encoding/decoding algorithm better suited for describing anisotropic materials, both 2D and 3D, has been developed and will be introduced in a separate paper.

An isotropic membrane whose response is taken to be a function of the symmetric stretch tensor will have two independent modes of deformation: dilation and shear. However, an isotropic membrane whose response is taken to be a function of the triangular distortion tensor will have three independent modes of deformation: dilation, squeeze and shear. This is consistent with Murnaghan's [1954] theoretical finding that a symmetric 2×2 matrix has two invariants, while a triangular 2×2 matrix has three invariants, see Appendix A.1 and Appendix B.2.

6. Constitutive relations

An elastic solid can conduct heat, but does not convert work into heat over a closed cycle. This defines an elastic body [Rajagopal 2011]. The second law of thermodynamics, when describing a reversible process, as interpreted by Carathéodory [1909], implicates that an integrating factor (temperature $T > 0$) exists that transforms the first law of thermodynamics, an *inexact differential equation*, into an *exact differential equation* that becomes $\mathrm{d}S = 1/T\,(\mathrm{d}U - 1/\rho_0\,\mathrm{d}W)$ for a solid continuum [Kestin and Rice 1970]. This is

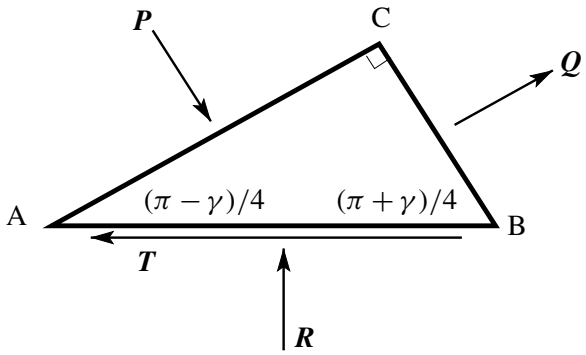

Figure 3. Poynting's [1909] stress analysis of simple shear. Forces $\boldsymbol{P}$ and $\boldsymbol{Q}$ align with the principal axes of stretch, therefore, there are no shears acting on these faces. Their axes are rotated $\gamma/4$ radians from the $\pm 45°$ diagonals, where γ is the extent of shear. Forces $\boldsymbol{R}$ and $\boldsymbol{T}$ are the normal and shear forces acting on the plane of shear. Triangle ABC is a right triangle whose sides have lengths $AB = 2\ell$ and $AC = \sqrt{2}\ell\big(1 + \frac{1}{4}\gamma + \frac{3}{32}\gamma^2\big)$ and $BC = \sqrt{2}\ell\big(1 - \frac{1}{4}\gamma + \frac{3}{32}\gamma^2\big)$. His analysis is accurate to second order.

the second law of thermodynamics governing a reversible process wherein U denotes the internal energy and S denotes the entropy, both per unit mass. Introducing the Legendre transformation $A = U - TS$ allows one to rewrite the second law as $\mathrm{d}T = -1/S(\mathrm{d}A - 1/\rho_0\,\mathrm{d}W)$, where A is the Helmholtz free energy per unit mass, with entropy S now being the integrating factor. Theories for elasticity follow forthwith.

6.1. ***Thermodynamic couplings.*** Two couplings that exist between conjugate pairs in a thermodynamic state are the Kelvin [Thomson 1878] and Poynting [1909] effects. The Kelvin effect is a first-order effect where a change in temperature causes a change in volume. The Poynting effect is a second-order effect where a shear causes a lengthening normal to the shear plane that, if constrained in the sense of a simple shear experiment, will lead to a compressive normal stress. The former effect is well known; the latter effect is less so. They are handled as constitutive characteristics in our approach.

The Kelvin effect is typically modeled in three space as $\Delta V = 3\alpha\Delta T$ where a change in volume ΔV is proportional to a change in temperature ΔT with α being the constant of proportionality, i.e., the coefficient of thermal strain.

Figure 3 presents an overview of Poynting's stress analysis for simple shear. In a change of notation, he considered a second-order response with principle tractions of $\|\boldsymbol{P}\|/AC = G_1\gamma - (\frac{1}{2}G_1 - G_2)\gamma^2$ and $\|\boldsymbol{Q}\|/BC = G_1\gamma + (\frac{1}{2}G_1 - G_2)\gamma^2$. Applying this notation to Poynting's analysis, he determined that the components of traction acting upon the plane of shear are $\|\boldsymbol{T}\|/AB = G_1\gamma$ and $\|\boldsymbol{R}\|/AB = -G_2\gamma^2$ wherein G_1 is the linear shear modulus of Lamé while G_2 is a second-order shear modulus introduced by Poynting. In the material frame $\{\mathbf{m}_i\}$, traction $\|\boldsymbol{T}\|/AB$ equates with $\tilde{S}_{12}$ and traction $\|\boldsymbol{R}\|/AB$ equates with $-\tilde{S}_{22}$, while the stress component $\tilde{S}_{11}$ is zero.

6.2. ***Explicit elasticity.*** A Green [1848] elastic solid assumes that the Helmholtz free energy is a state function whose variation is described by an exact differential in state, namely, temperature and strain

[Ogden 1984]. In terms of the decomposition of work put forward in (6), the second law takes on a form of

$$\rho_0\left(\frac{\partial A}{\partial T}\,\mathrm{d}T+\frac{\partial A}{\partial \delta}\,\mathrm{d}\delta+\frac{\partial A}{\partial \varepsilon}\,\mathrm{d}\varepsilon+\frac{\partial A}{\partial \gamma}\,\mathrm{d}\gamma\right)=-\rho_0 S\,\mathrm{d}T+\pi\,\mathrm{d}\delta+\sigma\,\mathrm{d}\epsilon+\tau\,\mathrm{d}\gamma, \tag{12}$$

which — because the temperature T, strain from dilation δ, strain from squeeze ε, and strain from shear γ can all be varied separately and independently of one another (at least in principle) — requires that the coefficients to differentials $\mathrm{d}T$, $\mathrm{d}\delta$, $\mathrm{d}\varepsilon$ and $\mathrm{d}\gamma$ must each vanish individually, leading to the following set of constitutive formulæ:

$$S=-\frac{\partial A}{\partial T},\quad \pi=\rho_0\frac{\partial A}{\partial \delta},\quad \sigma=\rho_0\frac{\partial A}{\partial \varepsilon},\quad \tau=\rho_0\frac{\partial A}{\partial \gamma}. \tag{13}$$

These constitutive equations govern a planar Green elastic solid within the context of our theoretical approach. Alternatively, Srinivasa [2012] derived a Green elastic solid in terms of the six upper-triangular components of the distortion tensor $\tilde{\mathbf{F}}$ in three-space.

6.2.1. *A Hooke–Kelvin–Poynting solid.* Consider a planar solid whose Helmholtz free-energy function takes on the form of

$$\rho_0 A=-C(T\ln(T/T_0)-(T-T_0))+2K(\delta-\alpha(T-T_0))^2+M\varepsilon^2+\left(\tfrac{1}{2}G_1+G_2(\varepsilon-\delta)\right)\gamma^2, \tag{14}$$

where C is the heat capacity and α is Kelvin's coefficient of thermal strain, both of which reference to some temperature T_0, while K, M and G_1 are akin to the bulk modulus, the P-wave modulus, and the shear modulus from linear elasticity, as they apply to 2-space, with G_2 being Poynting's second-order shear modulus.

Substituting this energy function into our elastic theory (13) produces the set of constitutive formulæ:

$$\rho_0 S=C\ln(T/T_0)+4\alpha K(\delta-\alpha(T-T_0)), \tag{15a}$$

$$\pi=4K(\delta-\alpha(T-T_0))-G_2\gamma^2, \tag{15b}$$

$$\sigma=2M\varepsilon+G_2\gamma^2, \tag{15c}$$

$$\tau=(G_1+2G_2(\varepsilon-\delta))\gamma, \tag{15d}$$

which describe an elastic planar solid in the material frame $\{\mathbf{m}_i\}$ where the deformation gradient is decomposed into an orthogonal rotation matrix and an upper-triangular distortion matrix (see Appendix B). This model accounts for both the Kelvin [Thomson 1878] and Poynting [1909] effects.

Poisson's Ratio: In linear elasticity, the ratio of transverse strain to axial strain caused by an axial traction, when multiplied by minus one to make it positive valued, is a material constant known as Poisson's ratio ν. In nonlinear elasticity, this ratio is a response function, not a material constant. In our analysis, $\ln a$ is the axial strain while $\ln b$ is the transverse strain in a simple extension, see Appendix B. Because stresses π and σ in (9) are equal during such a loading, (15) describes a Poisson's response of

$$\nu:=-\frac{\ln b}{\ln a}\bigg|_{\substack{\tilde{S}_{22}=0\\ \tilde{S}_{12}=0}}\equiv-\frac{\delta-\varepsilon}{\delta+\varepsilon}\bigg|_{\substack{\pi=\sigma\\ \tau=0}}=\frac{2K-M}{2K+M}, \tag{16}$$

so that, e.g., the ratio $\nu = \frac{1}{2}$ whenever $K = \frac{3}{2}M$, the ratio $\nu = \frac{1}{3}$ whenever $K = M$, and the ratio $\nu = 0$ whenever $K = \frac{1}{2}M$. Consequently, both K and M can be parameterized from a single uniaxial experiment, leaving G_1 and G_2 to be parameterized from a shear experiment.

6.2.2. *Solution strategy.* This scheme assumes that one is given a temperature T and a deformation gradient $\mathbf{F}$ and seeks its associated entropy density S and Kirchhoff stress $\mathbf{S}$.

Begin by computing extensions a and b and shear γ from (B.4) and then calculate the trigonometric functions $\cos\theta$ and $\sin\theta$ from (B.5) from which rotation $\mathbf{Q}$ can be established via (B.3a). Now determine the conjugate strains $\{\delta, \varepsilon, \gamma\}$ using the encoding algorithm of (7d)–(7f). Solve the constitutive equations (15) for the entropy S and conjugate stresses $\{\pi, \sigma, \tau\}$. Using these generalized stresses and the imposed squeeze strain ε, populate the material stress $\tilde{\mathbf{S}}$ using the decoding algorithm of (9a), which rotates into the Eulerian Kirchhoff stress $\mathbf{S}$ via $\mathbf{Q}$ according to (9c).

6.3. ***Implicit elasticity.*** An implicit elastic solid assumes that the energy function A depends upon temperature, strain *and* stress [Rajagopal 2003]. It cannot, however, depend upon both temperature and entropy, as it depends upon both strain and stress, because either the temperature T or the entropy S is the integrating factor for the second law, depending upon the thermodynamic potential selected. In terms of the decomposition of work put forward in (6), the second law of thermodynamics takes on a form of

$$\rho_0\left(\frac{\partial A}{\partial T}\,\mathrm{d}T+\frac{\partial A}{\partial \delta}\,\mathrm{d}\delta+\frac{\partial A}{\partial \pi}\,\mathrm{d}\pi+\frac{\partial A}{\partial \varepsilon}\,\mathrm{d}\varepsilon+\frac{\partial A}{\partial \sigma}\,\mathrm{d}\sigma+\frac{\partial A}{\partial \gamma}\,\mathrm{d}\gamma+\frac{\partial A}{\partial \tau}\,\mathrm{d}\tau\right)=-\rho_0 S\,\mathrm{d}T+\pi\,\mathrm{d}\delta+\sigma\,\mathrm{d}\epsilon+\tau\,\mathrm{d}\gamma \quad (17)$$

which — because the temperature T, the dilation response $\{\delta, \pi\}$, the squeeze response $\{\varepsilon, \sigma\}$, and the shear response $\{\gamma, \tau\}$ can all be varied separately and independently of one another (at least in principle) — allows one to separate causalities resulting in the following set of constitutive formulæ:

$$S = -\frac{\partial A}{\partial T}, \quad (18a)$$

$$\pi\,\mathrm{d}\delta = \rho_0\frac{\partial A}{\partial \delta}\,\mathrm{d}\delta + \rho_0\frac{\partial A}{\partial \pi}\,\mathrm{d}\pi, \quad (18b)$$

$$\sigma\,\mathrm{d}\varepsilon = \rho_0\frac{\partial A}{\partial \varepsilon}\,\mathrm{d}\varepsilon + \rho_0\frac{\partial A}{\partial \sigma}\,\mathrm{d}\sigma, \quad (18c)$$

$$\tau\,\mathrm{d}\gamma = \rho_0\frac{\partial A}{\partial \gamma}\,\mathrm{d}\gamma + \rho_0\frac{\partial A}{\partial \tau}\,\mathrm{d}\tau, \quad (18d)$$

where the governing equations for the stress/strain response are now described by an implicit system of ordinary differential equations.

As our interest from this point on resides with modeling soft biological tissues, we forgo addressing the coupling effects of Kelvin [Thomson 1878] and Poynting [1909]. We can safely neglect the Kelvin effect because mammals regulate their temperature. We neglect the Poynting effect as a simplification. How this second-order geometric effect is to be accounted for in a material that itself is highly nonlinear is a subject for future study. Furthermore, there is no experimental data known to us by which one could substantiate such a theory.

6.3.1. *Strain-limiting solid.* Extrapolating the energy function put forward by Freed and Rajagopal [2016] for an isothermal implicit strain-limiting elastic fiber into an energy function that is suitable for a planar

elastic membrane implicates

$$\rho_0 A = 4K\delta - \pi + \beta^\circ \pi\delta + 2M\varepsilon - \sigma + \beta^{\square}\sigma\varepsilon + G\gamma - \tau + \beta^{\angle}\tau\gamma, \tag{19}$$

where K, M and G are moduli describing tangent responses at zero stress and zero strain with β°, $\beta^{\square}$ and $\beta^{\angle}$ relating to their respective states of limiting strain: $\beta^\circ = 1/\delta_{\max}$, $\beta^{\square} = 1/\varepsilon_{\max}$ and $\beta^{\angle} = 1/\gamma_{\max}$. Substituting the energy function in (19) into the constitutive theory of (18) produces an implicit strain-limiting planar elastic solid described by the following system of differential equations:

$$\frac{\mathrm{d}\pi}{\mathrm{d}\delta} = \frac{4K + (\beta^\circ - 1)\pi}{1 - \beta^\circ\delta}, \tag{20a}$$

$$\frac{\mathrm{d}\sigma}{\mathrm{d}\varepsilon} = \frac{2M + (\beta^{\square} - 1)\sigma}{1 - \beta^{\square}\varepsilon}, \tag{20b}$$

$$\frac{\mathrm{d}\tau}{\mathrm{d}\gamma} = \frac{G + (\beta^{\angle} - 1)\tau}{1 - \beta^{\angle}\gamma}, \tag{20c}$$

whose solution, by the separation of variables, describes a dilatoric response of

$$\pi = \frac{4K}{\beta^\circ - 1}\left(\frac{1}{(1 - \beta^\circ\langle\delta\rangle)^{(\beta^\circ - 1)/\beta^\circ}} - 1\right) \quad \beta^\circ > 1, \tag{21a}$$

a squeeze response of

$$\sigma = \operatorname{sgn}(\varepsilon)\frac{2M}{\beta^{\square} - 1}\left(\frac{1}{(1 - \beta^{\square}|\varepsilon|)^{(\beta^{\square} - 1)/\beta^{\square}}} - 1\right) \quad \beta^{\square} > 1, \tag{21b}$$

and a shear response of

$$\tau = \operatorname{sgn}(\gamma)\frac{G}{\beta^{\angle} - 1}\left(\frac{1}{(1 - \beta^{\angle}|\gamma|)^{(\beta^{\angle} - 1)/\beta^{\angle}}} - 1\right) \quad \beta^{\angle} > 1. \tag{21c}$$

These formulæ are written so strain causes stress. They can be written where stress causes strain [Freed and Rajagopal 2016].

Formulæ (21b) and (21c) have been adjusted so that the stresses they produce are odd functions of their respective strains. Both positive and negative squeeze and shear stresses can be supported by membranes, provided that any negative contribution arising from squeeze is offset by a positive dilation. In contrast, only positive dilations can be supported by a membrane. Negative dilations would wrinkle a membrane, which is why the Macaulay bracket $\langle\delta\rangle$ is introduced into formula (21a) with values for $\langle\delta\rangle$ being δ whenever $\delta \geq 0$ and 0 otherwise. This aspect of the model could be made more robust through an application of tension-field theory [Pipkin 1986; Steigmann 1990], but that lies beyond the scope of the present paper.

6.3.2. *Solution strategy.* This scheme assumes that one is given a deformation gradient $\mathbf{F}$ and seeks its associated Kirchhoff stress $\mathbf{S}$. It is possible that a submitted $\mathbf{F}$ can be invalid, so a strategy needs to be constructed to handle inadmissible deformation gradients. A more robust scheme would return strains for supplied stresses, but that strategy does not align as well with finite element formulations.

Begin by computing extensions a and b and shear γ from (B.4) and then calculate the trigonometric functions $\cos\theta$ and $\sin\theta$ from (B.5) from which rotation $\mathbf{Q}$ can be established via (B.3a). Now determine

the conjugate strains $\{\delta, \varepsilon, \gamma\}$ using the encoding algorithm in (7d)–(7f). Test to ensure $0 \le \delta < 1/\beta^\circ$ and $|\varepsilon| < 1/\beta^\square$ and $|\gamma| < 1/\beta^\angle$. If none of these constraints are violated then continue, otherwise the supplied deformation gradient $\mathbf{F}$ is inadmissible and must be handled. Solve the constitutive equations (21) for the conjugate stresses $\{\pi, \sigma, \tau\}$. Using these generalized stresses and the imposed squeeze strain ε, populate the material stress $\tilde{\mathbf{S}}$ using the decoding algorithm in (9a), which rotates into the Eulerian Kirchhoff stress $\mathbf{S}$ via $\mathbf{Q}$ according to (9c).

6.4. ***A model for biological membranes.*** Freed and Rajagopal [2016] modeled collagen fibers as a nonlinear implicit elastic solid intertwined with a linear Hookean solid such that their compliances add, with the outcome being a material response that is characteristic of most soft biologic materials. Here a stress/strain curve starts out with a compliant nonlinear response and finishes up with a stiff linear response. Their fiber model has three material constants whose values are unique, physical and visible within a stress/strain curve, as shown in Figure 4. Their conjecture, applied here to each stress/strain basis pair in $\mathbb{R}^2$, leads to the following set of three constitutive equations: one for the dilatoric response,

$$\delta = \frac{\langle \pi \rangle}{4K^C} + \frac{1}{\beta^\circ}\left(1 - \frac{1}{(1 + (\beta^\circ - 1)\langle \pi \rangle / 4K^E)^{\beta^\circ/(\beta^\circ - 1)}}\right) \quad \beta^\circ > 1, \tag{22a}$$

one for the squeeze response,

$$\varepsilon = \frac{\sigma}{2M^C} + \frac{\operatorname{sgn}(\sigma)}{\beta^\square}\left(1 - \frac{1}{(1 + (\beta^\square - 1)|\sigma|/2M^E)^{\beta^\square/(\beta^\square - 1)}}\right) \quad \beta^\square > 1, \tag{22b}$$

and one for the shear response,

$$\gamma = \frac{\tau}{G^C} + \frac{\operatorname{sgn}(\tau)}{\beta^\angle}\left(1 - \frac{1}{(1 + (\beta^\angle - 1)|\tau|/G^E)^{\beta^\angle/(\beta^\angle - 1)}}\right) \quad \beta^\angle > 1, \tag{22c}$$

which are expressed so that stresses cause strains. Moduli K^C $(> K^E > 0)$ and M^C $(> M^E > 0)$ and G^C $(> G^E > 0)$ are the terminating elastic moduli that describe deformation in their respective linear regions, whereat collagen is the predominant load bearing constituent. Moduli K^E, M^E and G^E are the elastic moduli caused by the restoring forces of elastin that crimp the collagen fibrils in a neighborhood surrounding zero stress and zero strain; while β° $(= 1/\delta^E_{\max})$ and $\beta^\square$ $(= 1/\varepsilon^E_{\max})$ and $\beta^\angle$ $(= 1/\gamma^E_{\max})$ are reciprocal measures for the three limiting states of configuration strain whereat, for soft tissues, the crimp of collagen has been stretched taut. These are illustrated in Figure 4.

6.4.1. *Solution strategy.* This scheme assumes that one is given a deformation gradient $\mathbf{F}$ along with an initial guess for the Kirchhoff stress $\mathbf{S}$ whose actual value is being sought.

Begin by computing extensions a and b and shear γ from (B.4) and then calculate the trigonometric functions $\cos\theta$ and $\sin\theta$ from (B.5) from which rotation $\mathbf{Q}$ can be established via (B.3a). Now determine the assigned conjugate strains $\{\delta, \varepsilon, \gamma\}$ using the encoding algorithm of (7d)–(7f). Rotate the guessed value for Kirchhoff stress $\mathbf{S}$ into the material frame using $\mathbf{Q}$ to get $\tilde{\mathbf{S}}$ according to (9c). Encode the conjugate stresses $\{\pi, \sigma, \tau\}$ using (7a)–(7c) and use these to solve the constitutive equations (22) to get predicted values for the conjugate strains $\{\delta, \varepsilon, \gamma\}$. Use a root finding algorithm to secure a set of conjugate stresses whose associated conjugate strains are in error with the assigned conjugate strains by less than some specified tolerance. Using the converged values for these conjugate stresses and the

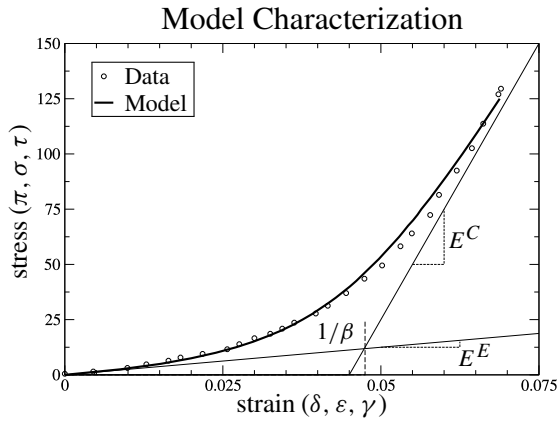

Figure 4. Representative plot depicting the tensile response for the three modes of model (22). Modulus $E^E \in \{K^E, M^E, G^E\}$ describes the low-stress asymptotic behavior where elastin governs the constitutive response, while modulus $E^C \in \{K^C, M^C, G^C\}$ describes the high-stress asymptotic behavior where collagen governs the constitutive response. The intersection of these two asymptotic lines is the reciprocal to parameter $\beta \in \{\beta^\circ, \beta^\square, \beta^\angle\}$ with $1/\beta$ designating the strain where collagen crimp stretches straight.

imposed squeeze strain ε, populate the material stress $\tilde{\mathbf{S}}$ using the decoding algorithm in (9a), which rotates into the Eulerian Kirchhoff stress $\mathbf{S}$ via $\mathbf{Q}$ according to (9c).

7. Experiments

A procedure is outlined in Appendix C for extracting the conjugate stresses π, σ, τ and strains $\delta, \varepsilon, \gamma$ from a planar experiment, along with the angular rotation θ between the material and Eulerian frames.

At present, there is no single experimental data set that we are aware of that would allow one to quantify all three modes of planar deformation introduced in this paper. Consequently, a parameterization of our model (22) using data extracted from a single experiment possessing sensitivity to all model parameters is not currently possible, nor is it for Fung's [1993, p. 304] planar model, in that regard. Both are constitutive equations in nine parameters under isothermal conditions. Plans have been put into motion to address this deficiency from which the data set will be rich enough to provide sensitivity sufficient for quantifying all model parameters. As for now, we are content with demonstrating that our material model (22) is reasonable and worthy of further consideration and scrutiny.

Ideally, one would perform three separate experiments: one for each mode or conjugate pair. One where $\{\pi, \delta\}$ vary and the other fields are held fixed, one where $\{\sigma, \varepsilon\}$ vary and the other fields are held fixed, and one where $\{\tau, \gamma\}$ vary and the other fields are held fixed. Here we analyze published data for dilation and shear, but there is no published data where squeeze is the sole mechanism of deformation. Fortunately, there is data where dilation exists both by itself and in conjunction with squeeze so that the response of both modes can be extracted and studied.

Figure 5 presents data acquired from a double-lap shear test done on porcine myocardium by Dokos et al. [2002, Figure 4], tabulated in [Freed 2014, Table 7.3]. They represent a passive shear response

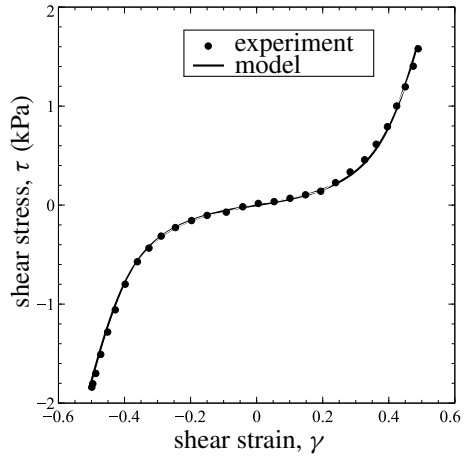

Figure 5. Loading behavior of a porcine myocardium under simple shear. The points represent experimental data. The curve represents the response of model (22c) with $G^C = 15\,\text{kPa}$, $G^E = 0.5\,\text{kPa}$ and $\beta^{\angle} = 2.5$.

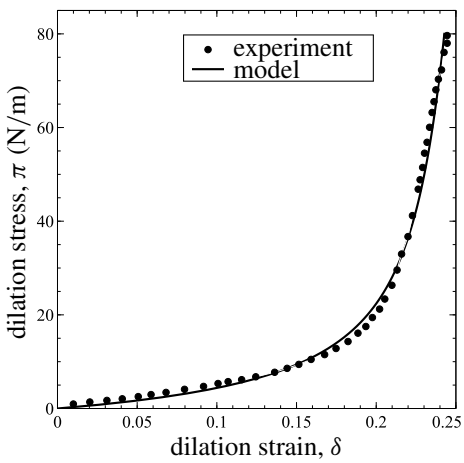

Figure 6. Dilation behavior of a porcine visceral pleural membrane under equibiaxial loading conditions. The points represent experimental data. The curve represents the response of model (22a) with $K^C = 1,875\,\text{N/m}$, $K^E = 7\,\text{N/m}$ and $\beta^{\circ} = 4.1$.

for muscle. Only the loading portion of the curve is shown. Viscoelastic effects will be addressed in a future paper. Our shear model (22c) does an excellent job of describing the nonlinear behavior exhibited by these data.

Figure 6 presents data from an equibiaxial test done on porcine visceral pleura by Freed, Liao and Einstein [2014]. Our dilation model (22a) does a nice job of describing the nonlinear behavior displayed by these data, too.

A planar biaxial loading sequence was imposed on a visceral pleural membrane in the study cited above. Specifically, an equibiaxial 1:1 loading was followed in sequence by two proportional loadings with orthogonal traction ratios of 2:1 and 1:2. Figure 7 presents the squeeze response from these three

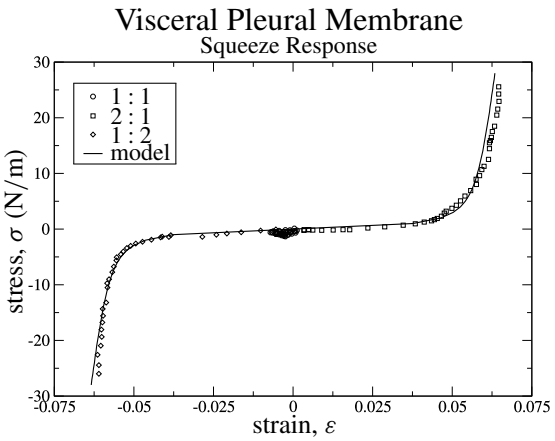

Figure 7. Squeeze behavior of a porcine visceral pleural membrane under three proportional loading conditions. The points represent experimental data. The curve represents the response of model (22b) with $M^C = 2500\,\text{N/m}$, $M^E = 5\,\text{N/m}$ and $\beta^{\square} = 17$.

experiments. The response from the 2:1 traction ratio produced the data in the first quadrant, while the response from the 1:2 traction ratio produced the data in the third quadrant. The equibiaxial experiment produces noise around the origin in the squeeze domain, as it ought; dilation and squeeze are independent deformation modes according to our theory. Our squeeze model (22b) provides a nice description for these data as well.

There is a very large difference in the strain limits for dilation and squeeze in the visceral pleural membrane, viz., $1/\beta^{\circ} = 0.24$ and $1/\beta^{\square} = 0.06$, respectively. This lends further credence to our conjecture that these two modes of deformation are independent of one another.

Equation (16) is applicable for establishing Poisson's ratio in a neighborhood around zero stress, in which case we found $\nu = 0.47$ because $K^E = 7\,\text{N/m}$ and $M^E = 5\,\text{N/m}$. This is consistent with values reported throughout the literature on Poisson's ratio for soft biological tissues.

To further substantiate our methodology, the dilations from these three proportional experiments are shown in Figure 8 along with the model correlation from Figure 6. The response from the 2:1 protocol is in reasonable agreement with the equibiaxial experiment. The 1:2 protocol was the last leg executed in the loading sequence imposed on this sample. Several slip-stick events caused by tissue tearing at suture incision points occurred during the 1:2 loading leg [Freed, Liao and Einstein 2014] and are a likely cause for why their dilation data in Figure 8 are offset from those of the other two protocols. Tearing also had an effect on the squeeze response recorded in Figure 7 causing a small translation of the strain response toward the origin in the third quadrant, but it is less noticeable there.

8. Summary

An elastic theory for planar biological membranes has been derived from thermodynamics and applied to data reported in the literature. The theory is unique in that it is based upon conjugate stress/strain basis pairs, not invariants. These pairs are generalized thermodynamic variables. Constitutive equations were derived for explicit and implicit elastic solids that, when combined, produce a model suitable for soft

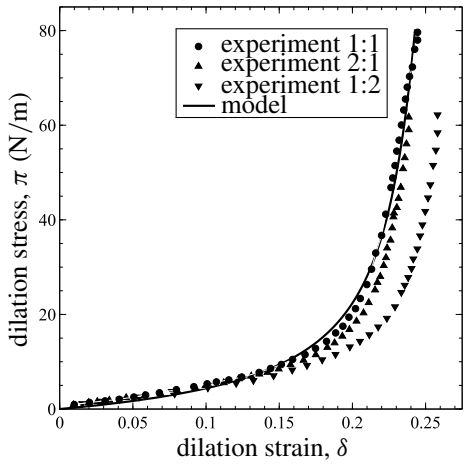

Figure 8. Dilation behavior of a porcine visceral pleural membrane under three proportional loading conditions. The points represent experimental data. The curve represents the model response taken from Figure 6.

tissues. The resulting constitutive formulæ produce a power-law response through the toe and heel regions that culminate with a linear terminal response, indicative of the behavior exhibited by most soft biological tissues whose extracellular matrix consists of collagen fibers intertwined with an elastin network. Data from biaxial experiments done on myocardium and visceral pleura substantiate the model.

Appendix A: Polar decomposition of F

Because $\det \mathbf{F} > 0$ from the conservation of mass, the deformation gradient $\mathbf{F}$ will have a unique matrix decomposition of $[\mathbf{F}] = [\mathbf{R}][\mathbf{U}]$ where matrix $[\mathbf{R}]$ has orthonormal columns and matrix $[\mathbf{U}]$ is symmetric with positive eigenvalues [Noll 1955].

Quantifying a polar decomposition of the deformation gradient, i.e., $\mathbf{F} = \mathbf{RU}$, see [Simo and Hughes 1998], begins with computing the eigenvalues for stretch via

$$\lambda_1 = \sqrt{\tfrac{1}{2}\big((C_{11}+C_{22}) + \sqrt{(C_{11}+C_{22})^2 - 4(C_{11}C_{22}-C_{12}^2)}\big)}, \tag{A.1a}$$

$$\lambda_2 = \sqrt{\tfrac{1}{2}\big((C_{11}+C_{22}) - \sqrt{(C_{11}+C_{22})^2 - 4(C_{11}C_{22}-C_{12}^2)}\big)}, \tag{A.1b}$$

where the symmetric Cauchy deformation tensor $\mathbf{C} = \mathbf{F}^{\mathsf{T}}\mathbf{F}$ has components $\mathbf{C} = C_{ij}\mathbf{n}_i \otimes \mathbf{n}_j$ evaluated in the Lagrangian frame $\{\mathbf{n}_1, \mathbf{n}_2\}$. Knowing the principal stretches, one can populate the matrices for the Lagrangian stretch $[\mathbf{U}]$ and its inverse $[\mathbf{U}]^{-1}$ via the formulæ [Ting 1985]:

$$[\mathbf{U}] = \frac{1}{I}(II[\mathbf{I}] + [\mathbf{C}]), \tag{A.2a}$$

$$[\mathbf{U}]^{-1} = \frac{1}{I\,II}((I^2 - II)[\mathbf{I}] - [\mathbf{C}]), \tag{A.2b}$$

where the two invariants I and II of stretch are described by

$$I = \lambda_1 + \lambda_2 \quad \text{and} \quad II = \lambda_1 \lambda_2. \tag{A.3}$$

The rotation matrix $[\mathbf{R}]$ determined from $[\mathbf{R}] = [\mathbf{F}][\mathbf{U}]^{-1}$ becomes

$$[\mathbf{R}] = \begin{bmatrix} \cos\psi & \sin\psi \\ -\sin\psi & \cos\psi \end{bmatrix}, \tag{A.4a}$$

wherein, from (A.1)–(A.3),

$$\psi = \begin{cases} \sin^{-1}\big([(I^2 - II - C_{22})F_{12} - C_{12}F_{11}]/(I\ II)\big), \\ \sin^{-1}\big([(C_{11} - I^2 + II)F_{21} + C_{12}F_{22}]/(I\ II)\big), \end{cases} \tag{A.4b}$$

where ψ is a rotation angle that orients the natural frame $\{\mathbf{n}_i\}$ relative to the Eulerian frame $\{\mathbf{e}_i\}$, as drawn in Figure 1, and is positive for clockwise rotations and negative for counterclockwise rotations.

A.1. ***Invariants.*** A symmetric 2×2 matrix, say $[\mathbf{A}]$, with elements

$$[\mathbf{A}] = \begin{bmatrix} a & c \\ c & b \end{bmatrix} \tag{A.5a}$$

in some coordinate frame $\{\mathbf{e}_1, \mathbf{e}_2\}$, rotates via some orthogonal matrix $[\mathbf{R}]$ into another coordinate frame $\{\hat{\mathbf{e}}_1, \hat{\mathbf{e}}_2\}$ where $\hat{\mathbf{e}}_i = \mathbf{e}_i\mathbf{R}$ with the matrix mapping as $[\hat{\mathbf{A}}] = [\mathbf{R}]^{\mathsf{T}}[\mathbf{A}][\mathbf{R}]$. A function of matrix $[\mathbf{A}]$, say $f(\mathbf{A})$, is invariant under arbitrary rotations provided that

$$f(\mathbf{A}) = f(\hat{\mathbf{A}}) = f(\mathbf{R}^{\mathsf{T}}\mathbf{A}\mathbf{R}). \tag{A.5b}$$

It is well known that the trace and determinant obey this condition, resulting in the two invariants

$$I_1 = a + b \quad \text{and} \quad I_2 = ab - c^2, \tag{A.5c}$$

wherein $I_1 := \operatorname{tr}(\mathbf{R}^{\mathsf{T}}\mathbf{A}\mathbf{R}) = \operatorname{tr}(\mathbf{R}\mathbf{R}^{\mathsf{T}}\mathbf{A}) = \operatorname{tr}(\mathbf{A})$ and $I_2 := \det(\mathbf{R}^{\mathsf{T}}\mathbf{A}\mathbf{R}) = \det(\mathbf{R}^{\mathsf{T}})\det(\mathbf{A})\det(\mathbf{R}) = \det(\mathbf{A})$ and therefore $\operatorname{tr}(\mathbf{A}^2) = I_1^2 - 2I_2$. In the case of stretch, (A.3) and (A.5c) are equivalent, with (A.3) being described in principal (spectral) coordinates.

Appendix B: QR decomposition of F

Because $\det\mathbf{F} > 0$ from the conservation of mass, the deformation gradient $\mathbf{F}$ will have another unique matrix decomposition of $[\mathbf{F}] = [\mathbf{Q}][\tilde{\mathbf{F}}]$ where matrix $[\mathbf{Q}]$ has orthonormal columns (distinct from $[\mathbf{R}]$) and matrix $[\tilde{\mathbf{F}}]$ is upper triangular with positive diagonal elements [Stewart 1973].

Quantifying a **QR** decomposition of the deformation gradient, i.e., $[\mathbf{F}] = [\mathbf{Q}][\tilde{\mathbf{F}}]$, leads to a distortion $[\tilde{\mathbf{F}}]$ and its inverse $[\tilde{\mathbf{F}}]^{-1}$ that populate via [Freed and Srinivasa 2015]

$$[\tilde{\mathbf{F}}] = \begin{bmatrix} a & a\gamma \\ 0 & b \end{bmatrix} \quad \text{and} \quad [\tilde{\mathbf{F}}]^{-1} = \begin{bmatrix} 1/a & -\gamma/b \\ 0 & 1/b \end{bmatrix}, \tag{B.1}$$

whose constituents are established through a Cholesky factorization of $\mathbf{C} = \mathbf{F}^{\mathsf{T}}\mathbf{F} = \tilde{\mathbf{F}}^{\mathsf{T}}\tilde{\mathbf{F}}$ leading to [Srinivasa 2012]

$$a = \sqrt{C_{11}}, \quad \gamma = C_{12}/C_{11}, \quad b = \sqrt{C_{22} - C_{12}^2/C_{11}}, \tag{B.2}$$

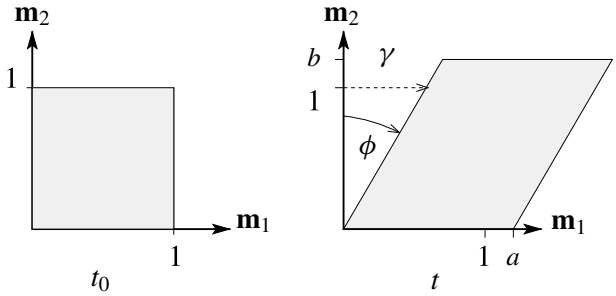

Figure 9. The homogeneous distortion of a unit square into a parallelogram. Extensions a and b and shear $\gamma = \tan\phi$ are the kinematic parameters to be measured in a planar experiment to quantify distortion $\tilde{\mathbf{F}}$ via (B.1) in the $\{\mathbf{m}_i\}$ coordinate frame.

where parameters a, b and γ are physical quantities that can be extracted from experiment (see Appendix C). Measurements are to be made in accordance with Figure 9. Parameter a is the extension ratio in the $\mathbf{m}_1$ direction, viz., $a = \ell_1(t)/\ell_1(t_0)$. Parameter b is the extension ratio in the $\mathbf{m}_2$ direction, viz., $b = \ell_2(t)/\ell_2(t_0)$. Parameter γ measures the extent that a material line originally aligned with the $\mathbf{m}_2$ direction rotates in the $\mathbf{m}_1$ direction — an extent described by $\gamma = \tan\phi$, wherein ϕ is the shear angle. Extensions a and b and stretches λ_1 and λ_2 are coincident only in the absence of shear γ, otherwise they are distinct quantities. Rosakis [1990, Lemma 5.1] has proven that $\lambda_1 \geq a \geq \lambda_2$, where λ_1 and λ_2 are the eigenvalues of stretch given in (A.1).

The rotational contribution $[\mathbf{Q}]$ arising from an upper-triangular decomposition of the deformation gradient is determined from $[\mathbf{Q}] = [\mathbf{F}][\tilde{\mathbf{F}}]^{-1}$ and (B.1) and (B.2) leading to

$$[\mathbf{Q}] = \begin{bmatrix} \cos\theta & \sin\theta \\ -\sin\theta & \cos\theta \end{bmatrix}, \tag{B.3a}$$

wherein

$$\theta = \begin{cases} -\sin^{-1}(F_{21}/a), \\ \sin^{-1}\big((F_{12} - \gamma F_{11})/b\big), \end{cases} \tag{B.3b}$$

with θ being the angle that the material frame $\{\mathbf{m}_i\}$ rotates relative to the Eulerian frame $\{\mathbf{e}_i\}$ with positive rotations occurring in a clockwise sense, see, Figure 1.

Recall that the angle of rotation of the Lagrangian frame $\{\mathbf{n}_i\}$ relative to the Eulerian frame $\{\mathbf{e}_i\}$ is ψ, see (A.4). Consequently, angle $\psi - \theta$ establishes the angle of rotation of the Lagrangian frame $\{\mathbf{n}_i\}$ about the material frame $\{\mathbf{m}_i\}$, see, Figure 1.

B.1. ***Derived from the deformation gradient.*** Alternatively, one can use the components of the deformation gradient $[\mathbf{F}]$ to directly quantify extensions a and b and shear γ, the building blocks of distortion $[\tilde{\mathbf{F}}]$, plus the angle θ that determines rotation $[\mathbf{Q}]$ between the Eulerian $\{\mathbf{e}_i\}$ and material $\{\mathbf{m}_i\}$ coordinate frames via

$$a = \sqrt{F_{11}^2 + F_{21}^2}, \quad \gamma = \frac{F_{11}F_{12} + F_{21}F_{22}}{F_{11}^2 + F_{21}^2}, \quad b = \frac{F_{11}F_{22} - F_{12}F_{21}}{\sqrt{F_{11}^2 + F_{21}^2}}, \tag{B.4}$$

with

$$\sin\theta = \frac{-F_{21}}{\sqrt{F_{11}^2 + F_{21}^2}} \quad \text{and} \quad \cos\theta = \frac{F_{11}}{\sqrt{F_{11}^2 + F_{21}^2}}, \tag{B.5}$$

thereby foregoing any need to construct the Cauchy deformation tensor $\mathbf{C}$.

B.2. ***Invariants.*** An upper-triangular 2×2 matrix, say $[\mathbf{A}]$, with elements

$$[\mathbf{A}] = \begin{bmatrix} a & c \\ 0 & b \end{bmatrix} \tag{B.6}$$

has three unitary invariants [Murnaghan 1954]:

$$\bar{I}_1 = \text{tr}(\mathbf{A}) = a + b, \quad \bar{I}_2 = \text{tr}(\mathbf{A}^2) = a^2 + b^2, \quad \bar{I}_3 = \text{tr}(\mathbf{A}^\mathsf{T}\mathbf{A}) = a^2 + b^2 + c^2, \tag{B.7}$$

where $\bar{I}_1$, $\bar{I}_2$ and $\bar{I}_3$ are invariant of coordinate rotations because $\text{tr}(\mathbf{R}^\mathsf{T}\mathbf{A}\mathbf{R}) = \text{tr}(\mathbf{R}\mathbf{R}^\mathsf{T}\mathbf{A}) = \text{tr}(\mathbf{A}) = \bar{I}_1$ and $\text{tr}((\mathbf{R}^\mathsf{T}\mathbf{A}\mathbf{R})(\mathbf{R}^\mathsf{T}\mathbf{A}\mathbf{R})) = \text{tr}(\mathbf{R}^\mathsf{T}\mathbf{A}\mathbf{A}\mathbf{R}) = \text{tr}(\mathbf{R}\mathbf{R}^\mathsf{T}\mathbf{A}^2) = \text{tr}(\mathbf{A}^2) = \bar{I}_2$, and because $\text{tr}((\mathbf{R}^\mathsf{T}\mathbf{A}\mathbf{R})^\mathsf{T}(\mathbf{R}^\mathsf{T}\mathbf{A}\mathbf{R})) = \text{tr}(\mathbf{R}^\mathsf{T}\mathbf{A}^\mathsf{T}\mathbf{R}\mathbf{R}^\mathsf{T}\mathbf{A}\mathbf{R}) = \text{tr}(\mathbf{R}^\mathsf{T}\mathbf{A}^\mathsf{T}\mathbf{A}\mathbf{R}) = \text{tr}(\mathbf{R}\mathbf{R}^\mathsf{T}\mathbf{A}^\mathsf{T}\mathbf{A}) = \text{tr}(\mathbf{A}^\mathsf{T}\mathbf{A}) = \bar{I}_3$. It follows that $\det\mathbf{A} = \frac{1}{2}(\bar{I}_1^2 - \bar{I}_2)$. The extra invariant follows because matrix $[\mathbf{A}]$ is upper triangular and therefore $[\mathbf{A}]^2$ is upper triangular whereas $[\mathbf{A}]^\mathsf{T}[\mathbf{A}]$ is symmetric.

Appendix C: Experimentation

Lanir and Fung [1974], Humphrey et al. [1987], Sacks [1999; 2000] and others have been perfecting the planar biaxial-stretch experiment for over four decades, as it applies to testing soft biological tissues. Our analysis of this experiment assumes homogeneous deformation and incorporates an upper triangular decomposition of the deformation gradient to quantify deformation and stress from experimental observations.

C.1. ***Deformation.*** An experimental assessment of deformation is straightforward. Extensions a and b and shear $\gamma = \tan\phi$ are the kinematic parameters to be acquired. Their values are directly observed and readily measured in accordance with Figure 2. Once they are known, the distortion matrix $[\tilde{\mathbf{F}}]$ can be populated according to (B.1). Coordinate directions $\mathbf{e}_1$ and $\mathbf{e}_2$ are orthogonal, as are coordinate directions $\mathbf{m}_1$ and $\mathbf{m}_2$. Angle θ rotates $\{\mathbf{e}_i\}$ into $\{\mathbf{m}_i\}$ and is drawn in its positive sense in Figure 2. With θ measured and known, one can populate the rotation matrix $[\mathbf{Q}]$ according to (B.3a).

Axes $\mathbf{m}_1$ and $\mathbf{m}_2$ can be thought of as being painted onto the material in some reference state t_0 oriented at an angle of θ_0 with respect to the spatial frame $\{\mathbf{e}_i\}$ so that initially

$$[\mathbf{F}_0] = \begin{bmatrix} \cos\theta_0 & \sin\theta_0 \\ -\sin\theta_0 & \cos\theta_0 \end{bmatrix}. \tag{C.1a}$$

In a deformed state t, material axis $\mathbf{m}_1$ remains a material axis, now rotated by an angle of θ from the spatial frame $\{\mathbf{e}_i\}$, however, the material line originally drawn in the $\mathbf{m}_2$ direction (drawn as $\mathbf{m}_{2,0}$ in Figure 2) may no longer be orthogonal to $\mathbf{m}_1$ at times $t > t_0$. Any angular difference (from being a right angle) is caused by shear and quantified by $\phi = \tan^{-1}\gamma$. The deformation gradient is now given by

$$[\mathbf{F}] = [\mathbf{Q}][\tilde{\mathbf{F}}] = \begin{bmatrix} \cos\theta & \sin\theta \\ -\sin\theta & \cos\theta \end{bmatrix} \begin{bmatrix} a & a\gamma \\ 0 & b \end{bmatrix} = \begin{bmatrix} a\cos\theta & b\sin\theta + a\gamma\cos\theta \\ -a\sin\theta & b\cos\theta - a\gamma\sin\theta \end{bmatrix}. \tag{C.1b}$$

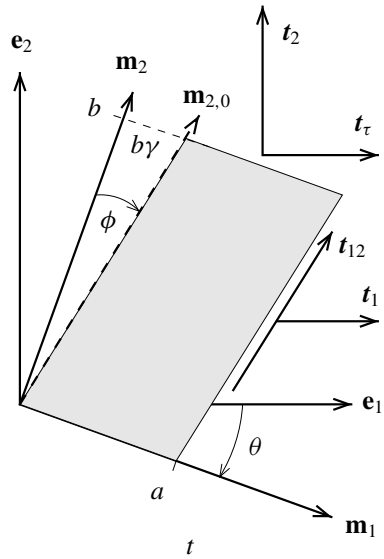

Figure 10. In-plane loading of a sample that was originally square and has undergone biaxial extension through orthogonal tractions $\boldsymbol{f}_1$ and $\boldsymbol{f}_2$ applied in the $\mathbf{e}_1$ and $\mathbf{e}_2$ directions, respectively, and have also undergone a shear through a traction $\boldsymbol{f}_\tau$ applied in the $\mathbf{e}_1$ direction, e.g., in the geometric sense of a double-lap shear. These three tractions have units of force per unit undeformed length of line, as measured in a reference state at time t_0 where $a = b = 1$ and $\gamma = 0$. In a deformed state, say at current time t, the actual tractions are $\boldsymbol{t}_1 = \boldsymbol{f}_1/b\sqrt{1+\gamma^2}$ and $\boldsymbol{t}_2 = \boldsymbol{f}_2/a$ and $\boldsymbol{t}_\tau = \boldsymbol{f}_\tau/a$ and have units of force per unit deformed length of line, where $\gamma = \tan\phi$. Traction $\boldsymbol{t}_{12}$ is an internal reaction caused by the grips. It cannot be controlled by the experimentalist. It exists to conserve angular momentum.

Direction $\mathbf{m}_1$ will often be selected to associate with a feature of interest in the sample being tested, e.g., aligned with a fiber direction.

This kinematic assessment is valid for any homogeneous planar deformation. It is general.

C.2. ***Stress.*** Stresses are more challenging to get, but the process is fairly straightforward. Cauchy's [1827] fundamental theorem for stress implies that $\boldsymbol{t} = \mathbf{T}\boldsymbol{n}$ where $\boldsymbol{t} = t_i\mathbf{e}_i$ is a traction vector, $\mathbf{T} = T_{ij}\mathbf{e}_i \otimes \mathbf{e}_j$ is Cauchy's stress tensor, and $\boldsymbol{n} = n_i\mathbf{e}_i$ is a unit normal to the surface upon which traction $\boldsymbol{t}$ acts. All fields are defined in the Eulerian frame $\{\mathbf{e}_1, \mathbf{e}_2\}$. The symmetric Kirchhoff [1852] stress, also an Eulerian field, is defined by $\mathbf{S} := \det(\mathbf{F})\mathbf{T} = S_{ij}\mathbf{e}_i \otimes \mathbf{e}_j$, where $\det\mathbf{F} = ab$ for membranes. Cauchy's theorem for stress rotates into the material frame $\{\mathbf{m}_i\}$ to become $\tilde{\boldsymbol{t}} = 1/(ab)\,\tilde{\mathbf{S}}\tilde{\boldsymbol{n}}$ wherein $\tilde{\boldsymbol{t}} = \mathbf{Q}^\mathsf{T}\boldsymbol{t}$ and $\tilde{\boldsymbol{n}} = \mathbf{Q}^\mathsf{T}\boldsymbol{n}$ and $\tilde{\mathbf{S}} = \mathbf{Q}^\mathsf{T}\mathbf{S}\mathbf{Q}$. It is formula $\tilde{\boldsymbol{t}} = 1/(ab)\,\tilde{\mathbf{S}}\tilde{\boldsymbol{n}}$ that we choose to apply to quantify stress in the material frame $\{\mathbf{m}_1, \mathbf{m}_2\}$.

When it comes to stress, each experiment is a separate boundary value problem. There is no general result like there is for deformation. Here we consider the experiment illustrated in Figure 10. Data extracted from such an experiment would be rich enough to ensure sensitivity for all parameters in our material model (22), hence our interest in this experiment.

To aid in avoiding wrinkling over a range of interest in shear strain, a sample would ideally be exposed to positive tractions in the 1 and 2 directions, denoted as $\boldsymbol{t}_1$ and $\boldsymbol{t}_2$ in Figure 10. After the membrane

is supporting surface tension, to offset the onset of wrinkling, one would impose a traction of shear $\boldsymbol{t}_\tau$ through, e.g., a double-lap shear gripping configuration (traction $\boldsymbol{t}_{12}$ present in Figure 10 is not under the control of an experimentalist. It is an internal traction caused by the grips).

In accordance with Figure 10, an application of Cauchy's theorem to the two edges of the areal element in that figure, solving for stress components in the $\{\mathbf{m}_i\}$ coordinate frame, leads to

$$\begin{Bmatrix} t_1\cos\theta + t_{12}\sin\phi \\ t_1\sin\theta + t_{12}\cos\phi \end{Bmatrix} = \frac{1}{ab}\begin{bmatrix} \tilde{S}_{11} & \tilde{S}_{12} \\ \tilde{S}_{21} & \tilde{S}_{22} \end{bmatrix}\begin{Bmatrix} \cos\phi \\ -\sin\phi \end{Bmatrix} \tag{C.2a}$$

and

$$\begin{Bmatrix} -t_2\sin\theta + t_\tau\cos\theta \\ t_2\cos\theta + t_\tau\sin\theta \end{Bmatrix} = \frac{1}{ab}\begin{bmatrix} \tilde{S}_{11} & \tilde{S}_{12} \\ \tilde{S}_{21} & \tilde{S}_{22} \end{bmatrix}\begin{Bmatrix} 0 \\ 1 \end{Bmatrix} \tag{C.2b}$$

that comprise a linear system of equations which, when solved for the components of stress $\tilde{S}_{ij}$, yields

$$\tilde{S}_{11} = a(\cos\theta f_1 + b\gamma t_{12}) + b\gamma(\cos\theta f_\tau - \sin\theta f_2), \tag{C.3a}$$

$$\tilde{S}_{12} = \tilde{S}_{21} = b(\cos\theta f_\tau - \sin\theta f_2), \tag{C.3b}$$

$$\tilde{S}_{22} = b(\sin\theta f_\tau + \cos\theta f_2), \tag{C.3c}$$

where, from symmetry of $\tilde{\mathbf{S}}$, i.e., $\tilde{S}_{21} = \tilde{S}_{12}$, one determines that

$$t_{12} = \frac{-a\sin\theta\cos\phi f_1 - b\sin(\theta+\phi) f_2 + b\cos(\theta+\phi) f_\tau}{ab\cos\phi}, \tag{C.3d}$$

wherein tractions f_1, f_2 and f_τ have units of force per unit undeformed length of line. They associate with tractions t_1, t_2 and t_τ, which have units of force per unit deformed length of line, via the formulæ

$$f_1 = b\sec\phi t_1, \quad f_2 = at_2, \quad f_\tau = at_\tau. \tag{C.4}$$

From (7a)–(7c), one finds that the conjugate stresses have values of

$$\pi = a(\cos\theta f_1 + b\gamma t_{12}) + b((\sin\theta + \gamma\cos\theta) f_\tau + (\cos\theta - \gamma\sin\theta) f_2), \tag{C.5a}$$

$$\sigma = a(\cos\theta f_1 + b\gamma t_{12}) - b((\sin\theta - \gamma\cos\theta) f_\tau + (\cos\theta + \gamma\sin\theta) f_2), \tag{C.5b}$$

$$\tau = a(\cos\theta f_\tau - \sin\theta f_2), \tag{C.5c}$$

and therefore an experimentalist needs to measure the three tractions f_1, f_2 and f_τ and the three deformations a, b and γ in order to quantify the three conjugate states of stress π, σ and τ.

These formulæ will simplify under a variety of special conditions, e.g., whenever $\theta = \phi = 0$ and $f_\tau = 0$, (C.5) simplifies to

$$\pi = af_1 + bf_2, \quad \sigma = af_1 - bf_2, \quad \tau = 0, \tag{C.6}$$

which describe the boundary condition used in the experiments of Lanir and Fung [1974], Humphrey et al. [1987], Sacks [1999; 2000], Billiar and Sacks [2000b; 2000a], Freed, Liao and Einstein [2014] and numerous others.

Appendix D: Derivation of Equation (4)

We begin with the well known description for stress power [Ogden 1984]:

$$\dot{W} = \operatorname{tr}(\mathbf{P}^{\mathsf{T}}\dot{\mathbf{F}}), \tag{D.1}$$

and then apply properties of the trace. This allows one to rewrite the above expression as

$$\dot{W} = \operatorname{tr}(\mathbf{P}^{\mathsf{T}}\dot{\mathbf{F}}) = \operatorname{tr}(\mathbf{F}\mathbf{P}^{\mathsf{T}}\dot{\mathbf{F}}\mathbf{F}^{-1}) = \operatorname{tr}(\mathbf{S}\mathbf{L}), \tag{D.2}$$

because stress $\mathbf{S}$ is symmetric and therefore $\mathbf{S} = \mathbf{P}\mathbf{F}^{\mathsf{T}} = \mathbf{F}\mathbf{P}^{\mathsf{T}}$. Incorporating the triangular decomposition of the deformation gradient established in Appendix B permits one to rewrite the above equation as

$$\dot{W} = \operatorname{tr}(\mathbf{S}\mathbf{L}) = \operatorname{tr}(\mathbf{S}\dot{\mathbf{F}}\mathbf{F}^{-1}) = \operatorname{tr}(\mathbf{S}\dot{\mathbf{Q}}\tilde{\mathbf{F}}\tilde{\mathbf{F}}^{-1}\mathbf{Q}^{-1}) + \operatorname{tr}(\mathbf{S}\mathbf{Q}\dot{\tilde{\mathbf{F}}}\tilde{\mathbf{F}}^{-1}\mathbf{Q}^{-1}). \tag{D.3}$$

The first trace on the right-hand side is zero because the Kirchhoff stress $\mathbf{S} = S_{ij}\mathbf{e}_i \otimes \mathbf{e}_j$ is symmetric while spin $\boldsymbol{\Xi} = \dot{\mathbf{Q}}\mathbf{Q}^{\mathsf{T}} = \Xi_{ij}\mathbf{e}_i \otimes \mathbf{e}_j$ is skew symmetric, therefore $\operatorname{tr}(\mathbf{S}\dot{\mathbf{Q}}\tilde{\mathbf{F}}\tilde{\mathbf{F}}^{-1}\mathbf{Q}^{-1}) = \operatorname{tr}(\mathbf{S}\dot{\mathbf{Q}}\mathbf{Q}^{\mathsf{T}}) = \operatorname{tr}(\mathbf{S}\boldsymbol{\Xi}) = 0$. Rearranging the second trace leads to

$$\dot{W} = \operatorname{tr}(\mathbf{Q}^{\mathsf{T}}\mathbf{S}\mathbf{Q}\dot{\tilde{\mathbf{F}}}\tilde{\mathbf{F}}^{-1}) = \operatorname{tr}(\tilde{\mathbf{S}}\tilde{\mathbf{L}}), \tag{D.4}$$

wherein $\tilde{\mathbf{S}} := \mathbf{Q}^{\mathsf{T}}\mathbf{S}\mathbf{Q} = \tilde{S}_{ij}\mathbf{m}_i \otimes \mathbf{m}_j$ and $\tilde{\mathbf{L}} := \dot{\tilde{\mathbf{F}}}\tilde{\mathbf{F}}^{-1} = \tilde{L}_{ij}\mathbf{m}_i \otimes \mathbf{m}_j$, as established in (E.4). Because $\tilde{\mathbf{S}}$ is symmetric and $\tilde{\mathbf{L}}$ is upper triangular,

$$\operatorname{tr}\left(\begin{bmatrix}\tilde{S}_{11} & \tilde{S}_{12}\\ \tilde{S}_{12} & \tilde{S}_{22}\end{bmatrix}\begin{bmatrix}\tilde{L}_{11} & \tilde{L}_{12}\\ 0 & \tilde{L}_{22}\end{bmatrix}\right) = \tilde{S}_{11}\tilde{L}_{11} + \tilde{S}_{12}\tilde{L}_{12} + \tilde{S}_{22}\tilde{L}_{22}, \tag{D.5}$$

which proves (4).

Appendix E: Decomposition of distortion $\tilde{\mathbf{F}}$

The distortion tensor $\tilde{\mathbf{F}}$ in (B.1) can be decomposed into a product of three fundamental modes of deformation, e.g., $\tilde{\mathbf{F}} = \tilde{\mathbf{F}}^{\circ}\tilde{\mathbf{F}}^{▯}\tilde{\mathbf{F}}^{\angle}$ with matrix components

$$[\tilde{\mathbf{F}}^{\circ}][\tilde{\mathbf{F}}^{▯}][\tilde{\mathbf{F}}^{\angle}] = \underbrace{\begin{bmatrix}\sqrt{ab} & 0\\ 0 & \sqrt{ab}\end{bmatrix}}_{\text{dilation}}\underbrace{\begin{bmatrix}\sqrt{a/b} & 0\\ 0 & \sqrt{b/a}\end{bmatrix}}_{\text{squeeze}}\underbrace{\begin{bmatrix}1 & \gamma\\ 0 & 1\end{bmatrix}}_{\text{shear}} = \begin{bmatrix}a & a\gamma\\ 0 & b\end{bmatrix} = [\tilde{\mathbf{F}}], \tag{E.1}$$

where dilation $\tilde{\mathbf{F}}^{\circ}$ is a uniform contribution to distortion, squeeze $\tilde{\mathbf{F}}^{▯}$ is an extrusion-like contribution to distortion[2], and shear $\tilde{\mathbf{F}}^{\angle}$ is an angular contribution to distortion. The distortions of dilation and squeeze commute, because they are diagonal, and as such $\tilde{\mathbf{F}}^{\circ}\tilde{\mathbf{F}}^{▯} = \tilde{\mathbf{F}}^{▯}\tilde{\mathbf{F}}^{\circ}$. The distortions of squeeze and shear are isometric, because they preserve area, and as such $\det\tilde{\mathbf{F}}^{▯} = \det\tilde{\mathbf{F}}^{\angle} = 1$.

[2] Freed and Srinivasa [2015] refer to $\tilde{\mathbf{F}}^{▯}$ as extrusion. Here we call it squeeze to give it a more intuitive terminology to a wider audience. It describes an isometric deformation that maps a square □ into a rectangle ▯ of the same area. It is similar to (but distinct from) pure shear [Freed and Srinivasa 2015].

E.1. ***Rates of distortion.*** Differentiating the decomposition of distortion (E.1) by the product rule gives

$$\begin{aligned}\dot{\tilde{\mathbf{F}}} &= \dot{\tilde{\mathbf{F}}}^{\circ}\tilde{\mathbf{F}}^{\square}\tilde{\mathbf{F}}^{\angle} + \tilde{\mathbf{F}}^{\circ}\dot{\tilde{\mathbf{F}}}^{\square}\tilde{\mathbf{F}}^{\angle} + \tilde{\mathbf{F}}^{\circ}\tilde{\mathbf{F}}^{\square}\dot{\tilde{\mathbf{F}}}^{\angle}\\ &= \dot{\tilde{\mathbf{F}}}^{\circ}\tilde{\mathbf{F}}^{\square}\tilde{\mathbf{F}}^{\angle} + \dot{\tilde{\mathbf{F}}}^{\square}\tilde{\mathbf{F}}^{\circ}\tilde{\mathbf{F}}^{\angle} + \tilde{\mathbf{F}}^{\circ}\tilde{\mathbf{F}}^{\square}\dot{\tilde{\mathbf{F}}}^{\angle}\\ &= \dot{\tilde{\mathbf{F}}}^{\circ}(\tilde{\mathbf{F}}^{\circ})^{-1}\tilde{\mathbf{F}} + \dot{\tilde{\mathbf{F}}}^{\square}(\tilde{\mathbf{F}}^{\square})^{-1}\tilde{\mathbf{F}} + \tilde{\mathbf{F}}(\tilde{\mathbf{F}}^{\angle})^{-1}\dot{\tilde{\mathbf{F}}}^{\angle}\\ &= \tilde{\mathbf{L}}^{\circ}\tilde{\mathbf{F}} + \tilde{\mathbf{L}}^{\square}\tilde{\mathbf{F}} + \tilde{\mathbf{F}}\tilde{\mathbf{L}}^{\angle},\end{aligned} \tag{E.2}$$

where, to advance from the first line to the second, we use the fact that $\tilde{\mathbf{F}}^{\circ}$ and $\tilde{\mathbf{F}}^{\square}$ commute. Identities, e.g., $\mathbf{I} = (\tilde{\mathbf{F}}^{\circ})^{-1}\tilde{\mathbf{F}}^{\circ}$, along with (E.1) advance the second line to the third. Going from the third line to the fourth is done by defining velocity gradients for the three modes comprising the rate of distortion:

(1) For dilation, define $\tilde{\mathbf{L}}^{\circ} := \dot{\tilde{\mathbf{F}}}^{\circ}\big(\tilde{\mathbf{F}}^{\circ}\big)^{-1} = \big(\tilde{\mathbf{F}}^{\circ}\big)^{-1}\dot{\tilde{\mathbf{F}}}^{\circ}$ whose matrix components are

$$[\tilde{\mathbf{L}}^{\circ}] = \frac{1}{2}\left(\frac{\dot{a}}{a} + \frac{\dot{b}}{b}\right)\begin{bmatrix}1 & 0\\ 0 & 1\end{bmatrix}. \tag{E.3a}$$

(2) For squeeze, define $\tilde{\mathbf{L}}^{\square} := \dot{\tilde{\mathbf{F}}}^{\square}\big(\tilde{\mathbf{F}}^{\square}\big)^{-1} = \big(\tilde{\mathbf{F}}^{\square}\big)^{-1}\dot{\tilde{\mathbf{F}}}^{\square}$ whose matrix components are

$$[\tilde{\mathbf{L}}^{\square}] = \frac{1}{2}\left(\frac{\dot{a}}{a} - \frac{\dot{b}}{b}\right)\begin{bmatrix}1 & 0\\ 0 & -1\end{bmatrix}. \tag{E.3b}$$

(3) For shear, define $\tilde{\mathbf{L}}^{\angle} := \dot{\tilde{\mathbf{F}}}^{\angle}\big(\tilde{\mathbf{F}}^{\angle}\big)^{-1} = \big(\tilde{\mathbf{F}}^{\angle}\big)^{-1}\dot{\tilde{\mathbf{F}}}^{\angle}$ whose matrix components are

$$[\tilde{\mathbf{L}}^{\angle}] = \begin{bmatrix}0 & \dot{\gamma}\\ 0 & 0\end{bmatrix}. \tag{E.3c}$$

It turns out that the material velocity gradients $\tilde{\mathbf{L}}^{\circ}$, $\tilde{\mathbf{L}}^{\square}$ and $\tilde{\mathbf{L}}^{\angle}$ commute in the products that define them.

The three material velocity gradients that are defined in (E.3) sum according to (E.2) to form a log-like rate of distortion that is defined by $\tilde{\mathbf{L}} := \dot{\tilde{\mathbf{F}}}\tilde{\mathbf{F}}^{-1} = \tilde{\mathbf{L}}^{\circ} + \tilde{\mathbf{L}}^{\square} + \tilde{\mathbf{F}}\tilde{\mathbf{L}}^{\angle}\tilde{\mathbf{F}}^{-1}$ with matrix components[3]

$$[\tilde{\mathbf{L}}] = \begin{bmatrix}\dot{a}/a & a\dot{\gamma}/b\\ 0 & \dot{b}/b\end{bmatrix}. \tag{E.4}$$

The Eulerian velocity gradient $\mathbf{L} := \dot{\mathbf{F}}\mathbf{F}^{-1}$ and the material velocity gradient $\tilde{\mathbf{L}} := \dot{\tilde{\mathbf{F}}}\tilde{\mathbf{F}}^{-1}$ relate to one another through the expression

$$\begin{aligned}\tilde{\mathbf{L}} &= \mathbf{Q}^{\mathsf{T}}(\mathbf{L} - \boldsymbol{\Xi})\mathbf{Q},\\ &= \mathbf{Q}^{\mathsf{T}}\mathbf{L}\mathbf{Q} - \boldsymbol{\Xi},\end{aligned} \quad \text{wherein} \quad [\boldsymbol{\Xi}] = \begin{bmatrix}0 & \dot{\theta}\\ -\dot{\theta} & 0\end{bmatrix} \tag{E.5}$$

with spin $\boldsymbol{\Xi} := \dot{\mathbf{Q}}\mathbf{Q}^{\mathsf{T}}$, an Eulerian field, designating the rate at which the material frame $\{\mathbf{m}_i\}$ rotates about the Eulerian frame $\{\mathbf{e}_i\}$ with θ being defined in (B.3b) and drawn in Figure 1. The skew symmetric part of (E.5) produces the useful result

$$\boldsymbol{\Xi} = \mathbf{W} - \tilde{\mathbf{W}}, \tag{30}$$

[3] Freed and Srinivasa [2015] define $\tilde{\mathbf{L}}$ as $\tilde{\mathbf{F}}^{-1}\dot{\tilde{\mathbf{F}}}$, whereas we define it as $\dot{\tilde{\mathbf{F}}}\tilde{\mathbf{F}}^{-1}$. They derived the logarithm of distortion $\ln\tilde{\mathbf{F}}$ whose rate is not $\tilde{\mathbf{L}}$. The diagonal components of $\tilde{\mathbf{L}}$ and $\ln\tilde{\mathbf{F}}$ are the same; it is in the off-diagonal components that they differ.

stated in (8d), where $\mathbf{W} := \frac{1}{2}(\mathbf{L} - \mathbf{L}^{\mathsf{T}})$ and $\tilde{\mathbf{W}} := \frac{1}{2}(\tilde{\mathbf{L}} - \tilde{\mathbf{L}}^{\mathsf{T}})$ are the spatial and material vorticities.

Remark. An important but subtle point is that $\tilde{\mathbf{L}}$ is not integrable, because $\tilde{\mathbf{F}}\tilde{\mathbf{L}}^{\angle}\tilde{\mathbf{F}}^{-1}$ is not integrable, and therefore $\tilde{\mathbf{L}}$ is not a viable measure for strain rate. Strain is a field that depends only upon its two end states, and not upon the path traversed to get from one state to the other. Consequently, *strain rate must be described by an exact differential*, and $\tilde{\mathbf{L}}$ is not an exact differential.

Acknowledgements

Discussions with professor Daniel R. Einstein from Saint Martin's University and with professors J. C. Criscione, K. R. Rajagopal and Arun R. Srinivasa from Texas A&M University are gratefully acknowledged.

References

[Amensag and McFetridge 2014] S. Amensag and P. S. McFetridge, "Tuning scaffold mechanics by laminating native extracellular matrix membranes and effects on early cellular remodeling", *J. Biomed. Mater. Res. A* **102**:5 (2014), 1325–1333.

[Becker 1893] G. F. Becker, "The finite elastic stress-strain function", *Am. J. Sci.* **46**:275 (1893), 337–356.

[Billiar and Sacks 2000a] K. L. Billiar and M. S. Sacks, "Biaxial mechanical properties of the natural and glutaraldehyde treated aortic valve cusp, part I: Experimental results", *J. Biomech. Eng.* **122**:1 (2000), 23–30.

[Billiar and Sacks 2000b] K. L. Billiar and M. S. Sacks, "Biaxial mechanical properties of the native and glutaraldehyde-treated aortic valve cusp, part II: A structural constitutive model", *J. Biomech. Eng.* **122**:4 (2000), 327–335.

[Bird et al. 1987a] R. B. Bird, R. C. Armstrong, and O. Hassager, *Dynamics of polymeric liquids, I: Fluid mechanics*, 2nd ed., Wiley, New York, 1987.

[Bird et al. 1987b] R. B. Bird, C. F. Curtiss, R. C. Armstrong, and O. Hassager, *Dynamics of polymeric liquids, II: Kinetic theory*, 2nd ed., Wiley, New York, 1987.

[Carathéodory 1909] C. Carathéodory, "Untersuchungen über die Grundlagen der Thermodynamik", *Math. Ann.* **67**:3 (1909), 355–386. Translated in *The second law of thermodynamics* J. Kestin (ed.), Dowden, Hutchinson and Ross, Stroudsberg, PA, (1976) 229–256.

[Cauchy 1827] A.-L. Cauchy, *Exercices de mathématiques*, de Bure Frères, Paris, 1827.

[Criscione 2003] J. C. Criscione, "Rivlin's representation formula is ill-conceived for the determination of response functions via biaxial testing", *J. Elasticity* **70**:1-3 (2003), 129–147.

[Criscione et al. 2000] J. C. Criscione, J. D. Humphrey, A. S. Douglas, and W. C. Hunter, "An invariant basis for natural strain which yields orthogonal stress response terms in isotropic hyperelasticity", *J. Mech. Phys. Solids* **48**:12 (2000), 2445–2465.

[Criscione et al. 2003a] J. C. Criscione, M. S. Sacks, and W. C. Hunter, "Experimentally tractable, pseudo-elastic constitutive law for biomembranes, I: Theory", *J. Biomech. Eng.* **125**:1 (2003), 94–99.

[Criscione et al. 2003b] J. C. Criscione, M. S. Sacks, and W. C. Hunter, "Experimentally tractable, pseudo-elastic constitutive law for biomembranes, II: Application", *J. Biomech. Eng.* **125**:1 (2003), 100–105.

[Dienes 1979] J. K. Dienes, "On the analysis of rotation and stress rate in deforming bodies", *Acta Mech.* **32**:4 (1979), 217–232.

[Dokos et al. 2002] S. Dokos, B. H. Smaill, A. A. Young, and I. J. LeGrice, "Shear properties of passive ventricular myocardium", *Am. J. Physiol. Heart Circ. Physiol.* **283**:6 (2002), H2650–H2659.

[Evans and Skalak 1979] E. Evans and R. Skalak, "Mechanics and thermodynamics of biomembranes: part 2", *CRC Crit. Rev. Bioeng.* **3**:4 (1979), 331–418.

[Freed 2014] A. D. Freed, *Soft solids: a primer to the theoretical mechanics of materials*, Birkhäuser, Basel, 2014.

[Freed and Rajagopal 2016] A. D. Freed and K. R. Rajagopal, "A promising approach for modeling biological fibers", *Acta Mech.* **227**:6 (2016), 1609–1619.

[Freed and Srinivasa 2015] A. D. Freed and A. R. Srinivasa, "Logarithmic strain and its material derivative for a QR decomposition of the deformation gradient", *Acta Mech.* **226**:8 (2015), 2645–2670.

[Freed, Liao and Einstein 2014] A. D. Freed, J. Liao, and D. R. Einstein, "A membrane model form implicit elasticity theory: application to visceral pleura", *Biomech. Model. Mechanobiol.* **13**:4 (2014), 871–881.

[Fung 1993] Y. C. Fung, *Biomechanics: mechanical properties of living tissues*, 2nd ed., Springer, New York, 1993.

[Grashow et al. 2006] J. S. Grashow, A. P. Yoganathan, and M. S. Sacks, "Biaixal stress–stretch behavior of the mitral valve anterior leaflet at physiologic strain rates", *Ann. Biomed. Eng.* **34**:2 (2006), 315–325.

[Green 1848] G. Green, "On the propagation of light in crystallized media", *Trans. Cambridge Philos. Soc.* **7** (1848), 121–140.

[Green and Naghdi 1965] A. E. Green and P. M. Naghdi, "A general theory of an elastic-plastic continuum", *Arch. Rational Mech. Anal.* **18**:4 (1965), 251–281.

[Helfrich 1973] W. Helfrich, "Elastic properties of lipid bilayers: theory and possible experiments", *Z. Naturforsch C.* **28**:11 (1973), 693–703.

[Hill 1978] R. Hill, *Aspects of invariance in solid mechanics*, Advances in applied mechanics **18**, Academic Press, New York, 1978.

[Humphrey 1998] J. Humphrey, "Computer methods in membrane biomechanics", *Comput. Methods Biomech. Biomed. Eng.* **1**:3 (1998), 171–210.

[Humphrey et al. 1987] J. Humphrey, D. Vawter, and R. Vito, "Quantification of strains in biaxially tested soft tissues", *J. Biomech.* **20**:1 (1987), 59–65.

[Kestin and Rice 1970] J. Kestin and J. R. Rice, "Paradoxes in the application of thermodynamics to strained solids", pp. 275–298 in *A critical review of thermodynamics*, edited by E. Stuart et al., Mono Book Corp., Baltimore, MD, 1970.

[Kharaziha et al. 2013] M. Kharaziha, M. Nikkhah, S.-R. Shin, N. Annabi, N. Mosoumi, A. Gaharwar, G. Camci-Unal, and A. Khademhosseini, "PGS: gelatin nanofibrous scaffolds with tunable mechanical and structural properties for engineering cardiac tissues", *Biomaterials* **34**:27 (2013), 6355–6366.

[Kirchhoff 1852] G. Kirchhoff, "Über die Gleichungen des Gleichgewichtes eines elastischen Körpers bei nicht unendlich kleinen Verschiebungen seiner Theile", *Sitzungsberichte der Akademie der Wissenschaften, Wien* **9** (1852), 763–773.

[Lanir and Fung 1974] Y. Lanir and Y. Fung, "Two-dimensional mechanical properties of rabbit skin, I: Experimental system", *J. Biomech.* **7**:1 (1974), 29–34.

[Lodge 1964] A. Lodge, *Elastic liquids: an introductory vector treatment of finite-strain polymer rheology*, Academic Press, London, 1964.

[Lodge 1974] A. Lodge, *Body tensor fields in continuum mechanics: with applications to polymer rheology*, Academic Press, New York, 1974.

[Lubarda 2010] V. A. Lubarda, "Constitutive analysis of thin biological membranes with application to radial stretching of a hollow circular membrane", *J. Mech. Phys. Solids* **58**:6 (2010), 860–873.

[Murnaghan 1954] F. D. Murnaghan, "On the unitary invariants of a square matrix", *Anais Acad. Brasil. Ci.* **26** (1954), 1–7.

[Noll 1955] W. Noll, "On the continuity of the solid and fluid states", *J. Rational Mech. Anal.* **4** (1955), 3–81.

[Ogden 1984] R. Ogden, *Non-linear elastic deformations*, Wiley, New York, 1984.

[Oldroyd 1950] J. G. Oldroyd, "On the formulation of rheological equations of state", *Proc. Roy. Soc. London. A.* **200** (1950), 523–541.

[Pipkin 1986] A. C. Pipkin, "The relaxed energy density for isotropic elastic membranes", *IMA J. Appl. Math.* **36**:1 (1986), 85–99.

[Poynting 1909] J. H. Poynting, "On pressure perpendicular to the shear planes in finite pure shears, and on the lengthening of loaded wires when twisted", *Proc. Roy. Soc. London. A.* **82**:557 (1909), 546–559.

[Rajagopal 2003] K. R. Rajagopal, "On implicit constitutive theories", *Appl. Math.* **48**:4 (2003), 279–319.

[Rajagopal 2011] K. R. Rajagopal, "Conspectus of concepts of elasticity", *Math. Mech. Solids* **16**:5 (2011), 536–562.

[Rivlin and Smith 1969] R. Rivlin and G. Smith, "Orthogonal integrity basis for N symmetric matrices", pp. 121–141 in *Contributions to mechanics*, edited by D. Abir, Pergamon Press, New York, 1969.

[Rosakis 1990] P. Rosakis, "Ellipticity and deformations with discontinuous gradients in finite elastostatics", *Arch. Rational Mech. Anal.* **109**:1 (1990), 1–37.

[Sacks 1999] M. Sacks, "A method for planar biaxial mechanical testing that includes in-plane shear", *J. Biomech. Eng.* **121**:5 (1999), 551–555.

[Sacks 2000] M. S. Sacks, "Biaxial mechanical evaluation of planar biological materials", *J. Elasticity* **61**:1-3 (2000), 199–246.

[Sacks and Chuong 1993] M. Sacks and C. Chuong, "Biaxial mechanical properties of passive right ventricular free wall myocardium", *J. Biomech. Eng.* **115**:2 (1993), 202–205.

[Simo and Hughes 1998] J. C. Simo and T. J. R. Hughes, *Computational inelasticity*, Interdisciplinary Applied Mathematics **7**, Springer, New York, 1998.

[Spencer 1972] A. Spencer, *Deformations in fibre-reinforced materials*, Clarendon Press, Oxford, England, 1972.

[Srinivasa 2012] A. R. Srinivasa, "On the use of the upper triangular (or QR) decomposition for developing constitutive equations for Green-elastic materials", *Int. J. Eng. Sci.* **60** (2012), 1–12.

[Steigmann 1990] D. J. Steigmann, "Tension-field theory", *Proc. Roy. Soc. London A* **429**:1876 (1990), 141–173.

[Stewart 1973] G. W. Stewart, *Introduction to matrix computations*, Academic Press, New York, 1973.

[Thomson 1878] W. Thomson, "On the thermoelastic, thermomagnetic, and pyroelectric properties of matter", *Philos. Mag.* **5**:28 (1878), 4–27.

[Ting 1985] T. C. T. Ting, "Determination of $\mathbf{C}^{1/2}$, $\mathbf{C}^{-1/2}$ and more general tensor functions of $\mathbf{C}$", *J. Elasticity* **15**:3 (1985), 319–323.

[Truesdell and Noll 2004] C. Truesdell and W. Noll, *The non-linear field theories of mechanics*, 3rd ed., Springer, Berlin, 2004.

[Xie et al. 2015] M. Xie, J. Ge, Y. Xue, Y. Du, B. Lei, and P. X. Ma, "Photo-crosslinked fabrication of novel biocompatible and elastomeric star-shaped inositol-based polymer with highly tunable mechanical behavior and degradation", *J. Mech. Behav. Biomed. Mater.* **51** (2015), 163–168.

Received 22 Jul 2016. Revised 2 Oct 2016. Accepted 18 Oct 2016.

ALAN D. FREED: afreed@tamu.edu
Department of Mechanical Engineering, Texas A&M University, TAMU 3123, College Station, TX 77843, United States

VEYSEL EREL: veyselerel@hotmail.com
Department of Mechanical Engineering, Texas A&M University, TAMU 3123, College Station, TX 77843, United States

MICHAEL R. MORENO: michael.moreno@tamu.edu
Department of Mechanical Engineering, Texas A&M University, TAMU 3123, College Station, TX 77843, United States

SUBMISSION GUIDELINES

ORIGINALITY

Authors may submit manuscripts in PDF format online at the Submissions page. Submission of a manuscript acknowledges that the manuscript is original and has neither previously, nor simultaneously, in whole or in part, been submitted elsewhere. Information regarding the preparation of manuscripts is provided below. Correspondence by email is requested for convenience and speed. For further information, write to contact@msp.org.

LANGUAGE

Manuscripts must be in English. A brief abstract of about 150 words or less must be included. The abstract should be self-contained and not make any reference to the bibliography. Also required are keywords and subject classification for the article, and, for each author, postal address, affiliation (if appropriate), and email address if available. A home-page URL is optional.

FORMAT

Authors can use their preferred manuscript-preparation software, including for example Microsoft Word or any variant of TEX. The journal itself is produced in LATEX, so accepted articles prepared using other software will be converted to LATEX at production time. Authors wishing to prepare their document in LATEX can follow the example file at www.jomms.net (but the use of other class files is acceptable). At submission time only a PDF file is required. After acceptance, authors must submit all source material (see especially Figures below).

REFERENCES

Bibliographical references should be complete, including article titles and page ranges. All references in the bibliography should be cited in the text. The use of BibTEX is preferred but not required. Tags will be converted to the house format (see a current issue for examples); however, for submission you may use the format of your choice. Links will be provided to all literature with known web locations; authors can supply their own links in addition to those provided by the editorial process.

FIGURES

Figures must be of publication quality. After acceptance, you will need to submit the original source files in vector format for all diagrams and graphs in your manuscript: vector EPS or vector PDF files are the most useful. (EPS stands for Encapsulated PostScript.)

Most drawing and graphing packages—Mathematica, Adobe Illustrator, Corel Draw, MATLAB, etc.—allow the user to save files in one of these formats. Make sure that what you're saving is vector graphics and not a bitmap. If you need help, please write to graphics@msp.org with as many details as you can about how your graphics were generated.

Please also include the original data for any plots. This is particularly important if you are unable to save Excel-generated plots in vector format. Saving them as bitmaps is not useful; please send the Excel (.xls) spreadsheets instead. Bundle your figure files into a single archive (using zip, tar, rar or other format of your choice) and upload on the link you been given at acceptance time.

Each figure should be captioned and numbered so that it can float. Small figures occupying no more than three lines of vertical space can be kept in the text ("the curve looks like this:"). It is acceptable to submit a manuscript with all figures at the end, if their placement is specified in the text by means of comments such as "Place Figure 1 here". The same considerations apply to tables.

WHITE SPACE

Forced line breaks or page breaks should not be inserted in the document. There is no point in your trying to optimize line and page breaks in the original manuscript. The manuscript will be reformatted to use the journal's preferred fonts and layout.

PROOFS

Page proofs will be made available to authors (or to the designated corresponding author) at a Web site in PDF format. Failure to acknowledge the receipt of proofs or to return corrections within the requested deadline may cause publication to be postponed.

Journal of Mechanics of Materials and Structures

Volume 12, No. 2 March 2017